AD-A099 149 CARNEGIE-MELLON UNIV PITTSBURGH PA DEPT OF MECHANICA--ETC F/G 11/6
AN IMPROVED MODEL FOR SECOND PHASE PARTICLE INTERACTION ANALYSI--ETC(U)
NOV 80 R R BATARA6S AFOSR-78-3533
UNCLASSIFIED SM80-14 AFOSR-TR-81-0467 NL

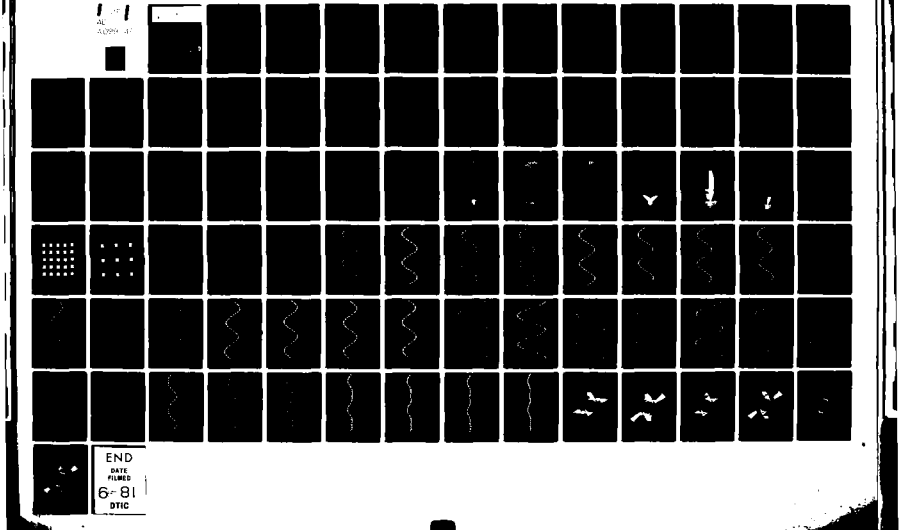

END
DATE FILMED
6-81
DTIC

Carnegie-Mellon University
PITTSBURGH, PENNSYLVANIA 15213

DEPARTMENT OF
MECHANICAL ENGINEERING

AN IMPROVED MODEL FOR SECOND PHASE PARTICLE INTERACTION ANALYSIS

Roberts R. Bataragş

Report SM80-14

November 1980

Submitted in partial fulfillment of the
requirements for the degree of
Master of Engineering

Department of Mechanical Engineering
Carnegie Institute of Technology
Carnegie-Mellon University
Pittsburgh, Pennsylvania

UNCLASSIFIED

SECURITY CLASSIFICATION OF THIS PAGE (When Data Entered)

REPORT DOCUMENTATION PAGE	READ INSTRUCTIONS BEFORE COMPLETING FORM
1. REPORT NUMBER: AFOSR-TR-81-0467	2. GOVT ACCESSION NO.: AD-A099 149
4. TITLE (and Subtitle): AN IMPROVED MODEL FOR SECOND PHASE PARTICLE INTERACTION ANALYSIS	5. TYPE OF REPORT & PERIOD COVERED: INTERIM, SEP 80-DEC 80
	6. PERFORMING ORG. REPORT NUMBER
7. AUTHOR(s): ROBERTS R. BATARAGS	8. CONTRACT OR GRANT NUMBER(s): AFOSR-78-3533
9. PERFORMING ORGANIZATION NAME AND ADDRESS: Carnegie Institute of Technology, Carnegie Mellon University, Pittsburgh, PA 15213	10. PROGRAM ELEMENT, PROJECT, TASK AREA & WORK UNIT NUMBERS: 61102F, 2307/B2
11. CONTROLLING OFFICE NAME AND ADDRESS: Air Force Office of Scientific Research/NA, Bolling AFB, DC 20332	12. REPORT DATE: November 1980; 13. NUMBER OF PAGES: 78
14. MONITORING AGENCY NAME & ADDRESS (if different from Controlling Office): SM80-14	15. SECURITY CLASS. (of this report): UNCLASSIFIED; 15a. DECLASSIFICATION/DOWNGRADING SCHEDULE

16. DISTRIBUTION STATEMENT (of this Report)

Approved for public release; distribution unlimited.

17. DISTRIBUTION STATEMENT (of the abstract entered in Block 20, if different from Report)

18. SUPPLEMENTARY NOTES

19. KEY WORDS (Continue on reverse side if necessary and identify by block number)

CONSTITUTIVE MODEL
INELASTICITY
MICROSTRUCTURE
FINITE ELEMENT MODEL

20. ABSTRACT (Continue on reverse side if necessary and identify by block number)

In high-strength alloys, microstructure can influence toughness in a manner not yet fully quantified. Computational mechanics offers a tool whereby the events leading to fracture may be simulated, but the success of such an enterprise depends heavily upon the quality of the model employed. This report outlines a sequence of events thought to precede ductile fracture and presents a finite element model designed to capture the main events. The model is considered to be an improvement over an earlier one, and data are presented to support this conclusion.

DD FORM 1 JAN 73 1473

UNCLASSIFIED

SECURITY CLASSIFICATION OF THIS PAGE (When Data Entered)

AN IMPROVED MODEL FOR SECOND PHASE PARTICLE INTERACTION ANALYSIS

Roberts R. Batarags

Report SM80-14 November 1980

Submitted in partial fulfillment of the
requirements for the degree of
Master of Engineering

Department of Mechanical Engineering
Carnegie Institute of Technology
Carnegie-Mellon University
Pittsburgh, Pennsylvania

ACKNOWLEDGEMENTS

This work was supported by the Air Force Office of Scientific Research, Research Grant AFOSR-78-3533.

Additionally, I would like to thank my officemates for their support and input. A particular note of thanks to Joseph Solecki for his tolerance and willingness to discuss anything and everything, at any time - for any length of time.

Thanks as well to Lisa Papalia for her preparation of this manuscript.

Finally and most importantly, I thank my advisor, Professor J. L. Swedlow. His guidance and steadfastness has been most helpful and appreciated.

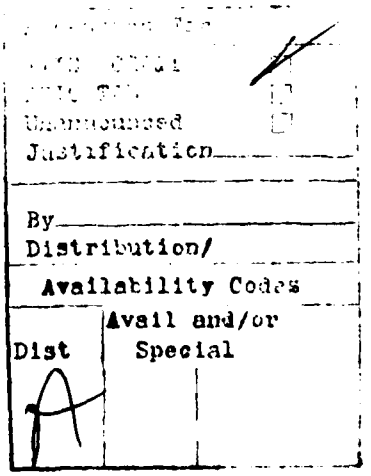

I. INTRODUCTION

The role of microstructure and how its behavior under loading influences the ductile fracture process are of significant interest to metallurgists as well as the mechanics community. We have addressed the issue, centering our efforts on computer simulation of microstructural events preceding fracture - primarily dealing with the effect of second phase particles. To date our efforts have met with limited success. However, we believe that the modeling of the microstructure under consideration which comprises the bulk of this report, has been improved and should allow for further work to proceed at a more rapid rate.

In order to provide a framework for our efforts, as well as to impart some sense to the sections to follow, a recapitulation of how we envisage the ductile fracture process to proceed is presented first.

1. A dispersion of second phase particles, whose material properties differ from the bulk of the material (here termed the matrix and which is considered both homogeneous and isotropic) will, under the action of low level loading, cause a local stress concentration to appear.

2. As the level of load increases and small scale (i.e. contained) plastic yielding occurs, the elastic stress concentration tends to be suppressed, whereas the local strains (measured in terms of e.g. the octatedral strain) will tend to increase.

2a. The foregoing sequence can be observed in the vicinity of a single second phase particle, since the events are local to the particle-matrix interface - not long range.

3. Depending on variables such as relative material properties, particle-particle spacing, load direction vis-a-vis the particle-particle axis and lateral constraint, a level of excitation will be attained at which the size of the plastic zones are no longer confined to and determined by an individual particle, but will rather connect with the plastic zones surrounding a neighbor particle. In other words, a change of size scale can occur such that the extent and shape of the plastic zone is no longer governed by a characteristic dimension of a single particle, but is instead governed by a dimension relating to the proximity of neighboring particles.

4. Once plastic zones from neighboring particles have interacted, further excitation will tend to concentrate within such highly strained regions. The interaction of second phase particles creates a pathway for macroscopic ductile fracture. Further material damage, such as the metallurgically observed void growth and coalescense phenomena, will occur in the most severely strained regions, leading to development of small fissures initially, and gross section fracture ultimately.

Our efforts have been concentrated on the effects of interacting second phase particles, and on the development and extent of strain localization We have attempted to demonstrate that the mere proximity of neighboring particles can lead to interaction between the attendant plastic zones, at quite low far field levels of excitation. Furthermore and most importantly, we have attempted to show that the presence of multiple second phase particles will accelerate the growth of regions of high strain.

Unfortunately, we have of late become sidetracked from the main issue due to modelling problems, which are discussed in the next section. Consequently,

the brunt of our latest endevour has been to eradicate the problems with our model of the microstructure. We believe that an adequate representation for the microstructure has been developed, so that progress can be made on the initial objective.

II. DISCUSSION AND EVALUATION OF PREVIOUS WORK

The work discussed in this section has been documented earlier [1,2]. The objective here is not to detail or reiterate the findings discussed previously, rather to highlight some of these findings for continuity. Additionally to be discussed are the problems with those findings and substantiating evidence.

The initial work [1] addressed the question of second phase particle interaction, under the assumption that the particle-matrix interface remained "coherent." An attempt to estimate the effect of particle destruction was made, by allowing one particle to open up at its center (the "burst" model), although such a procedure was acknowledged to be not entirely realistic. The latter work, [2], concerns itself with the issue of a matrix-particle decohesion, and the effect of such an event on the interaction of particles.

The particular two phase system chosen for these analyses is a Titanium alloy (Ti-6AL-4V), consisting of cylindrical second phase particles (α) in an otherwise homogeneous matrix (β) phase. Elastically the α phase is stiffer than the β, however, the α possesses a lower yield stress. Furthermore, the phase exhibits an extremely flat stress-strain curve plastically. That is, α work hardens to a much lesser extent than the β phase. The stress-strain curves for both the α and β phase are presented in Figs. 1 and 2, respectively.

The fact that the second phase particles are regarded as cylindrical allows one conceptually to section the material in such a fashion as to achieve a two dimensional problem containing circular second phase particles. Since interaction is the issue, a minimum of two particles is necessary. In these studies, the center to center distance was held fixed at 11 1/2 diameters. Because this alloy system, heat-treated differently, can produce a wide variation in particle spacing, 11 1/2 diameters is very conservative.

Both analyses utilized the identical finite element model for the microstructure, which is presented in Figures 3-5. Figure 3 depicts the complete model allowing for two second phase particles and three of the five distinct orientations of the particle-particle axis with respect to the loading axis, assumed vertical. Figure 4 indicates the regions encompassing both second phase particles, and their connectivity. An enlargement of one particle, and its immediate surroundings is seen in Figure 5.

Excitation of the model (Figure 3) is effected by displacement boundary conditions - tensile in the vertical direction. Loading in the lateral direction is not as easily resolved. At least three distinct lateral loading conditions (constraints) can be envisaged:

1) no motion normal to the direction of tensile loading permitted (Full Constraint)

2) no lateral constraint whatsoever (Nil Constraint)

3) lateral motion associated with Poisson contraction (Poisson Constraint)

A fuller discussion can be found in SM77-7, pages 7-9 (ref. 1).
See also the generalized discussion by Swedlow and Smelser (ref. 3).

DISCUSSION OF SM77-7

This analysis attempted to establish the phenomena of second phase particle interaction computationally, at far field strain levels smaller than those typically viewed by metallurgists studying the identical problem. The intent was to demonstrate that the presence of neighboring particles would alter the strain fields, even at such low levels of straining. If this were the case then the existence of second phase particles provides a precursor to large scale material damage. In effect - from the relative material properties of matrix and particles and their separation - the load under which the material will fail ductidely could be inferred.

Representative results are given by Figures 6-9. The first two figures (numbers 6 and 7) show octahedral strain values around one particle. The data are normalized with respect to octahedral strain at the proportional limit, a value of 0.012257. The radial location is in the matrix material, very close to the particle-matrix interface. The four curves indicate varying far-field levels of strain, with the lowest curve being an elastic result. Figures 8 and 9 depict the regions in which the local octahedral strains exceed far field values by 5%, (i.e. 1.05 times far field strain).

At the time the results were obtained, they were viewed as disappointing, although not inaccurate. The elastic curves on Figures 6 and 7 indicate no interaction, as should be expected at such a large particle spacing. Furthermore, the curves are smooth and reminiscent of elastic results for say a hole in a plate. From Figures 8 and 9, which represent the least and the most interaction seen, respectively, again benign conclusions were drawn. Consequently, work proceeded with an attempt to deal with matrix-particle decohesion, as detailed in the next section.

DISCUSSION OF SM79-8

Using the identical finite element model, an attempt was made to evaluate the effects of a local matrix-particle decohesion on the ability of second phase particles to interact. The so-called burst model indicated that the regions of high strain would exhibit a propensity to join at much lower levels of far field loading. Consequently, the assumption was that a decohesion would also accelerate the interactive effects; but would the level of load at which such a decohesion occurs be a major variable?

Representative results are given by Figures 10-16. Figures 10 and 11 show the variation, with angular position around the particle at which the decohesion was enforced, of ε_R Figures 12 and 13 - the variation of the normalized octahedral shear stress, both sets for two orientations. Figures 14-16 indicate regions exhibiting a high level of octahedral strain in relation to the far field values.

A few words of explanation are in order at this point: Since we were and still are lacking a criterion for decohesion, the decohesion was enforced at different levels of far field strain. "Coherent" model implies no decohesion; "initial debond" implies particle-matrix surface is separated but not opened prior to application of any load; "debond on 10" - small local plastic yielding present prior to debonding; "debond on 20" - plastic flow throughout the model prior to debonding; "debond on 15" - intermediate load level to "debond on 10 and 20." Additionally, the extent of the debond is approximately 1/12 of the circumference of the second phase particle.

The conclusions drawn from the analysis were that the orientation of the particle-particle axis with respect to the load axis was a very important

variable, lateral constraint less so. Futhermore, the more plastic flow present at the time of debond, the more pronounced the tendency for the regions of high octahedral strain to propogate. Finally, that the level of interaction seen for any analysis with a decohesion introduced was substantially greater than the level of interaction seen in either the corresponding "cohesive" or "burst" model case.

DISCUSSION OF THE MODEL AND ITS LIMITATIONS

The finite element model discussed so far, shown in Figures 3-5, has severe limitations for the purposes intended, although this is not obvious from the results presented and discussed previously. Elastic analyses, such as can be inferred from the lowest curves on Figures 6 and 7 are not indicative of the quality of results obtainable from the model for a plastic analysis. That, however, is essentially due to the nature of plastic flow itself. Once a region has yielded, further straining tends to accrue there, as opposed to necessarily yielding the surrounding regions. In a finite element sense, an element is considered as yielded if the yield criterion is exceeded at the centroid of a constant strain triangle i.e. a binary decision. Consequently, if a large element extends into regions of both high and low stress, a good possibility exists of its not yielding even if nearly 50% of the region is experiencing stress levels high enough to initiate plastic flow. Such a result may appear in Figures 8 and 9 since there is no apparent reason for the particular distribution of elements not exhibiting extensive strains, save for their having yielded later than their neighboring smaller elements.

The bipolar coordinate scheme used to facilitate the modeling introduces several other geometric flaws. The element size gradations that exist are

prejudicial since along the particle-particle axis the elements remain rather small between the particles, but not as much in other directions emanating from the particles. In effect, the plastic flow has been forced to occur between the particles. Similarly, there is also an angular bias built in around each particle - that being that the smallest elements around the particle occur directly on the particle-particle axis closest to the neighbor particle. In short, the region most likely to yield first occurs between both particles, and the path of least resistance to plastic flow lies directly towards the neighbor particle.

The existence of element size gradations in the direction of the neighbor particle is obvious from Figure 4, as is the angular size distribution. Whether such gradations are fatal to the analyses performed is definitively answered by Figures 17-19. These three figures are directly analogous to Figures 14-16 with the exception that the results shown in Figures 17-19 are taken from analyses where matrix material properties were substituted in the region normally associated with the neighbor particle. That is, Figures 17-19 are for a one-particle model. It should be mentioned that even though these results show regions over which the normalized octahedral shear strain exceeds far field values by 5% (Figures 14, 15, 17, and 18) and 10% (Figures 16 and 19) the entire region has yielded. Quite clearly then, if Figures 14 and 17, 15 and 18, 16 and 19 are viewed as pairs, the findings - with some small local perturbations - are identical! Consequently, the conclusion must necessarily be that the analyses have not been overly sensitive to the presence of a second, second-phase particle with second phase material properties, but rather the results appear dependent and quite sensitive to the finite element model itself. Hence the model must be rejected!

NEW MODEL AND INDICATIVE RESULTS

Having shown the bipolar modeling to be unacceptable in the previous section, we embarked on devising a new model. A number of considerations serve both as guides and constraints. The requirements and limitations we must address are:

1) A clearly defined 1:1 check case comparing single particle results to multiple particle results must be available

   a) in a model sense this is easily conceivable and must be easily obtainable

   b) on an exitation level the question that arises and still needs a definite answer is - is the comparison made on equal stress levels or equal far field strain levels?

2) Minimization, if not elimination of element size gradations. There are two distinct gradations, i.e., angular and radial, both of which need to be kept in mind.

3) The ability to vary orientation of the particle-particle connection axis vis-a-vis the load axis must exist.

4) The ability to vary L/D (distance between particles to diameter ratio) must be easily attainable.

5) Points 1-4 to be met without excessive computational cost.

The scheme settled upon attempts to consider all of the requirements established, and has done so with some level of success.

In order to keep the model size within limits and preserve the ability to vary L/D, a simple coarse to fine substructure technique is employed. The coarse or matrix model is shown in Figure 20, where the cell along which displacements are carried over to the fine or particle model is indicated by the heavy point. Figures 21 and 22 indicate how the L/D ratio can be varied from two to four approximately. The L/D is approximate as each particle is modeled as a square, whose area is then converted into a circle of equivalent area yielding a diameter (D). L is measured from center to center.

A single particle problem is analyzed by substituting second phase material properties into only the center square region darkened in Figure 22. The single particle case is the reference case, to which all further multiple particles cases must be compared. The comparison is imperative since the question being asked is: to what extent are the high strain regions altered due to the presence of neighboring particles?

The particle model is presented in Figures 23 and 24 in its actual size and configuration, and an enlargement, respectively. The model as presented can easily offer two distinct length to diameter ratios i.e. L/D = 2 and L/D = 4. Furthermore, larger length to diameter ratios can be designed by simply decreasing the size of the particle itself on the matrix model. This does, however, actually create new finite element models, which we have chosen not to depict at this time. In fact, we have dealt solely with the L/D = 2 model, trying to ensure that it performs sufficiently well for our needs. The close spacing is a result of a change of perspective. Since the previous analyses dealt with L/D~11 1/2, and were somewhat unsuccessful, it was decided that a more reasonable approach, especially considering the difficulties encountered with the model itself, is to analyze a situation where heavy interaction is certain to occur. Hence the close spacing.

From Figure 24, it is obvious that angular size gradations do not exist. However, modest radial size gradients are present. Essentially this is due to computer limitations. We recognize and acknowledge that the model is a compromise. However, we also believe it to be vastly superior to the previous model.

Variations of the particle-particle axis with respect to the load axis has been approached from a slightly different viewpoint than previously. The now discarded model actually consisted of five different models, three of which are

given by Figure 3. We have chosen to effect the rotation of load axis with respect to particle-particle axis through the input boundary conditions. That is, instead of imposing uniaxial tension on the model shown in Figure 20 vertically, we can impose boundary conditions to be those of say 45° off vertical on the model. Through transformation equations any off angle (from vertical) boundary conditions can be calculated.

The microstructure we are modeling contains cylindrical second phase particles, which should be modeled as circles in two dimensions. Since the matrix model, Figure 20, models the second phase particles as squares, some justification is in order. During the attempts to create a new model, we had designed a very similar model to that presented here, although containing somewhat less detail. Using that model we analyzed the problem of a hole in an elastic plate in tension. The problem was solved in two distinct ways that are:

1) direct loading of the fine model, and

2) loading of the matrix model, and subsequent substructure loading, i.e., of the fine model.

The importance is two-fold. First we can compare results to well-known analytic solutions and secondly loading of the matrix model and subsequent loading of the particle model informs us of the quality of results we can obtain by an extremely crude modeling of a circular particle by a square.* Both analyses showed excellent agreement with theory. Since the material properties of the second phase are not

---

*When the boundary conditions are input on the matrix model, a square region similar to that seen on the center of Figure 20 possesses essentially nil elastic properties. The displacements are then carried onto the particle model where a circular hole is vastly better modelled.

nearly as dissimilar form the matrix as compared to nil elastic properties, we expect two material problems to show the same kind of agreement. In short, we feel justified in our approximation of a circular region, on the matrix model, to be a square.

DISCUSSION OF RESULTS - Testing of the Element Model

We have run a rather extensive list of elastic check cases which essentially are an attempt to insure that:

1) we have no built-in bias
2) we have sufficient detail on the particle model
3) we are justified and introduce no difficulties by rotating our input to simulate rotation of the particle-particle axis WRT the load axis.

We also have preliminary plastic results available which will be presented as well.

Although, from our experience, elastic results are not necessarily conclusive indicators of the quality of plastic results, it is nevertheless important to examine elastic results in some detail. Furthermore, with the present model, we can obtain a sense of the quality of our model, since we can compare single to multiple particle results. Additionally, we expect to see differences in the elastic results since L/D = 2. Therefore, a comprehensive set of elastic results are presented in Figures 25 and 26. The angular variation of σ_r/σ for various locations are given by Figures 25-32, of $\sigma_{\theta\theta}/\sigma$ by Figures 33-40, of $\tau_{r\theta}/\sigma$ by Figures 41-48. Normalized octahedral shear stress angular variations are depicted by Figures 49-56. The radial location measured from the center of the particle starts at the closest element ring in the matrix material and progresses outwards for each of the sets of data presented.

The results presented substantiate our belief that the present model is a vast improvement over the previous model. The darkened symbols indicate single particle results for various angles of far field tension with respect to particle-particle axis. Since these points fall essentially onto one single curve, we can safely conclude that our method of simulating differing particle-particle axis orientations WRT the loading axis through input boundary conditions introduces no discernable errors.

Since these analyses were performed for a particle spacing given by L/D=2, we expect to see differences in the stress components once we analyze the multiple particle cases. These differences do appear as well. In general, from Figures 49-56 we can say that the stress level is somewhat higher i.e., clearly distinguishable from the single particle results. The scatter of the data is somewhat greater for the multiple particle results, than the single, but not objectionably so.

A rather interesting event is noticeable on Figures 49-56 for the multiple particle data. The nominal average value for τ_{oct}/τ_{lim} is on the order of .28, maximum ~.32. Now as we proceed radially outwards from the particle, the trend that appears is for the peak values of τ_{oct}/τ_{lim} to remain roughly constant, while the minimum values tend to increase. Certainly the fact that the curves tend to flatten out is not surprising - in fact for single particle results at a large enough distance we expect the τ_{oct}/τ_{lim} curve to be flat. Nevertheless, why do the 'valleys' get deeper in Figure 49, rather than the peaks becoming higher in comparison to Figure 56?

For our purposes the more important question is how does this particular model perform when plastic yielding occurs? Preliminary results have been obtained and are presented in Figures 57-62. These figures graphically depict regions

of high strain (measured by the octahedral shear strain) for both single particle and multiple particle analyses. The figures represent data obtained for an analysis where the far field loading is presumed tension at 22.5° from vertical on the matrix model, at an accumulated strain level of ~4%. There are very distinct differences between single and multiple particle results. On Figures 57 and 58 the elements exceeding far field strain levels by 5% are darkened and a shift is apparent from extensive yield in the load line direction (Figure 57) to preferred yield towards the neighbor particle (Figure 58). In fact on the basis of the 105% characterization, the particles have already connected. As we use a stricter characterization - 107% for Figures 59 and 60, and 110% for Figures 61 and 62, of course the high strain regions become progressively smaller. However, in all cases the effect of multiple particles is clearly visible.

One note of caution should be mentioned concerning the results given on Figures 57-62. The results are not precisely symetrical as we have depicted the data. The principal reason is since the tension axis is at 22.5° there is no precise symetry of element distributions. For example, had we chosen to have the tension axis at a multiple of 30°, the elements would be distributed precisely symetrically about the tension axis. Clearly, a polygonal representation for a circle has a finite number of such symetry lines. Nevertheless, had the load been applied in such a symetrical direction, we would expect symetrical results. In addition, the use of a 5% exceedance of the strain criteria is rather arbitrary and does not account for the minor numerical variations which occur in any analysis of the type presented.

An interesting observation can be made by viewing Figures 62, 60 and 58, in that order. Although, we are then viewing a progression of less severe criteria for the determination of high strain regions, the following extension also applies. Since the exceedance is highest on Figure 62 it can be assumed that these regions necessarily yielded first. The new regions darkened on Figure 60 yielded intermediately, and the regions darkened only on Figure 58 yielded last. The point is that the second phase particles which appear to have connected on Figure 58, have done so by 'growing' high strain regions from the neighbor particle, not radially out from the particle represented by the center of the particle model. Simply stated, information at the boundaries of the particle model is propogated inwards even though it is harder to do, than propogate plastic zones out from the particle, since those elements tend to be much smaller. It is to be noted, that this observation per se, does not indicate any problem - it is, however, interesting.

In conclusion, we believe the model presented here, substantiated by the results obtained and presented here, is a tremendous improvement over the previous model. We have paid great attention to eradicating the flaws of the previous model, and have succeeded. We believe that the model will allow meaningful analyses to be performed that will readdress the issue of interaction of second phase particles, and its importance.

REFERENCES

1. Swedlow, J. L. and G. B. Sinclair, "Two Cases of Inclusion - Inclusion Interaction in a Ti Alloy," Report SM77-7, Department of Mechanical Engineering, Carnegie-Mellon University (October 1977)

2. Batarags, R. R. and J. L. Swedlow, "The Effect of a Local Matrix-Inclusion Decohesion On The Interaction Between Inclusions In A Ti Alloy," Report SM79-8, Department of Mechanical Engineering, Carnegie-Mellon University (April 1979)

3. Swedlow, J. L. and R. E. Smelser, Materials and Science Engineering, 40 (1979) 139-140.

Figure 1. Presumed stress-strain curve for α phase. $E = 17.5 \times 10^6$ lb/in^2 and $\sigma_{lim} = 115 \times 10^3$ lb/in^2

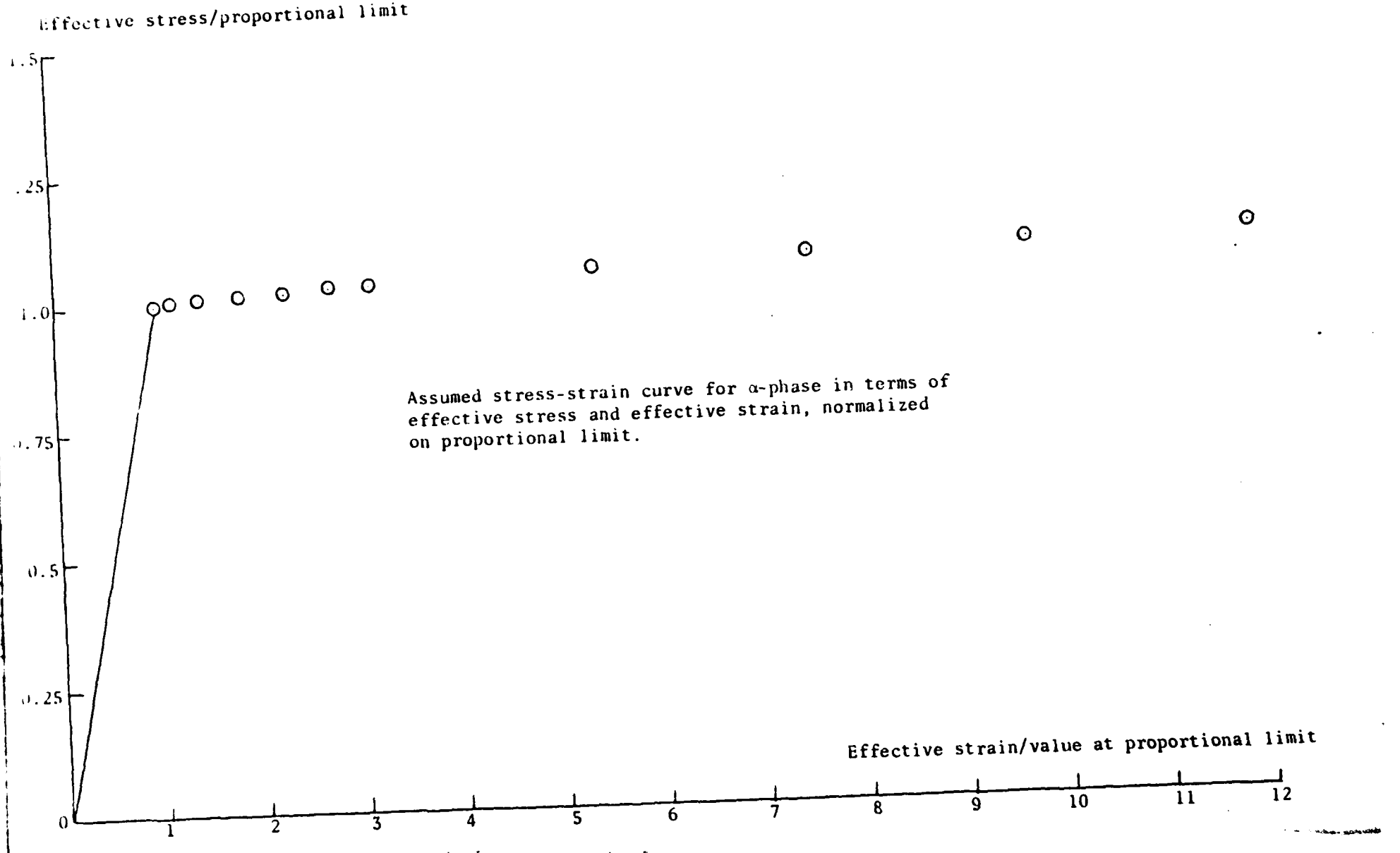

Figure 2. Presumed stress-strain curve for β phase. $E = 13.0 \times 10^6$ lb/in^2 and $\sigma_{lim} = 130 \times 10^3$ lb/in^2

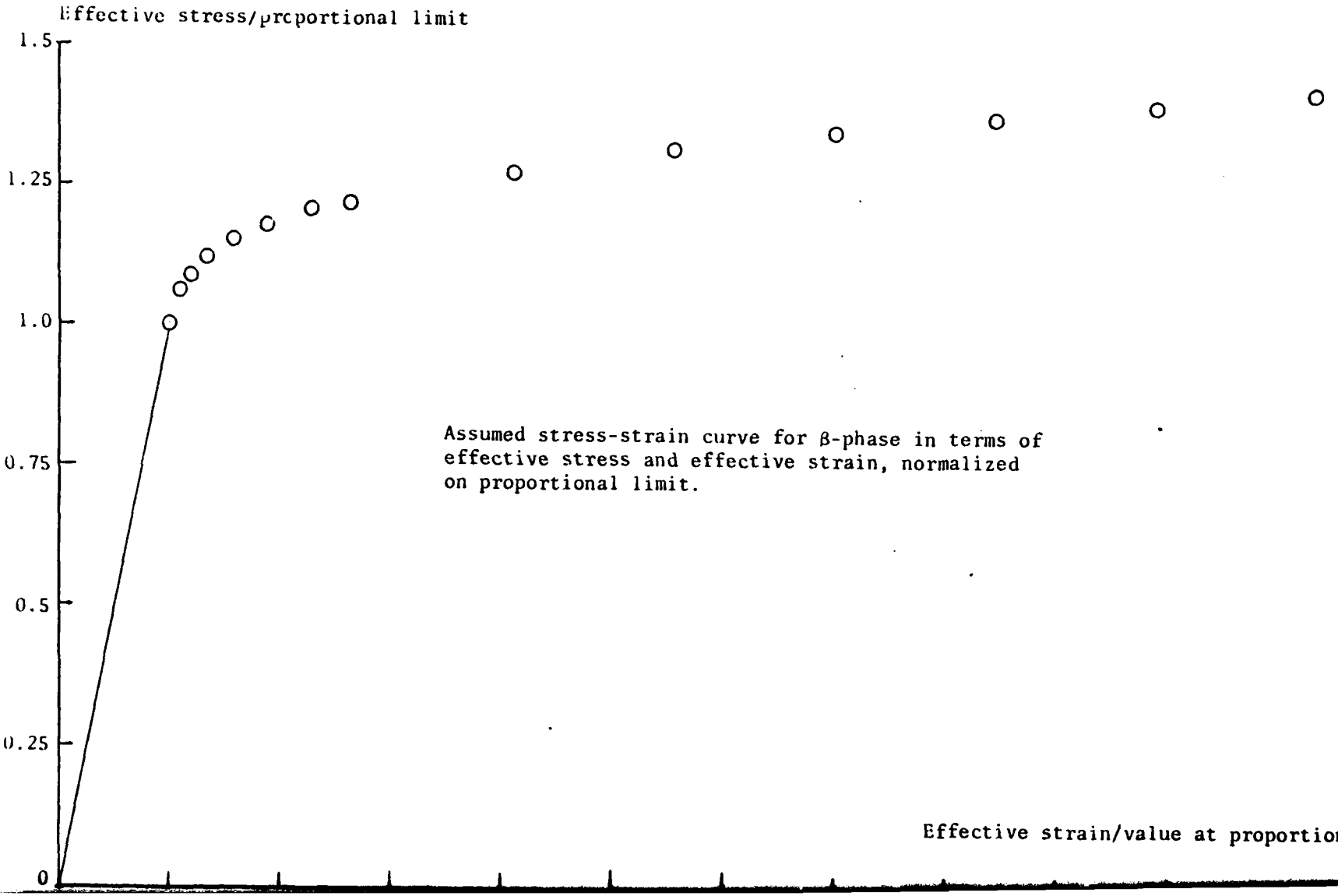

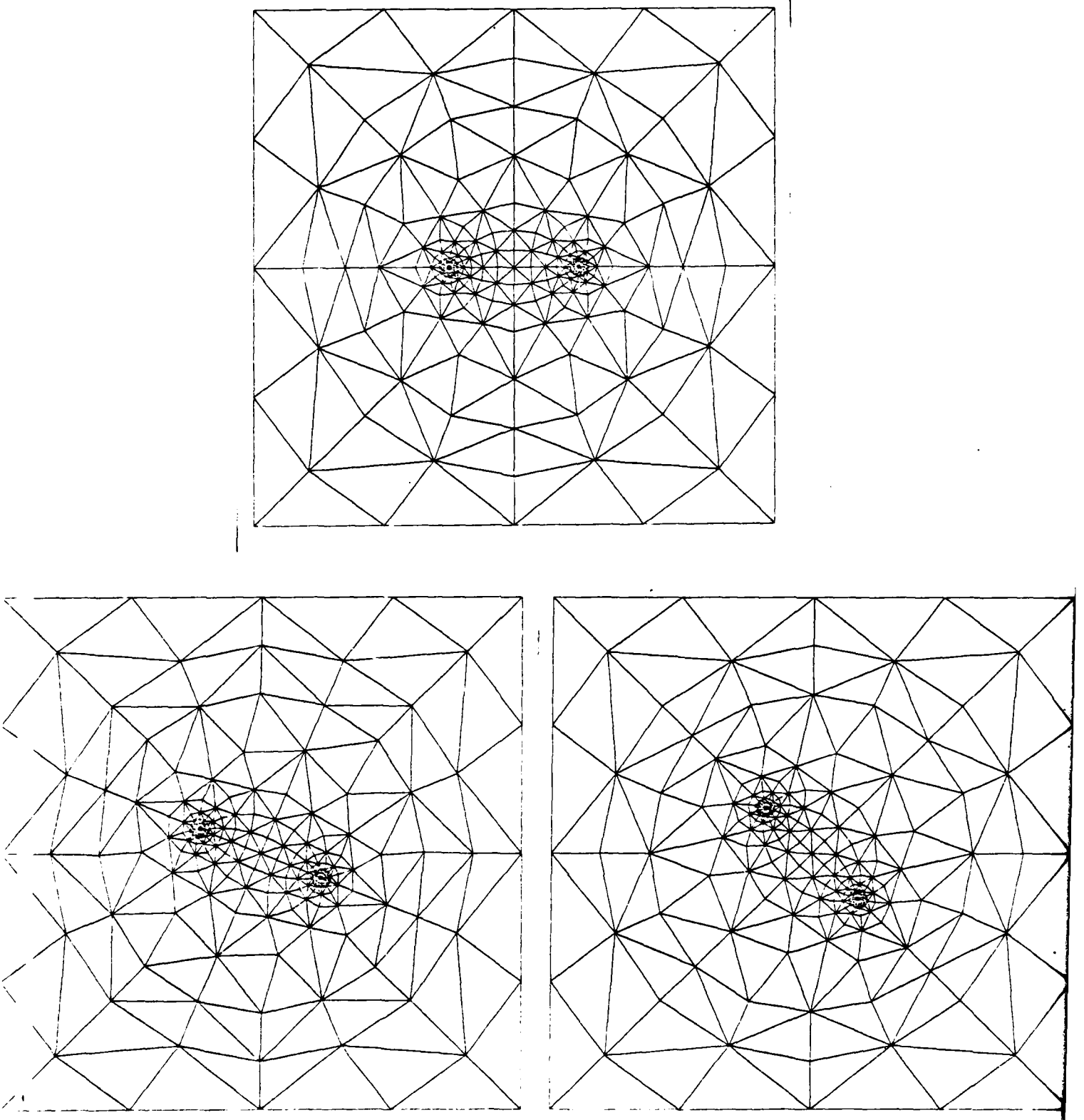

Figure 3. Bipolar element model, showing 3 of 5 available rotations of particle-particle axis. Excitation is vertical, constraint horizontal.

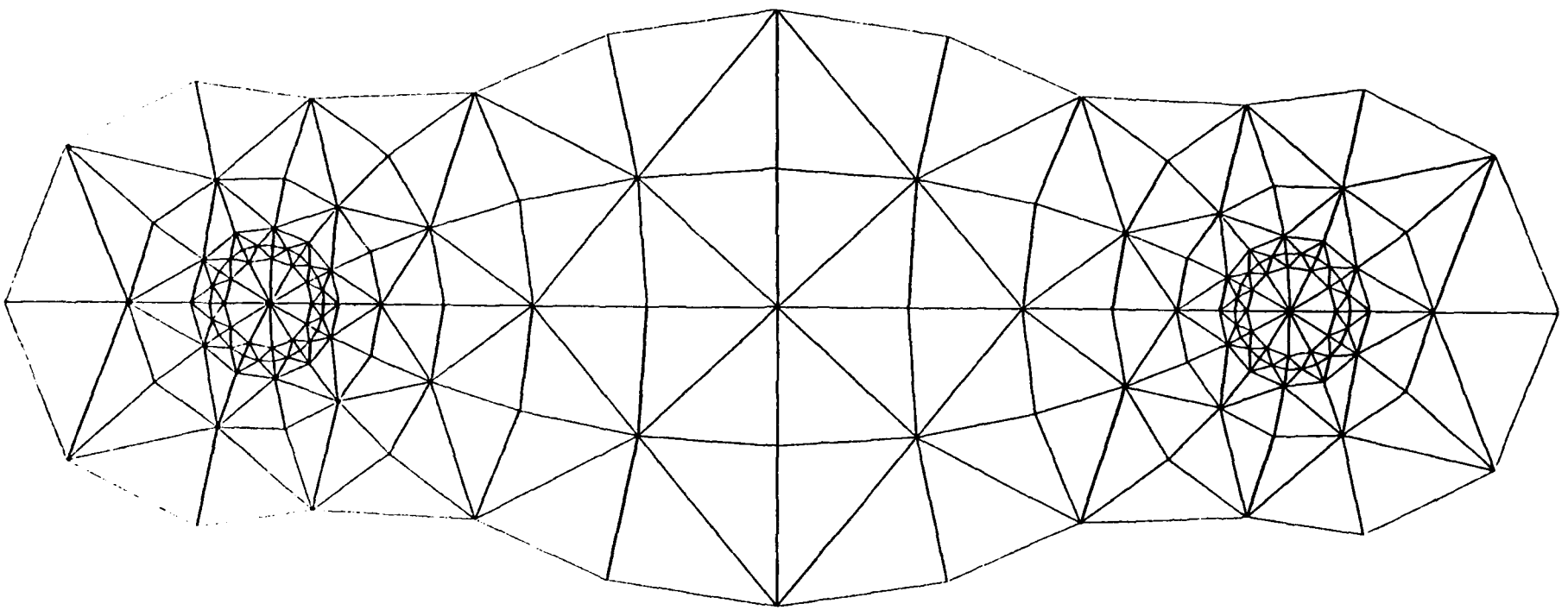

Figure 4. Enlargement of central region of bipolar map.

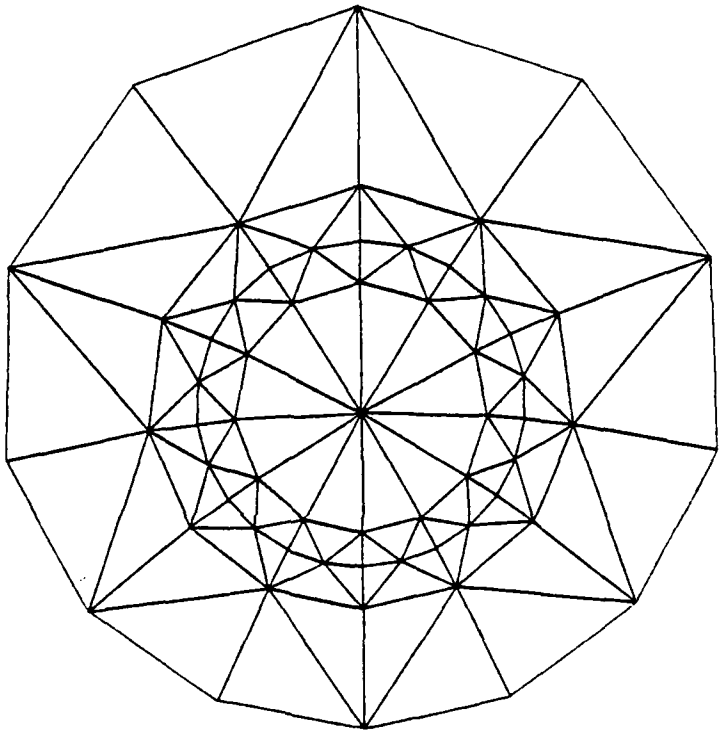

Figure 5. Enlargement of single particle and region directly contiguous.

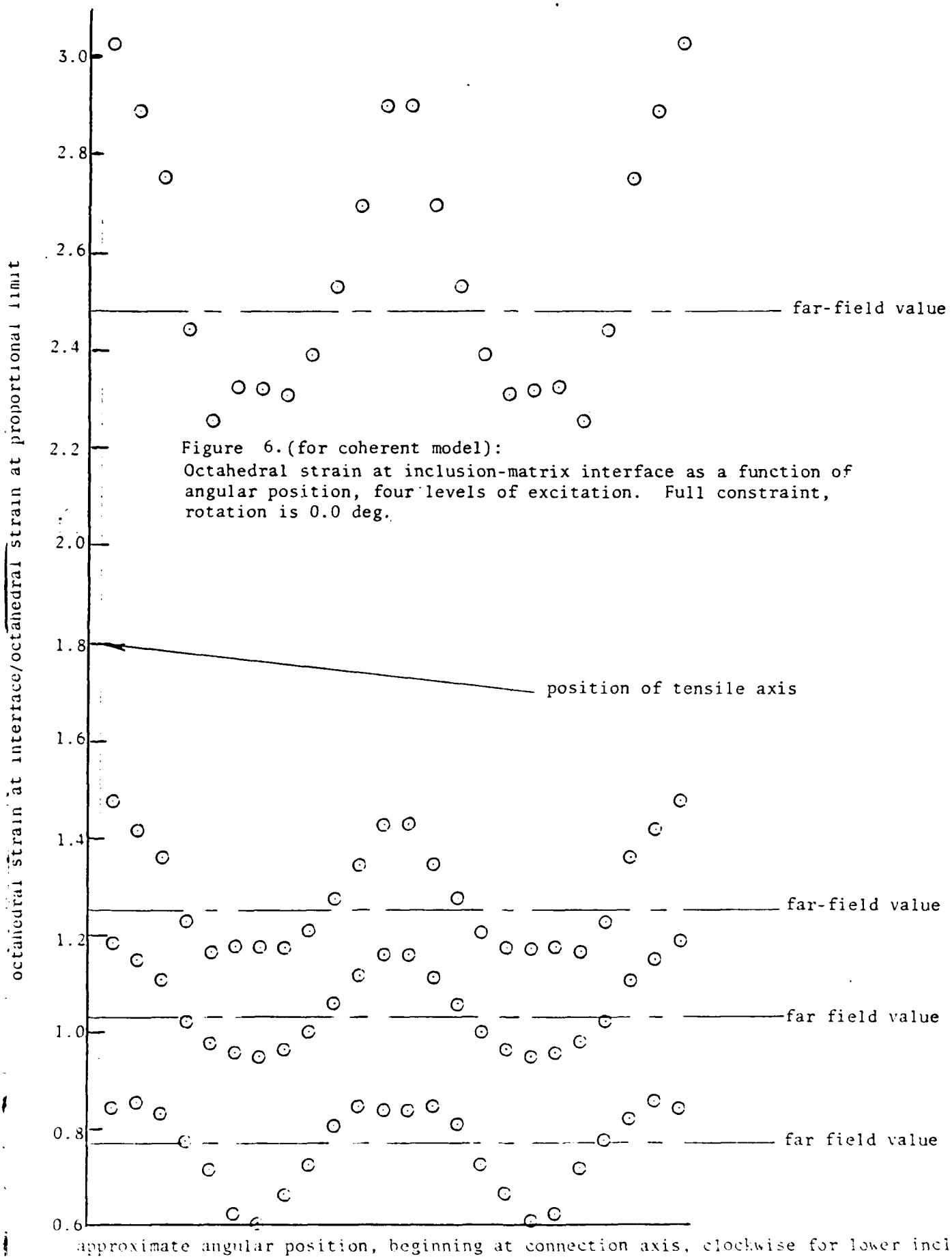

Figure 6.(for coherent model):
Octahedral strain at inclusion-matrix interface as a function of angular position, four levels of excitation. Full constraint, rotation is 0.0 deg.

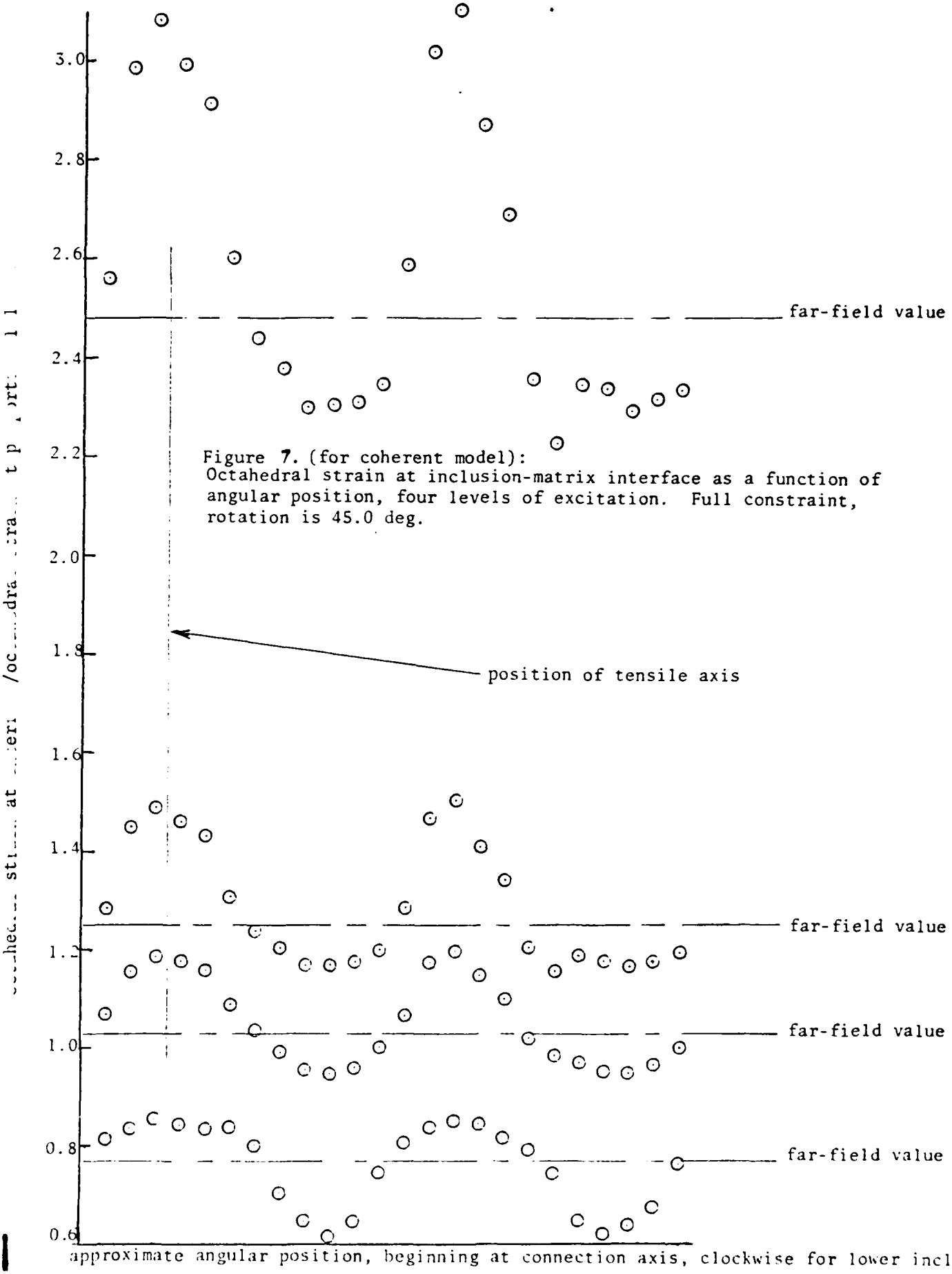

Figure 7. (for coherent model):
Octahedral strain at inclusion-matrix interface as a function of angular position, four levels of excitation. Full constraint, rotation is 45.0 deg.

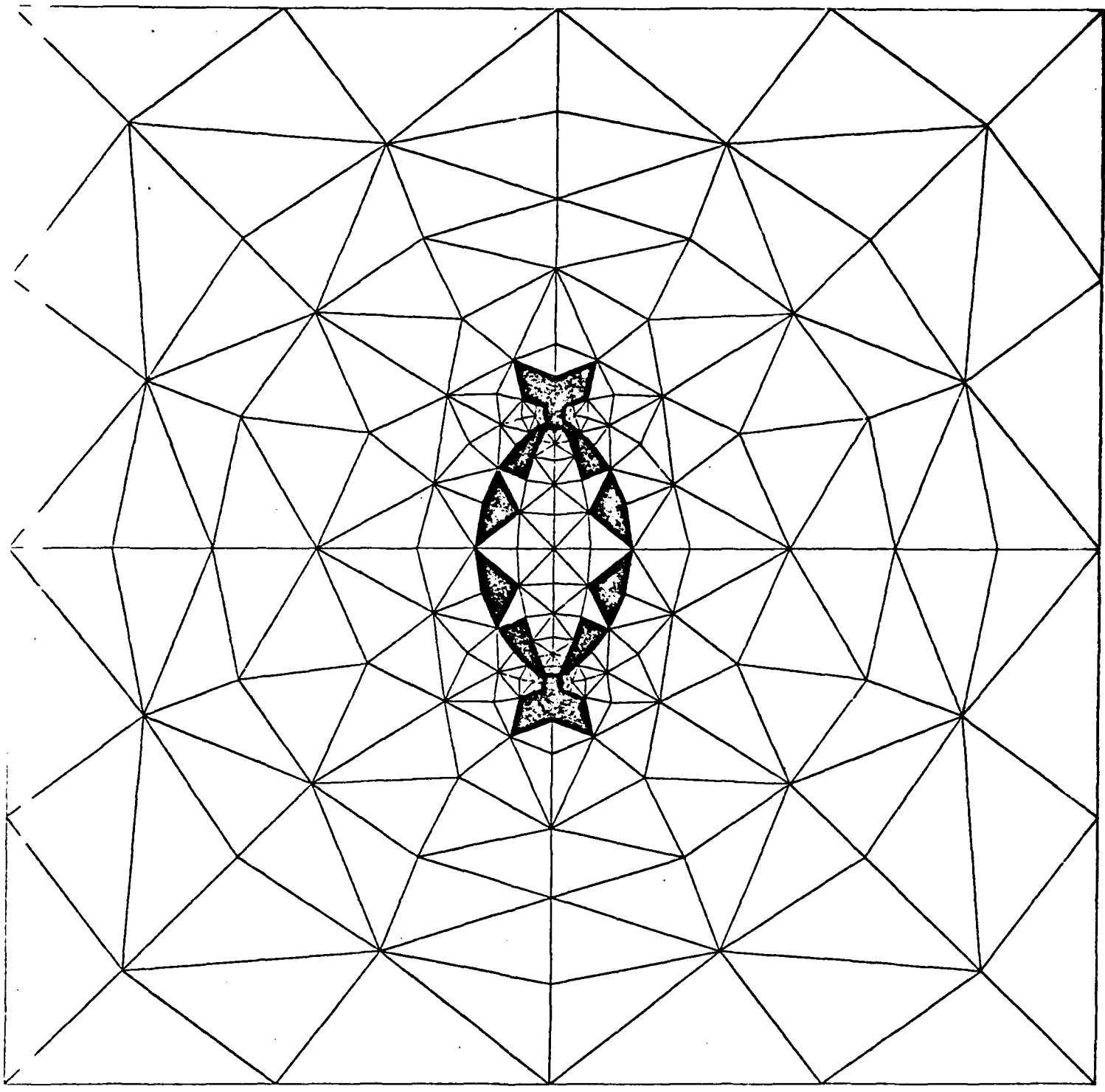

Figure 8. Regions with greatest propensity for extensive strain, full constraint, rotation is 0.0 deg, coherent model

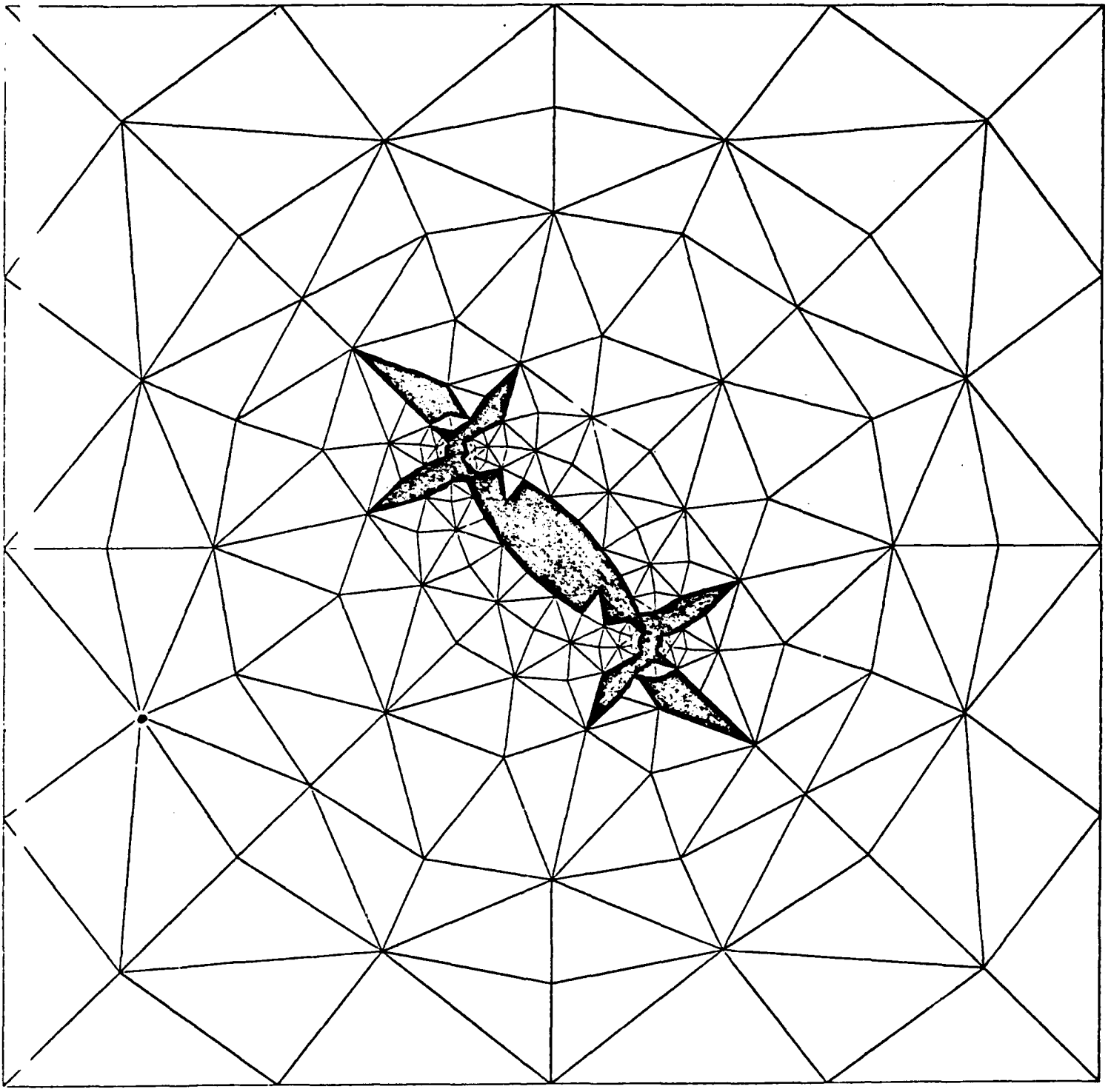

Figure 9. Regions with greatest propensity for extensive strain, full constraint, rotation is 45.0 deg, coherent model

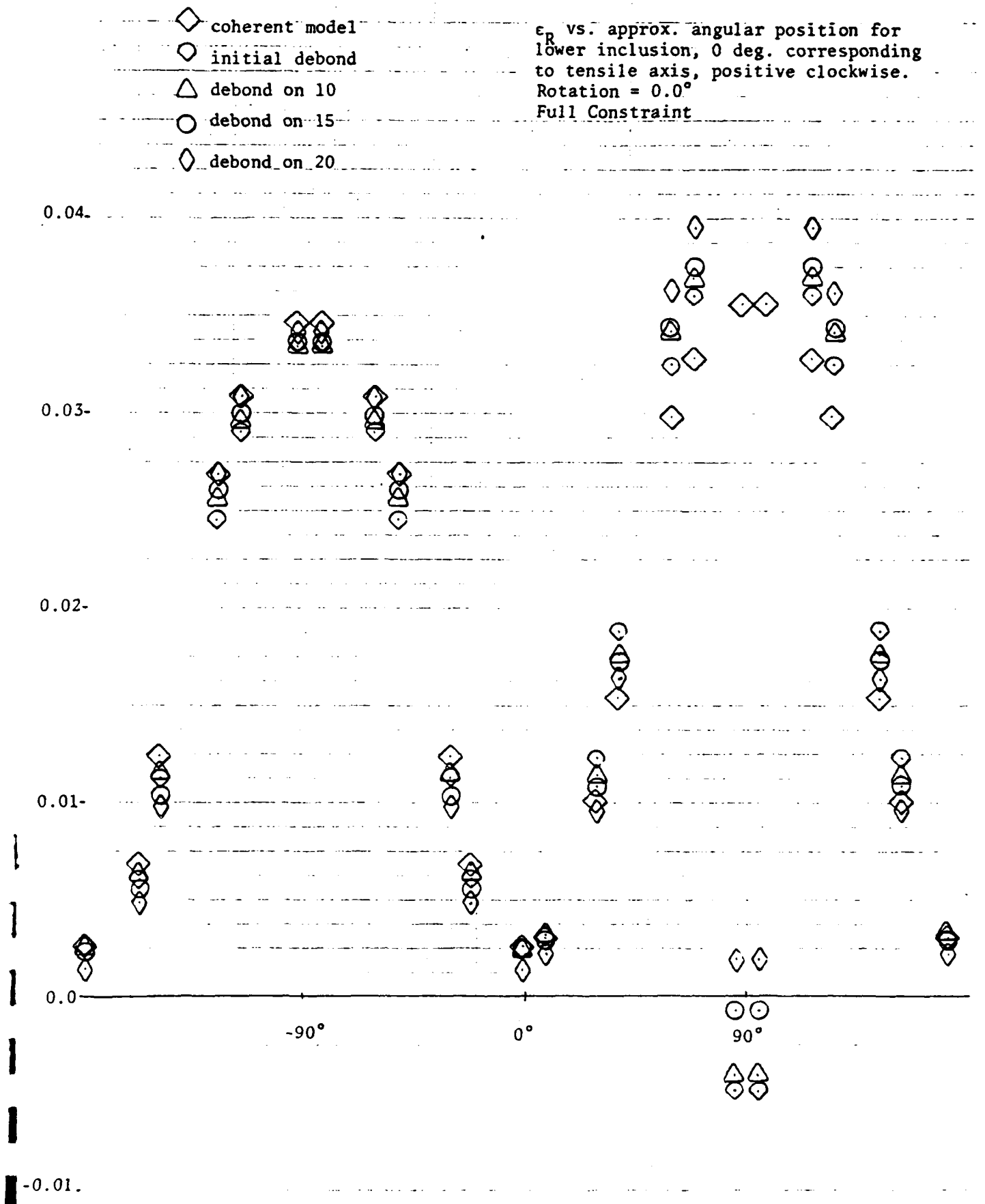
coherent model
initial debond
debond on 10
debond on 15
debond on 20
ϵ_R vs. approx. angular position for lower inclusion, 0 deg. corresponding to tensile axis, positive clockwise.
Rotation = 0.0°
Full Constraint
0.04
0.03
0.02
0.01
0.0
-0.01
-90°
0°
90°

Figure 10.

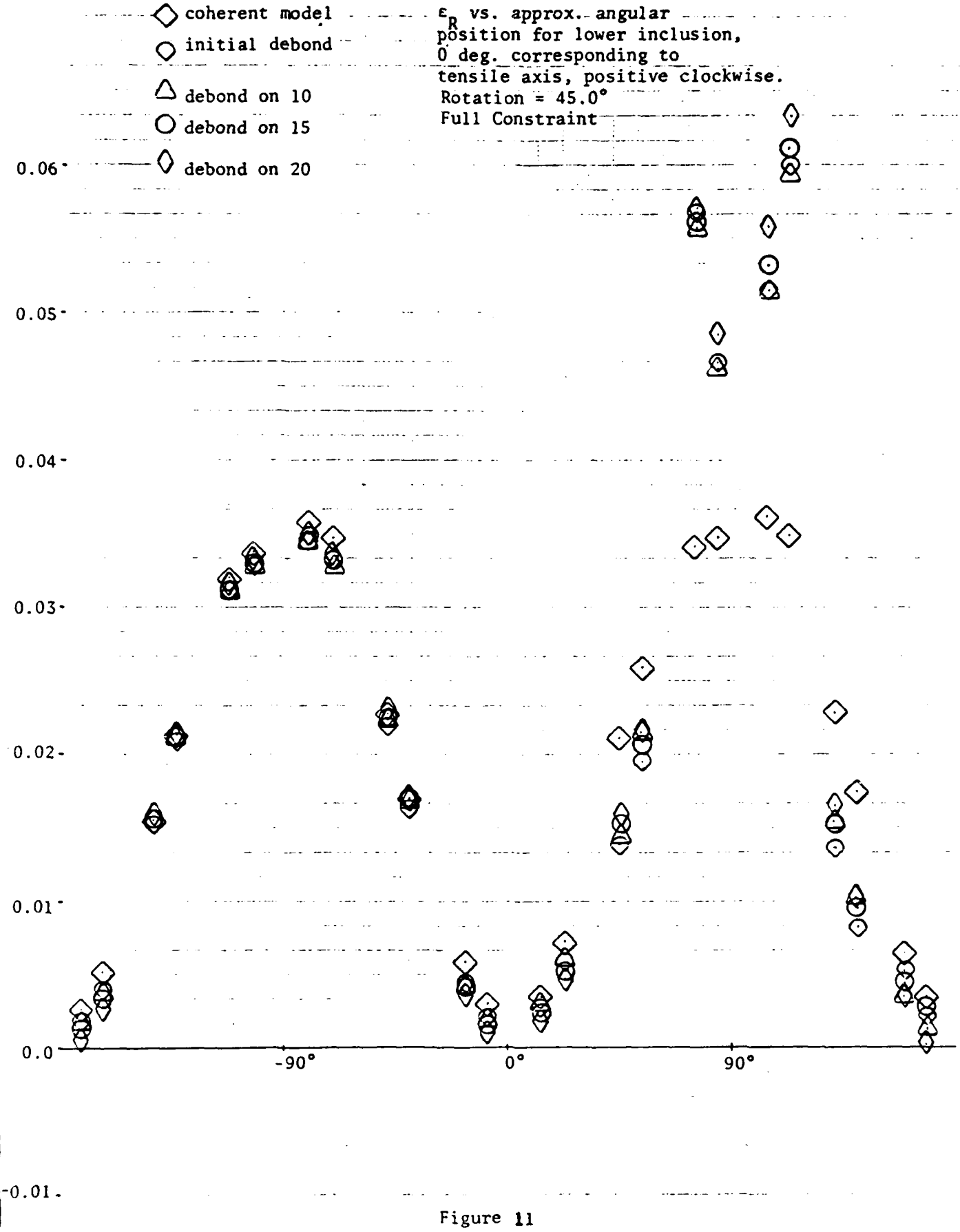
coherent model
initial debond
debond on 10
debond on 15
debond on 20
ε_R vs. approx. angular position for lower inclusion, 0 deg. corresponding to tensile axis, positive clockwise.
Rotation = 45.0°
Full Constraint
0.06
0.05
0.04
0.03
0.02
0.01
0.0
-0.01
-90°
0°
90°

Figure 11

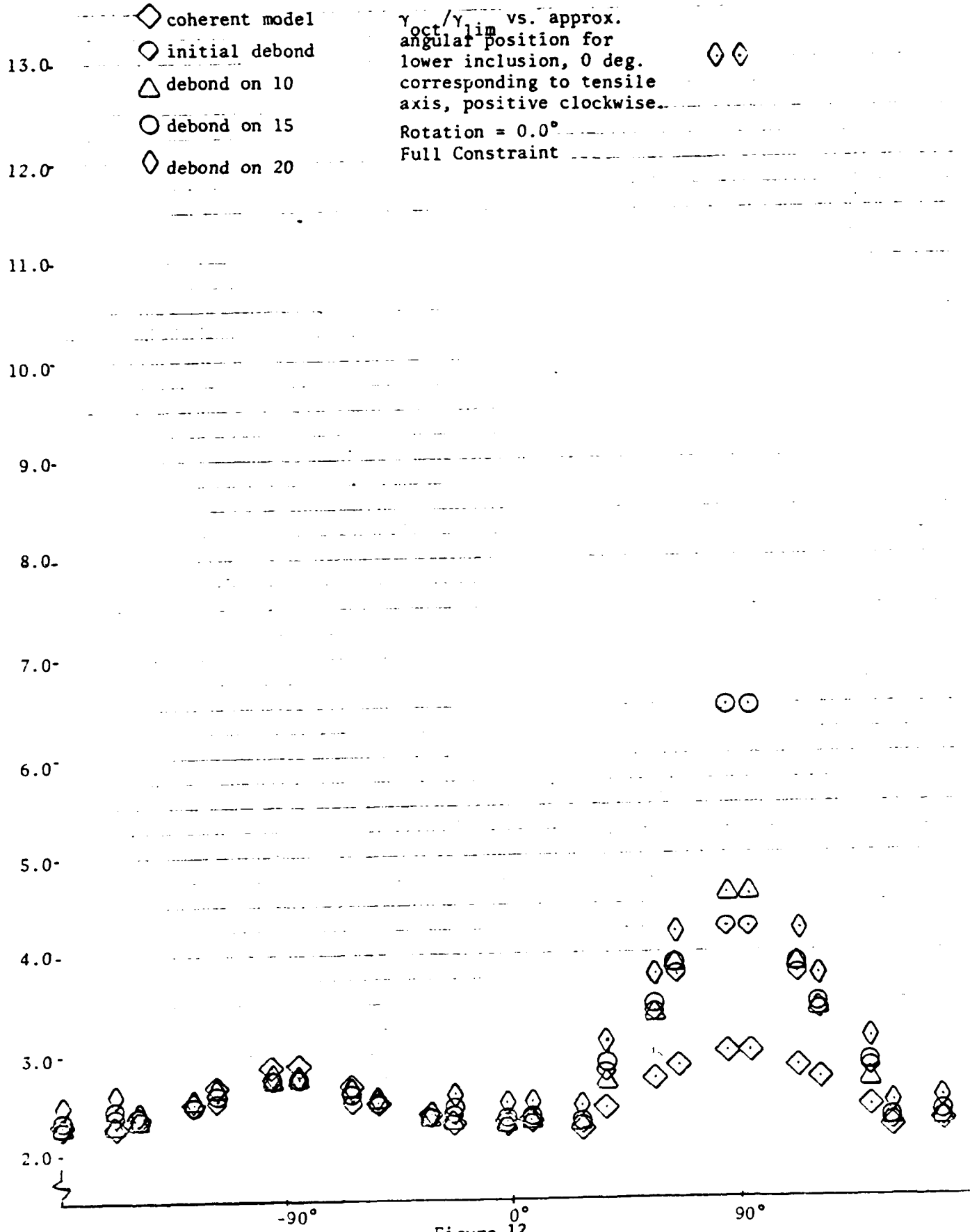
coherent model
initial debond
debond on 10
debond on 15
debond on 20
$\gamma_{oct}/\gamma_{lim}$ vs. approx. angular position for lower inclusion, 0 deg. corresponding to tensile axis, positive clockwise.
Rotation = 0.0°
Full Constraint
13.0
12.0
11.0
10.0
9.0
8.0
7.0
6.0
5.0
4.0
3.0
2.0
-90°
0°
90°

Figure 12.

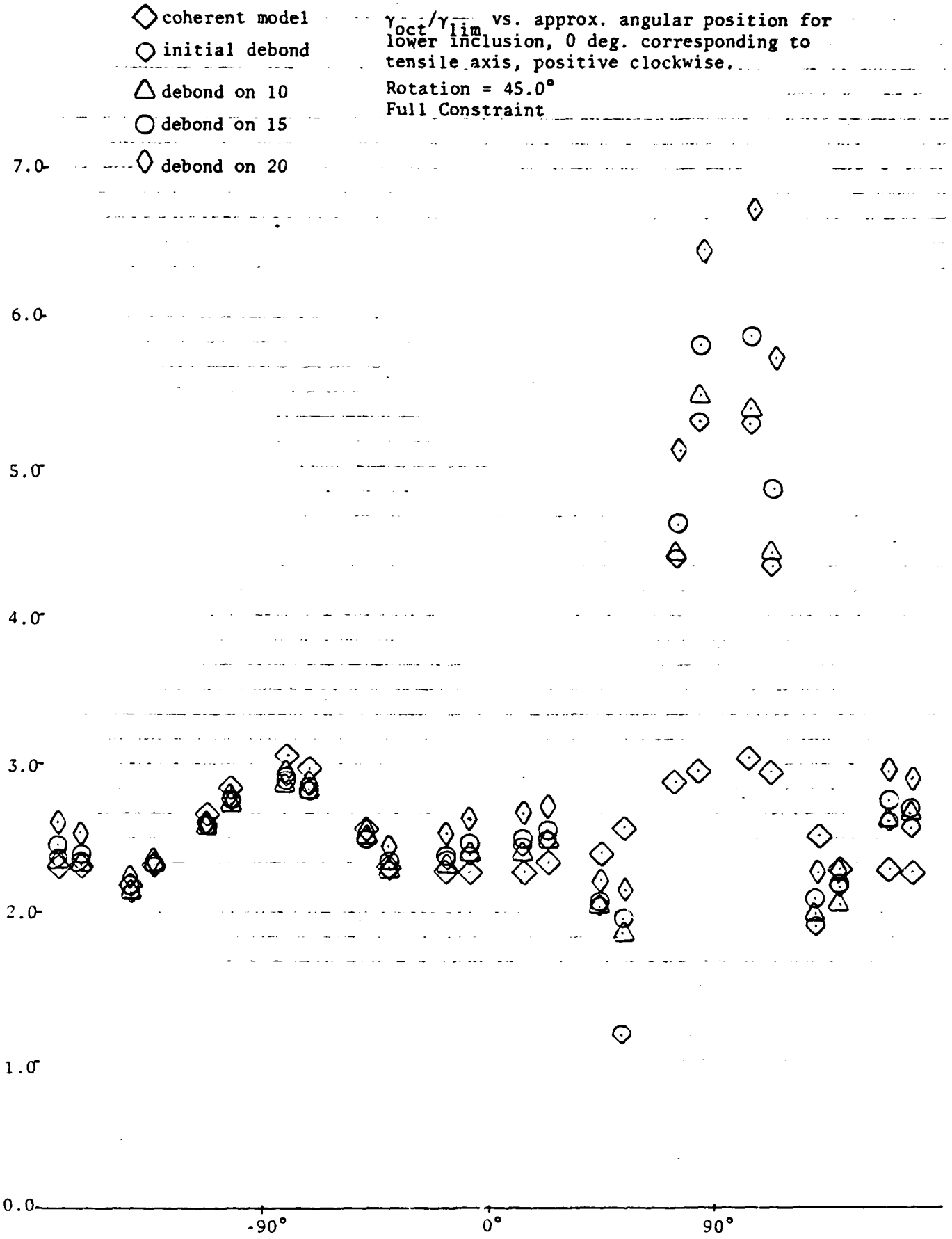
coherent model
initial debond
debond on 10
debond on 15
debond on 20
$\gamma_{oct}/\gamma_{lim}$ vs. approx. angular position for lower inclusion, 0 deg. corresponding to tensile axis, positive clockwise.
Rotation = 45.0°
Full Constraint
7.0
6.0
5.0
4.0
3.0
2.0
1.0
0.0
-90°
0°
90°

Figure 13.

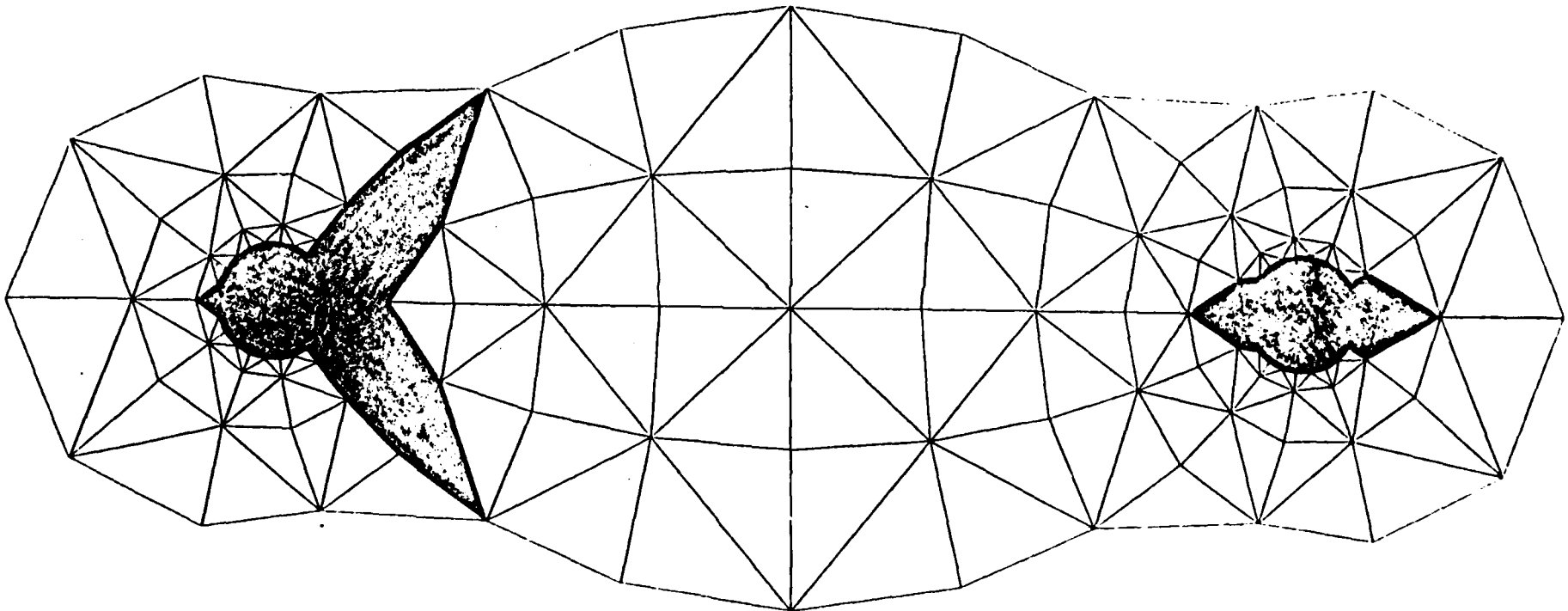

Darkened Regions Indicate

$$\frac{\gamma_{oct}}{\gamma_{lim}} > \left.\frac{\gamma_{oct}}{\gamma_{lim}}\right|_{\text{far field}} \times 1.05$$

Debond on 15, Rotation = 0°, Full Constraint

Figure 14.

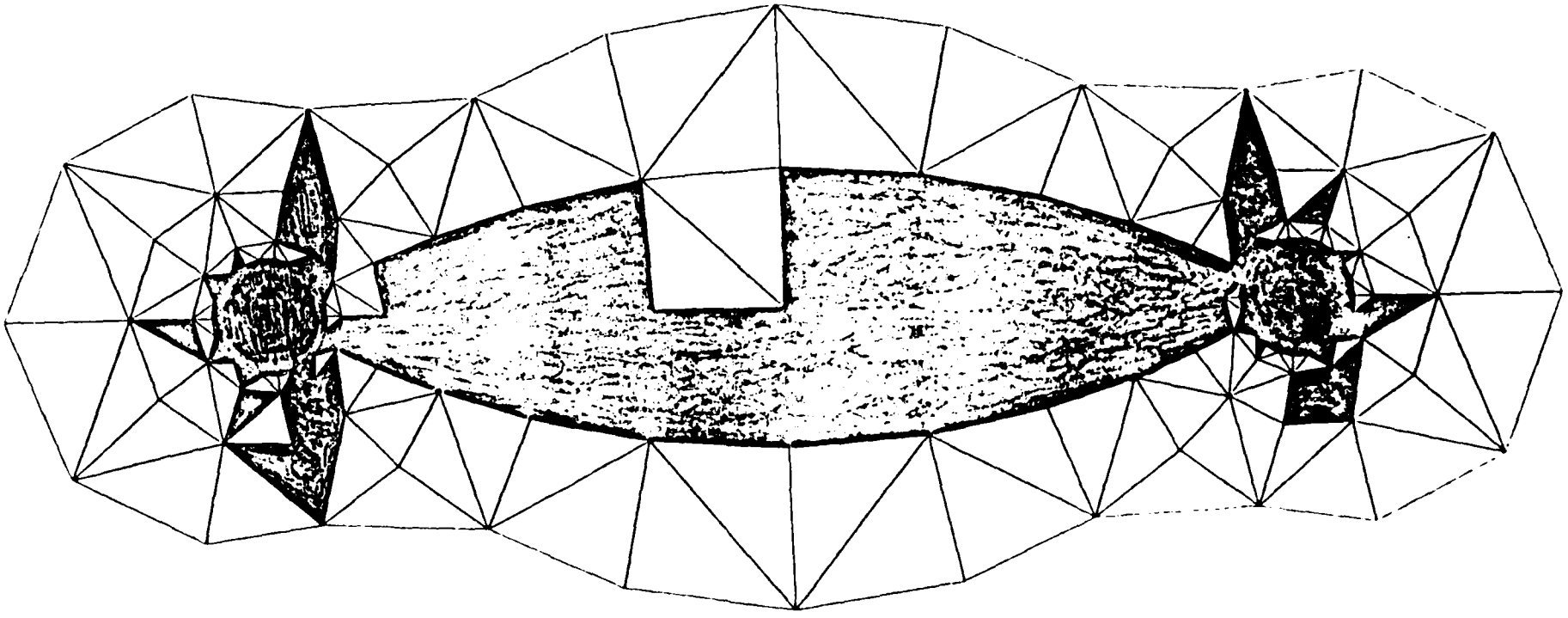

Darkened Regions Indicate

$$\frac{\gamma_{oct}}{\gamma_{lim}} > \left.\frac{\gamma_{oct}}{\gamma_{lim}}\right|_{\text{far field}} \times 1.05$$

Debond on 20, Rotation = 45°, Poisson Constraint

Figure 15

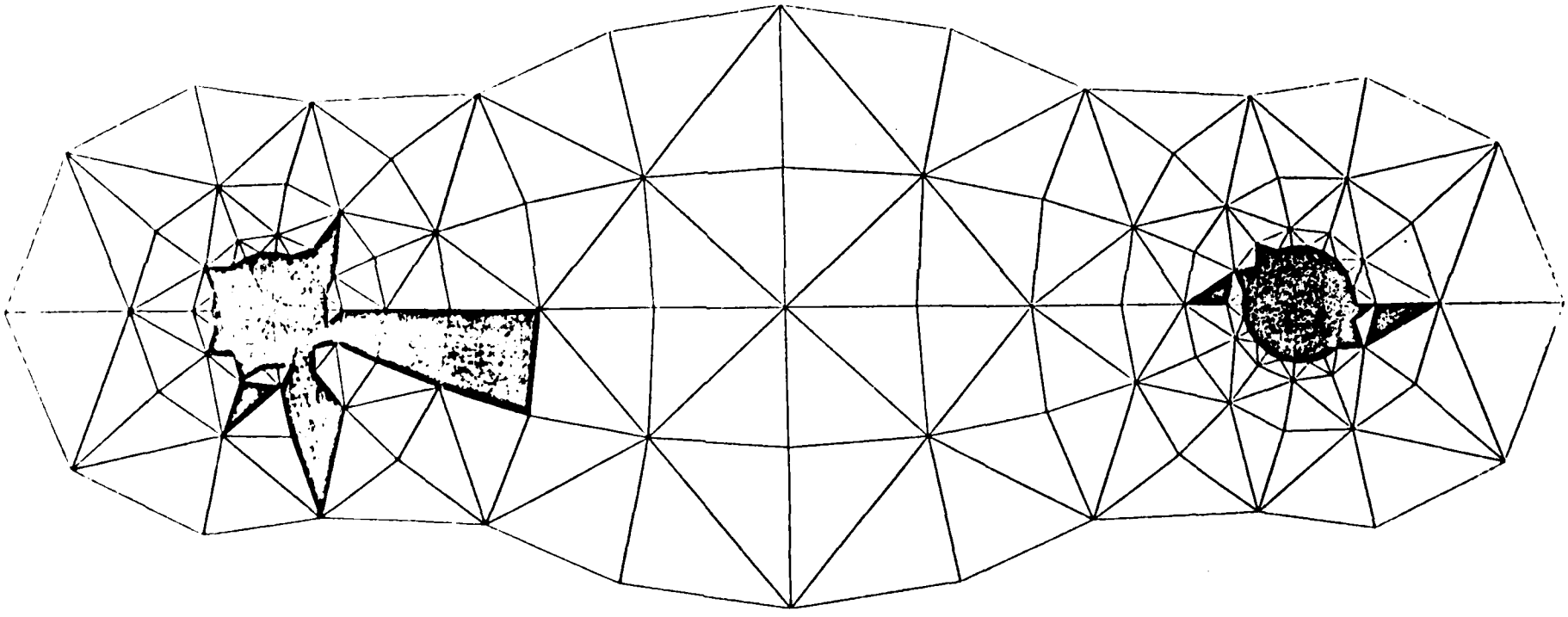

Darkened Regions Indicate

$$\frac{\gamma_{oct}}{\gamma_{lim}} > \left.\frac{\gamma_{oct}}{\gamma_{lim}}\right|_{\text{far field}} \times 1.10$$

Debond on 20, Poisson Constraint

Figure 16.

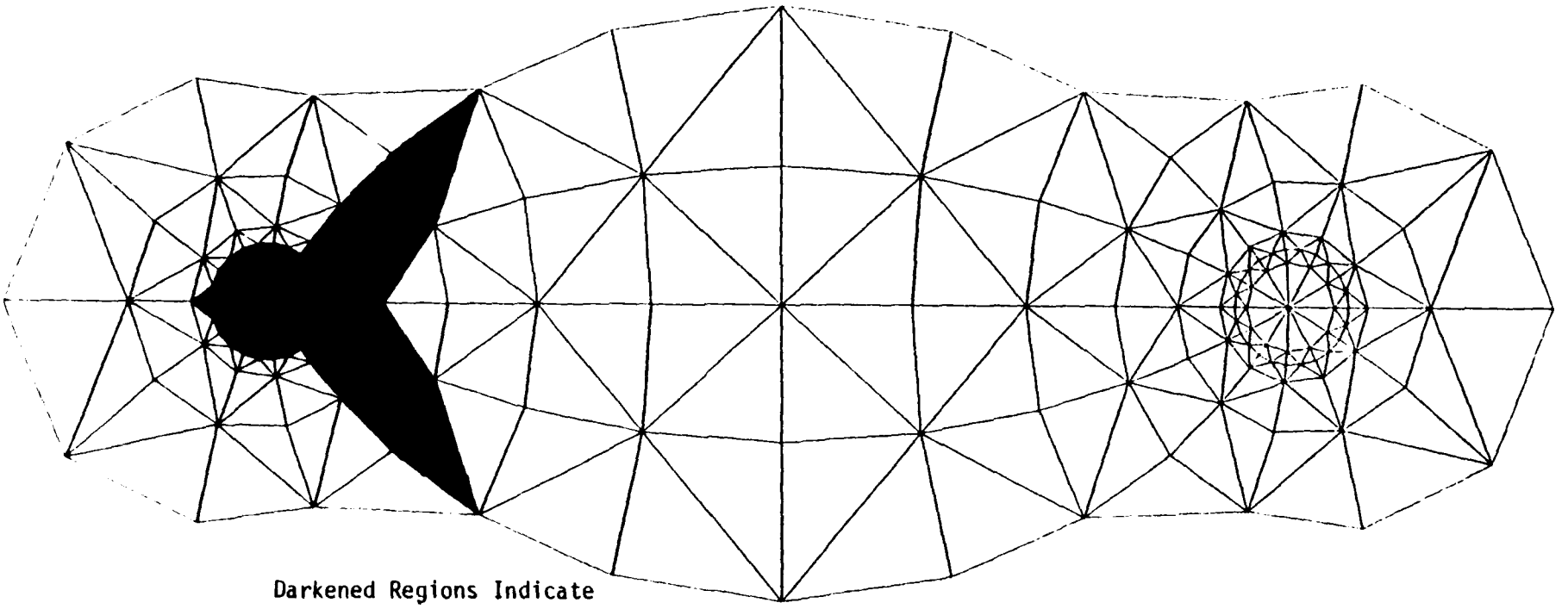

Darkened Regions Indicate

$$\frac{\gamma_{oct}}{\gamma_{lim}} > \left.\frac{\gamma_{oct}}{\gamma_{lim}}\right|_{\text{far field}} \times 1.05$$

Debond on 15, Rotation $\theta=0^{\circ}$, Full Constraint, Single Particle

Figure 17.

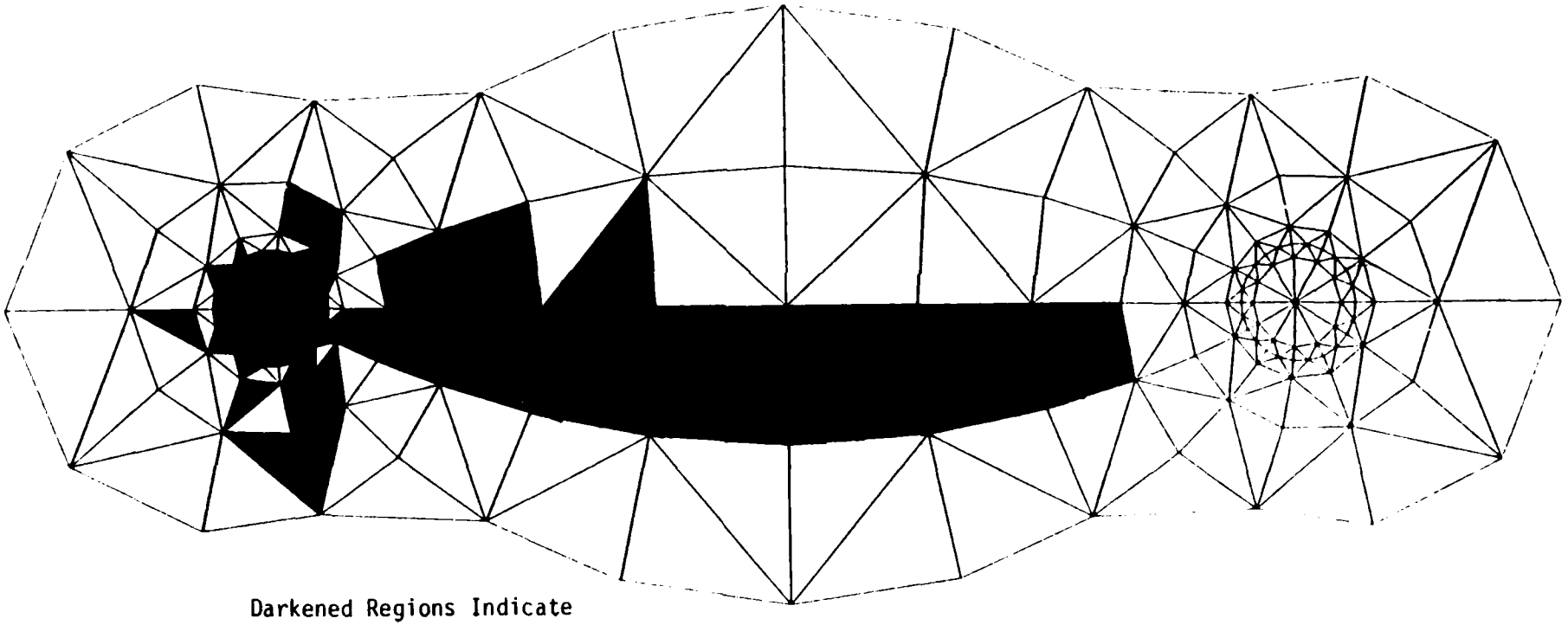

Darkened Regions Indicate

$$\frac{\gamma_{oct}}{\gamma_{lim}} > \left.\frac{\gamma_{oct}}{\gamma_{lim}}\right|_{\text{far field}} \times 1.05$$

Debond on 20, Rotation=45.0°, Poisson Constraint, Single Particle

Figure 18.

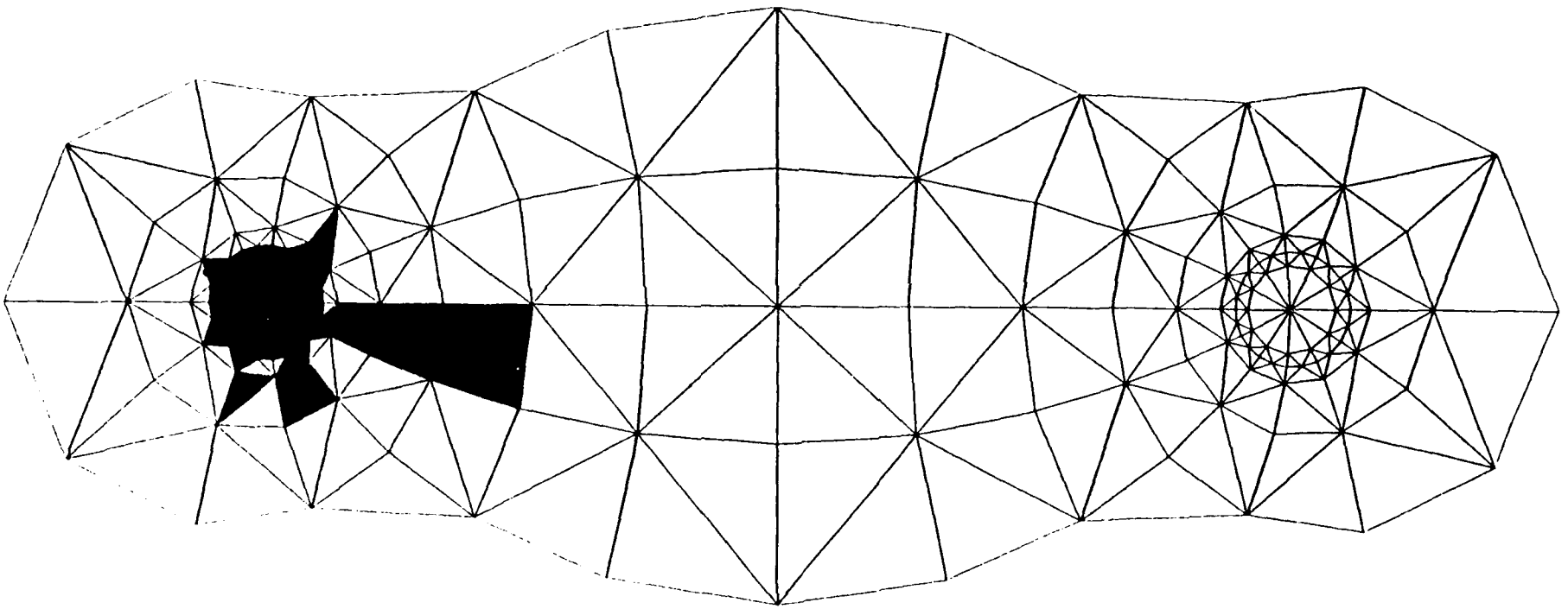

Darkened Regions Indicate

$$\frac{\gamma_{oct}}{\gamma_{lim}} > \frac{\gamma_{oct}}{\gamma_{lim}}_{far\ field} \times 1.10$$

Debond on 20, Rotation=45.0°, Poisson Constraint, Single Particle

Figure 19.

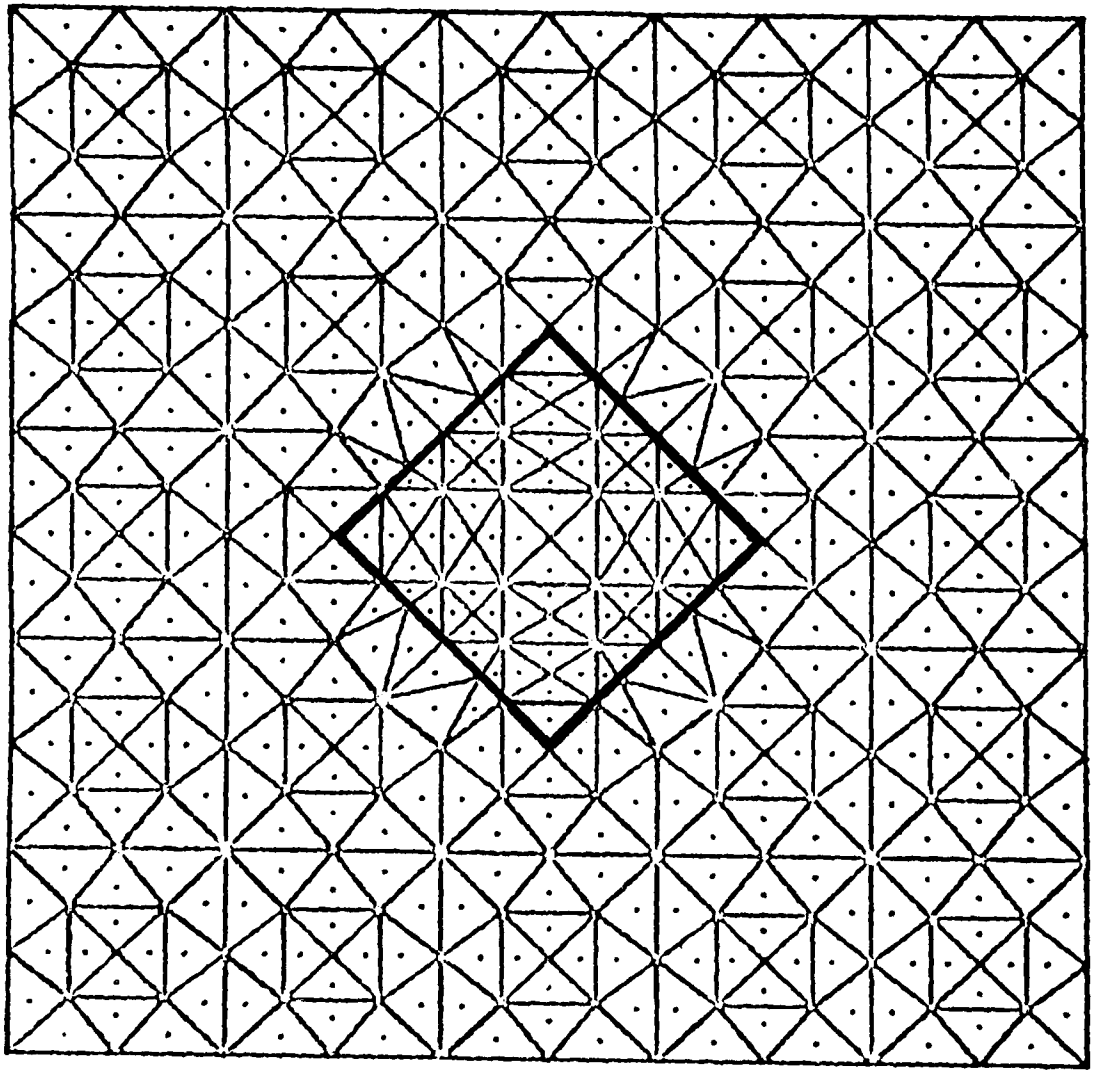

Matrix or Coarse Model. Substructuring occurs over region encompassed by heavy print.

Figure 20.

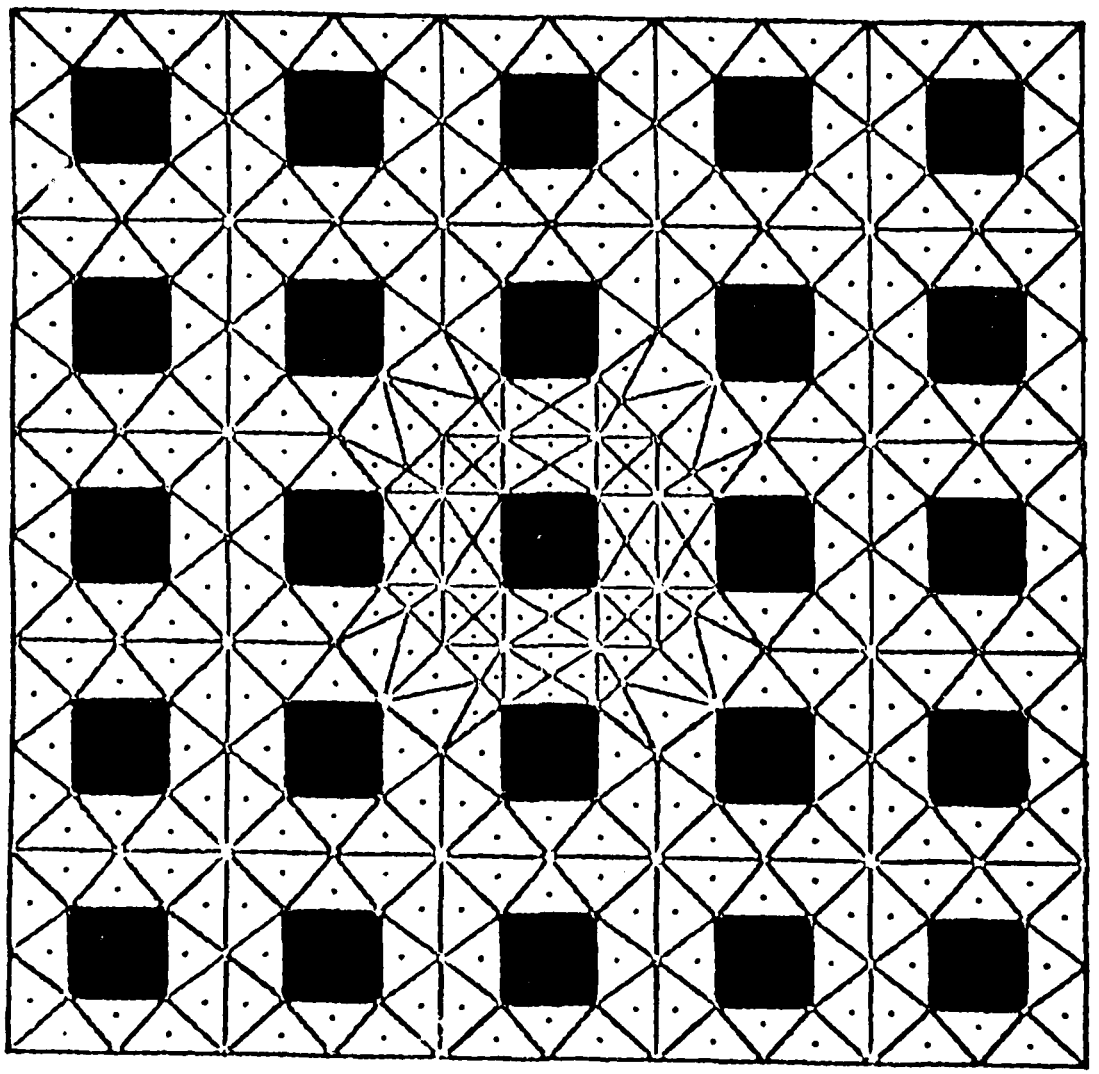

Matrix Model indicating L/D=2.

Figure 21.

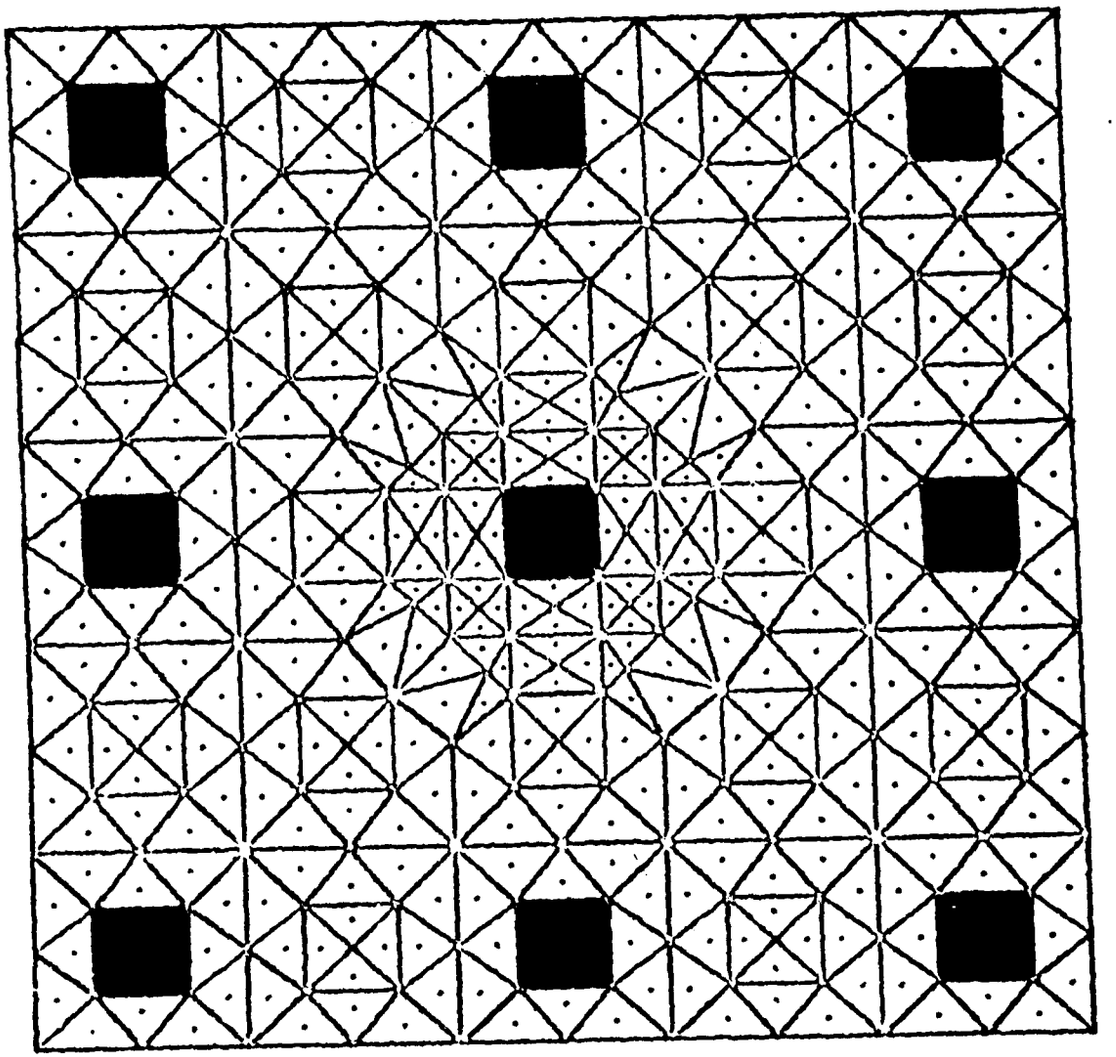

Matrix Model indicating L/D=4.

Figure 22.

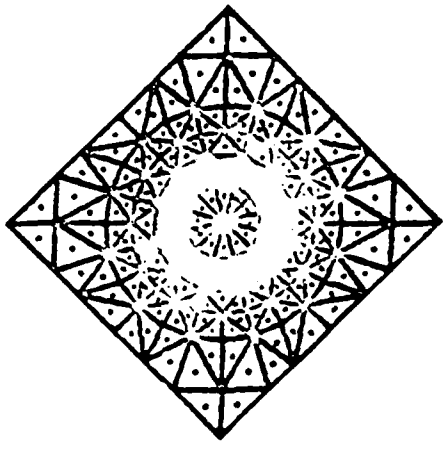

Particle or fine model presented in actual size and configuration.

Figure 23.

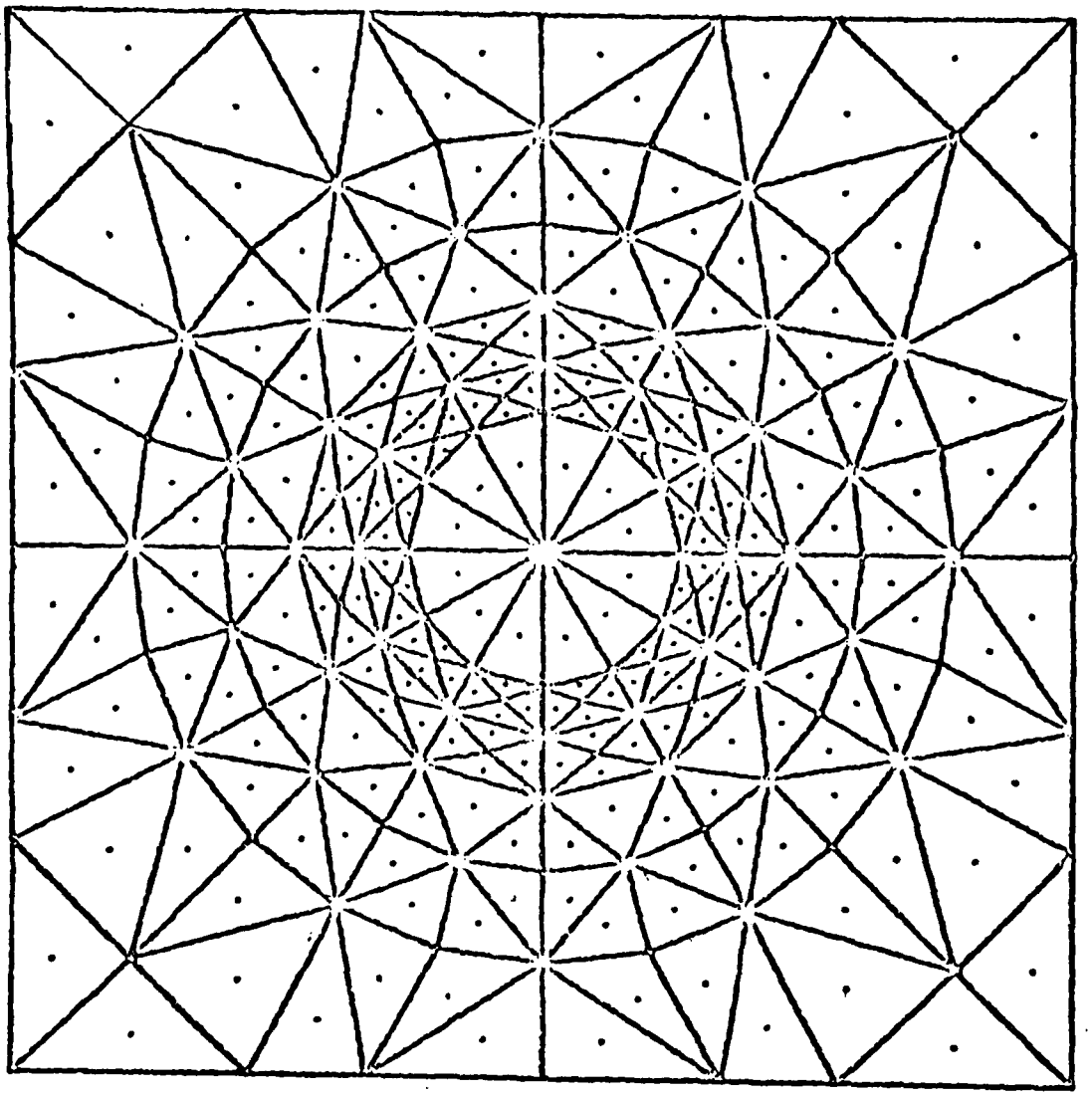

Enlargement of Particle Model and regions directly contguous.

Figure 24.

KEY:

⊙ PARTICLE-PARTICLE AXIS COINCIDES WITH TENSILE AXIS.

△ PARTICLE-PARTICLE AXIS FORMS 11.25° ANGLE WITH TENSILE AXIS.

⊡ PARTICLE-PARTICLE AXIS FORMS 22.5° ANGLE WITH TENSILE AXIS.

◇ PARTICLE-PARTICLE AXIS FORMS 45.0° ANGLE WITH TENSILE AXIS.

● ▲ ■ ◆ ANALOGOUS EXCEPT SINGLE PARTICLE ANALYSIS.

Figure 25a.

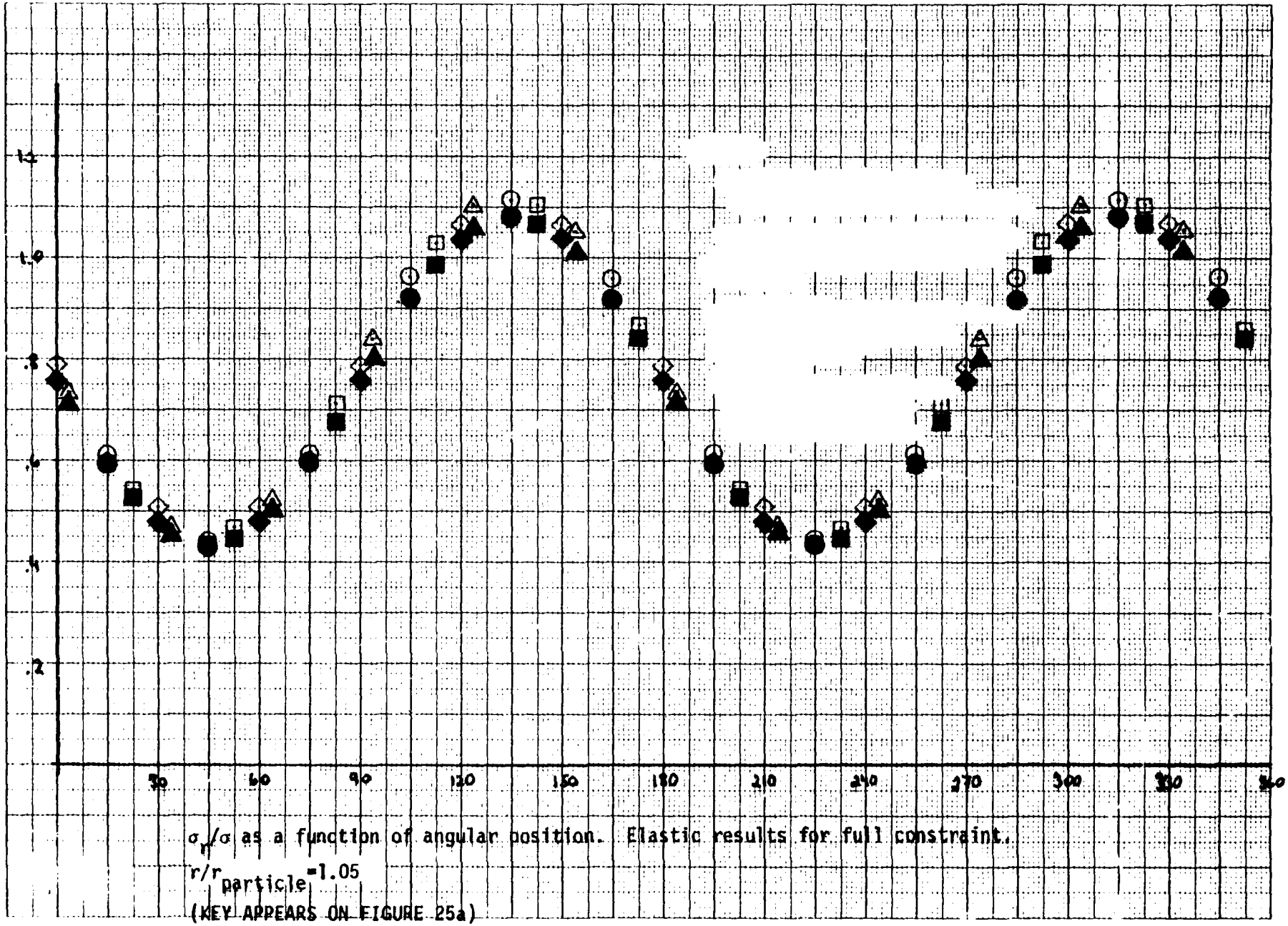

σ_θ/σ as a function of angular position. Elastic results for full constraint.

$r/r_{particle}$=1.05

(KEY APPEARS ON FIGURE 25a)

Figure 25b.

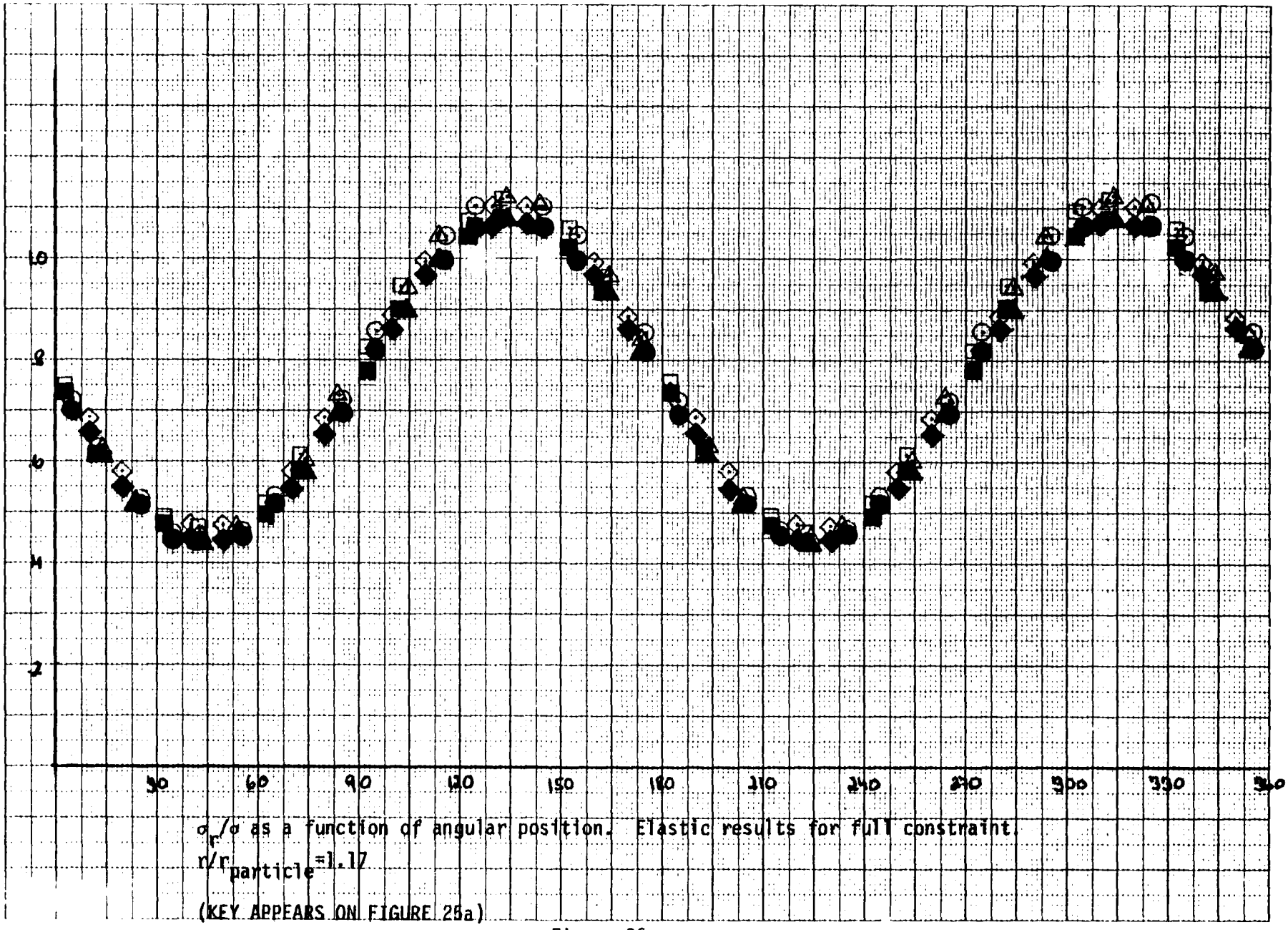

σ_r/σ as a function of angular position. Elastic results for full constraint.
$r/r_{particle}=1.17$

(KEY APPEARS ON FIGURE 25a)

Figure 26.

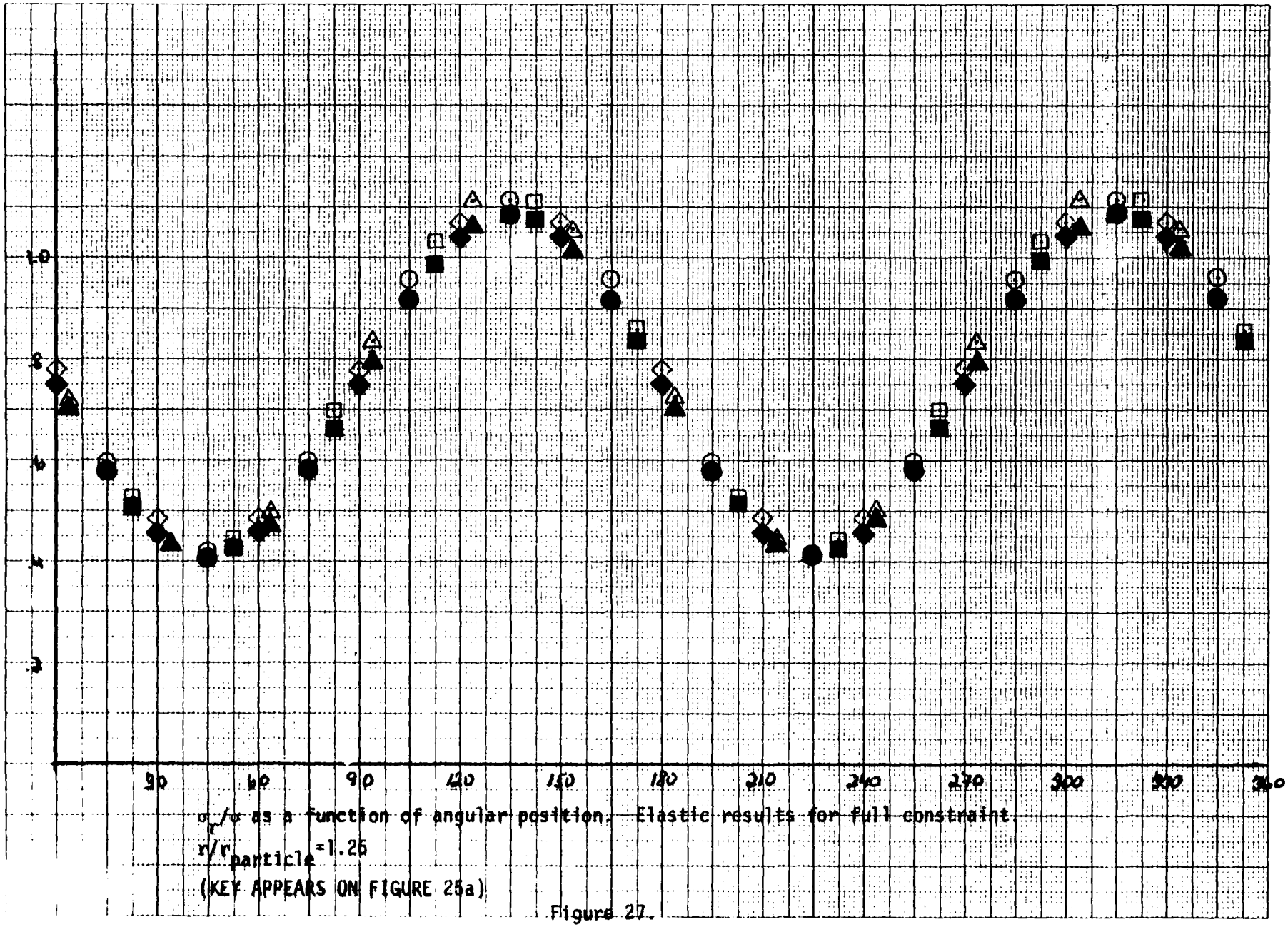

σ_r/σ as a function of angular position. Elastic results for full constraint.
$r/r_{particle}=1.25$
(KEY APPEARS ON FIGURE 25a)

Figure 27.

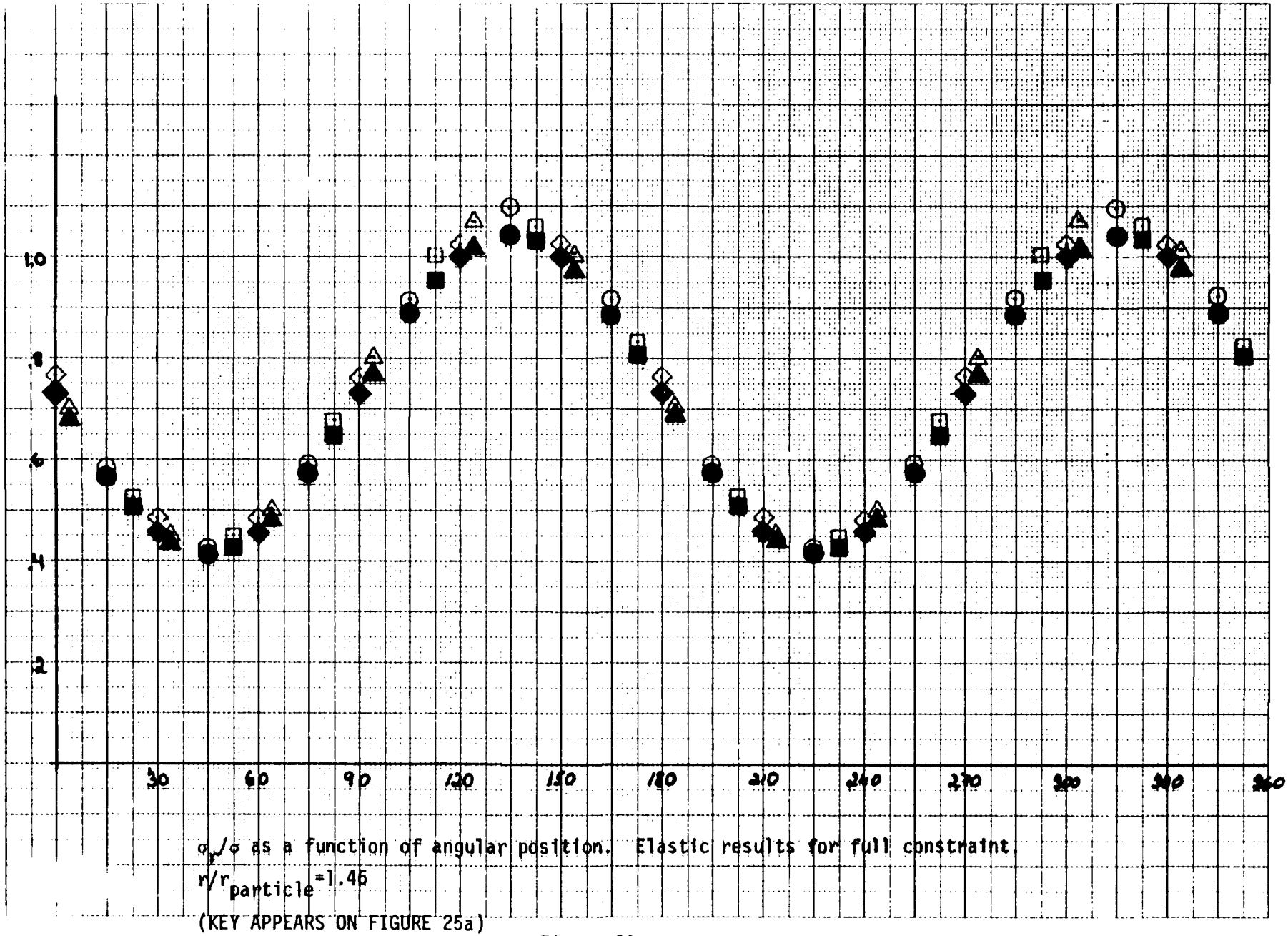

σ_r/σ as a function of angular position. Elastic results for full constraint.
$r/r_{particle}=1.46$
(KEY APPEARS ON FIGURE 25a)

Figure 28.

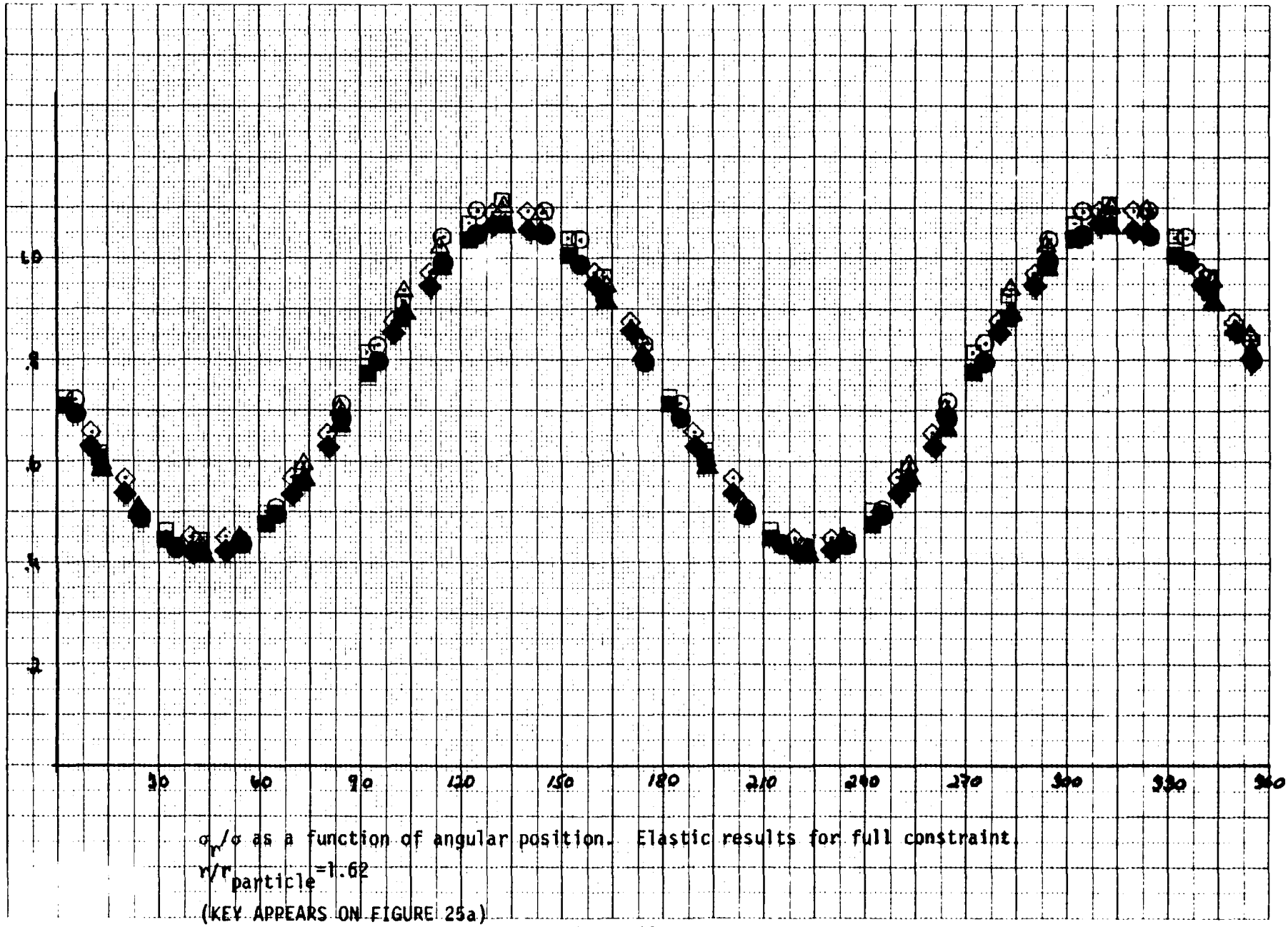

σ_r/σ as a function of angular position. Elastic results for full constraint.
$r/r_{particle}=1.62$
(KEY APPEARS ON FIGURE 25a)

Figure 29.

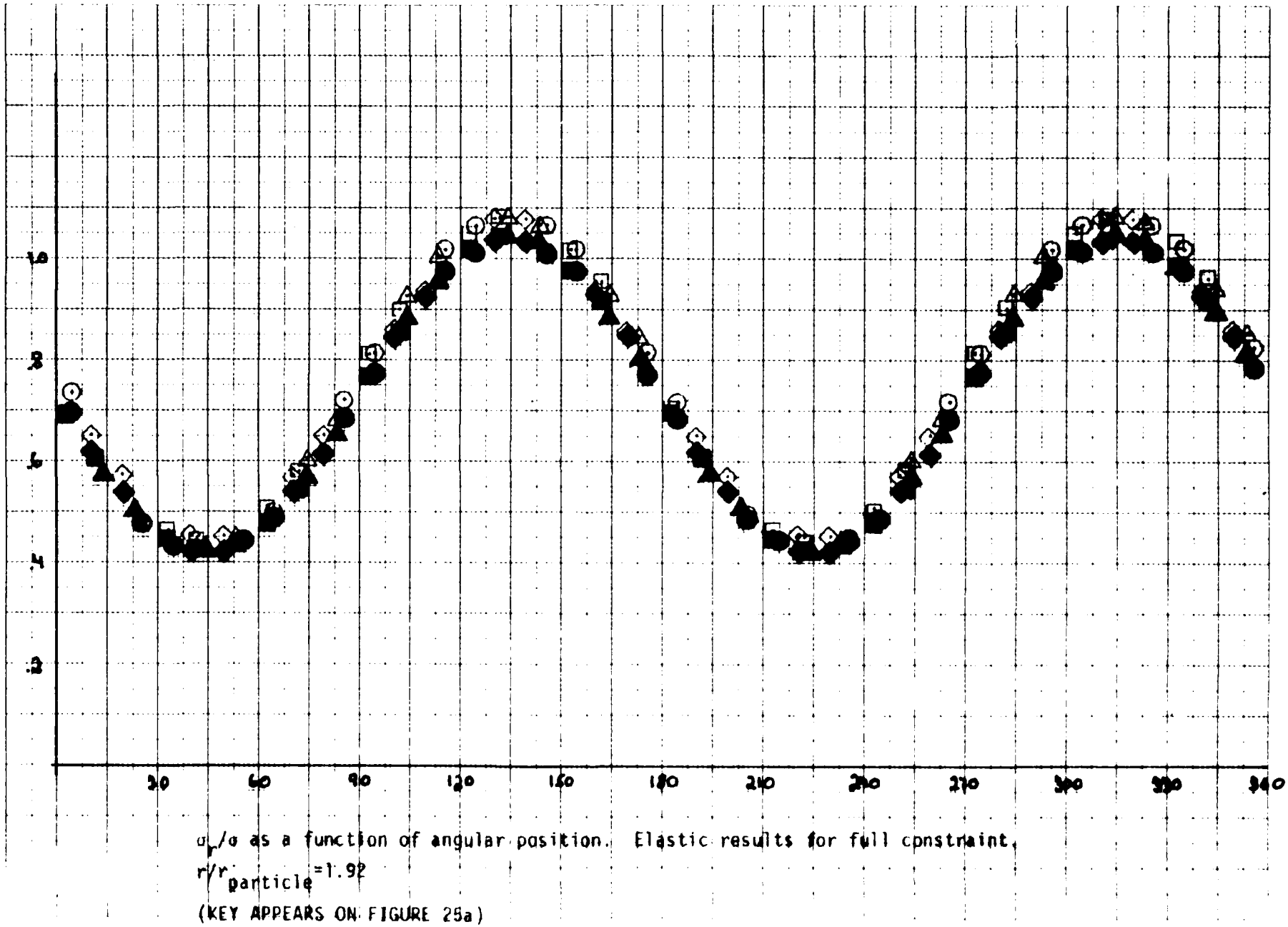

σ_r/σ as a function of angular position. Elastic results for full constraint, $r/r_{particle} = 1.92$

(KEY APPEARS ON FIGURE 25a)

Figure 30.

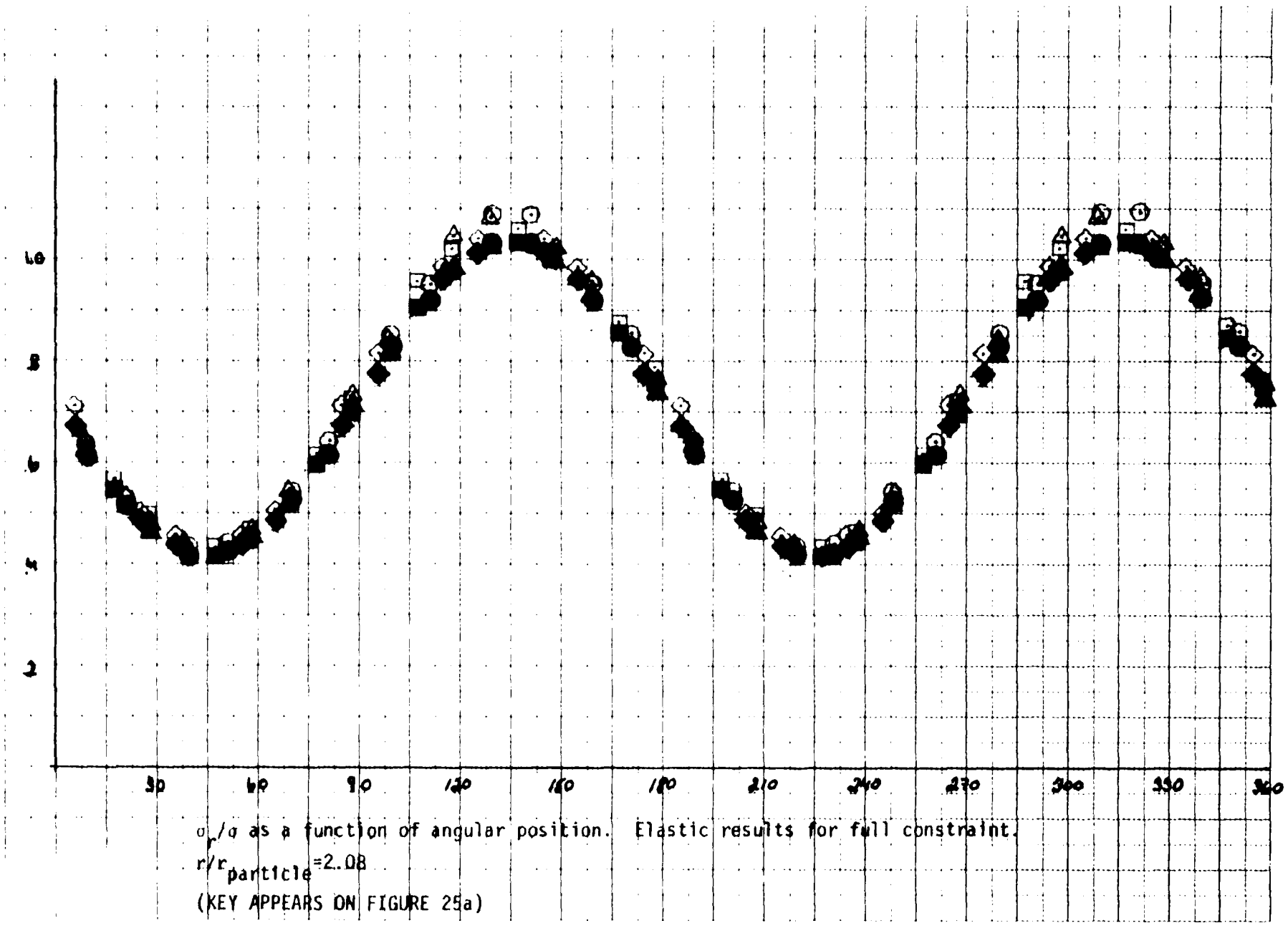

σ_r/σ as a function of angular position. Elastic results for full constraint.
$r/r_{particle}=2.08$
(KEY APPEARS ON FIGURE 25a)

Figure 31.

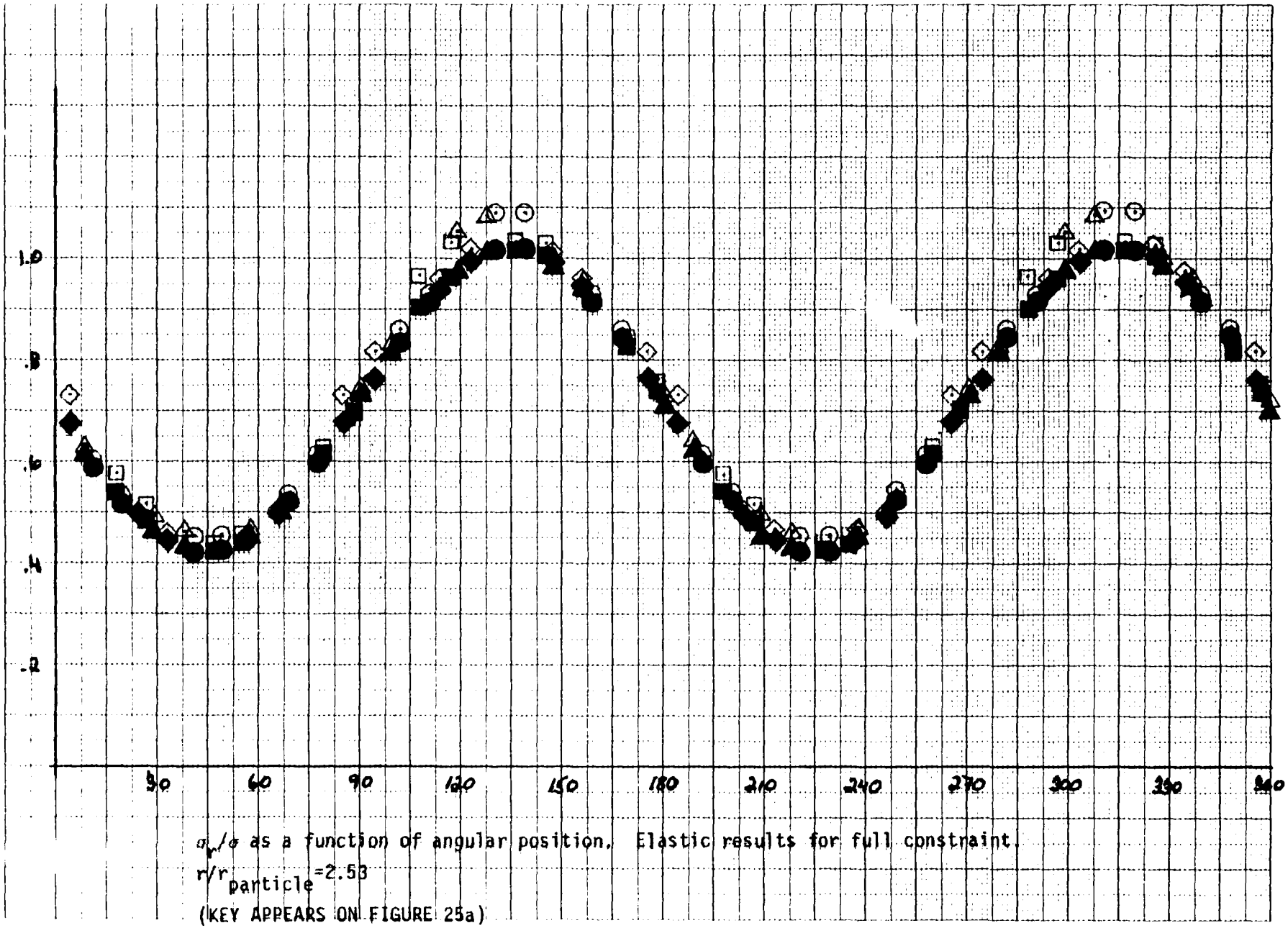

σ_r/σ as a function of angular position. Elastic results for full constraint.
$r/r_{particle}=2.53$
(KEY APPEARS ON FIGURE 25a)

Figure 32.

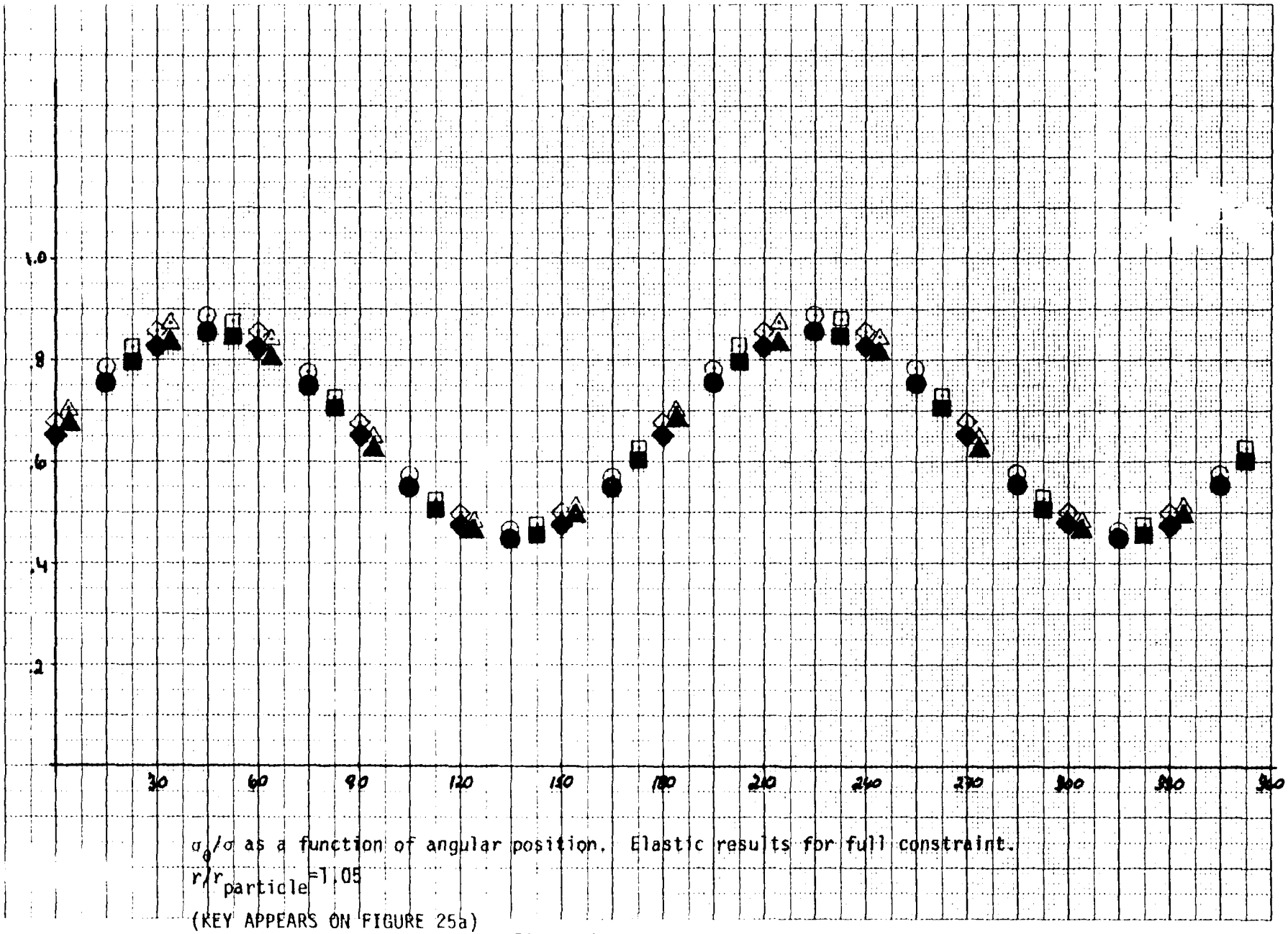

σ_θ/σ as a function of angular position. Elastic results for full constraint.
$r/r_{particle}=1.05$
(KEY APPEARS ON FIGURE 25a)

Figure 33.

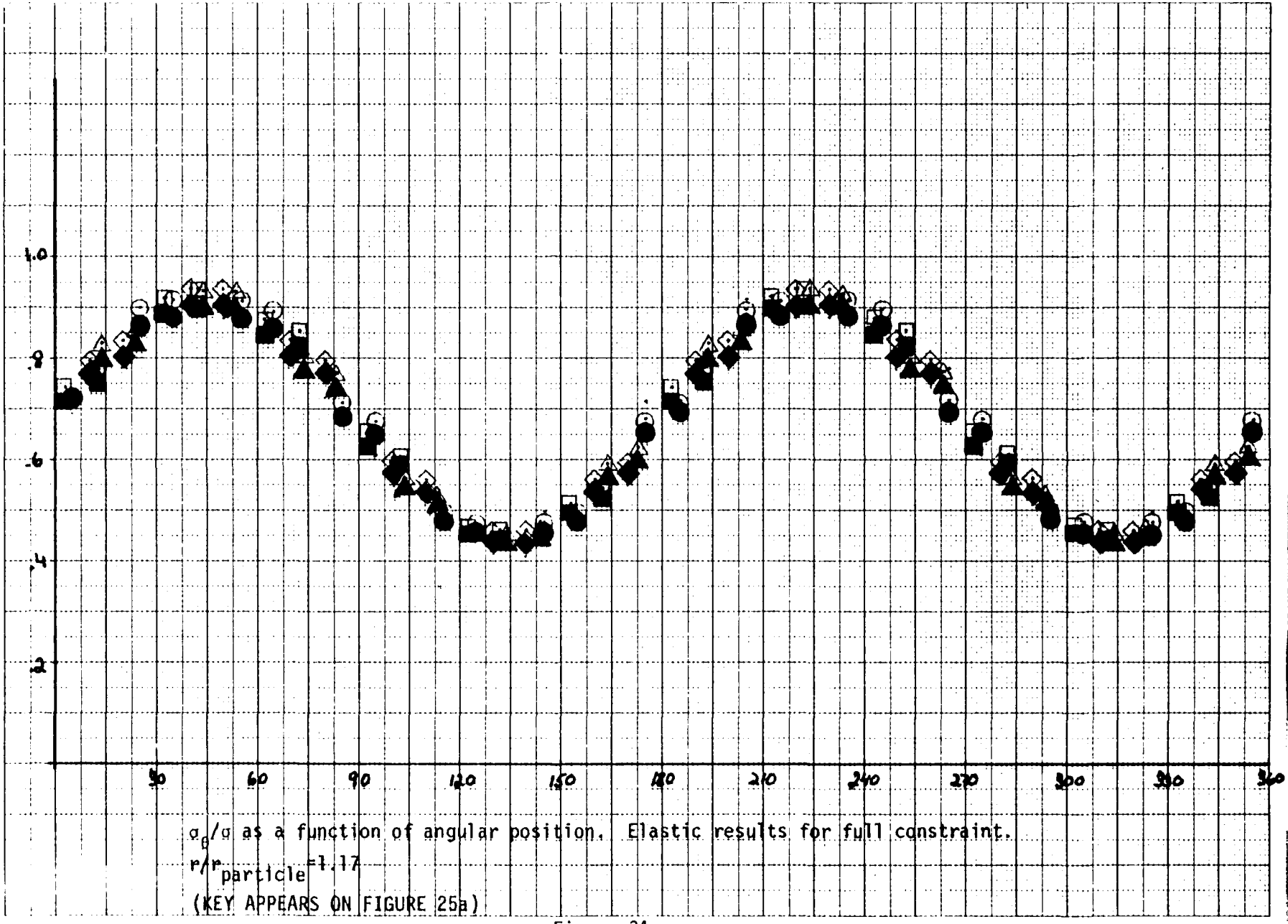

σ_θ/σ as a function of angular position. Elastic results for full constraint.
$r/r_{particle}=1.17$
(KEY APPEARS ON FIGURE 25a)

Figure 34.

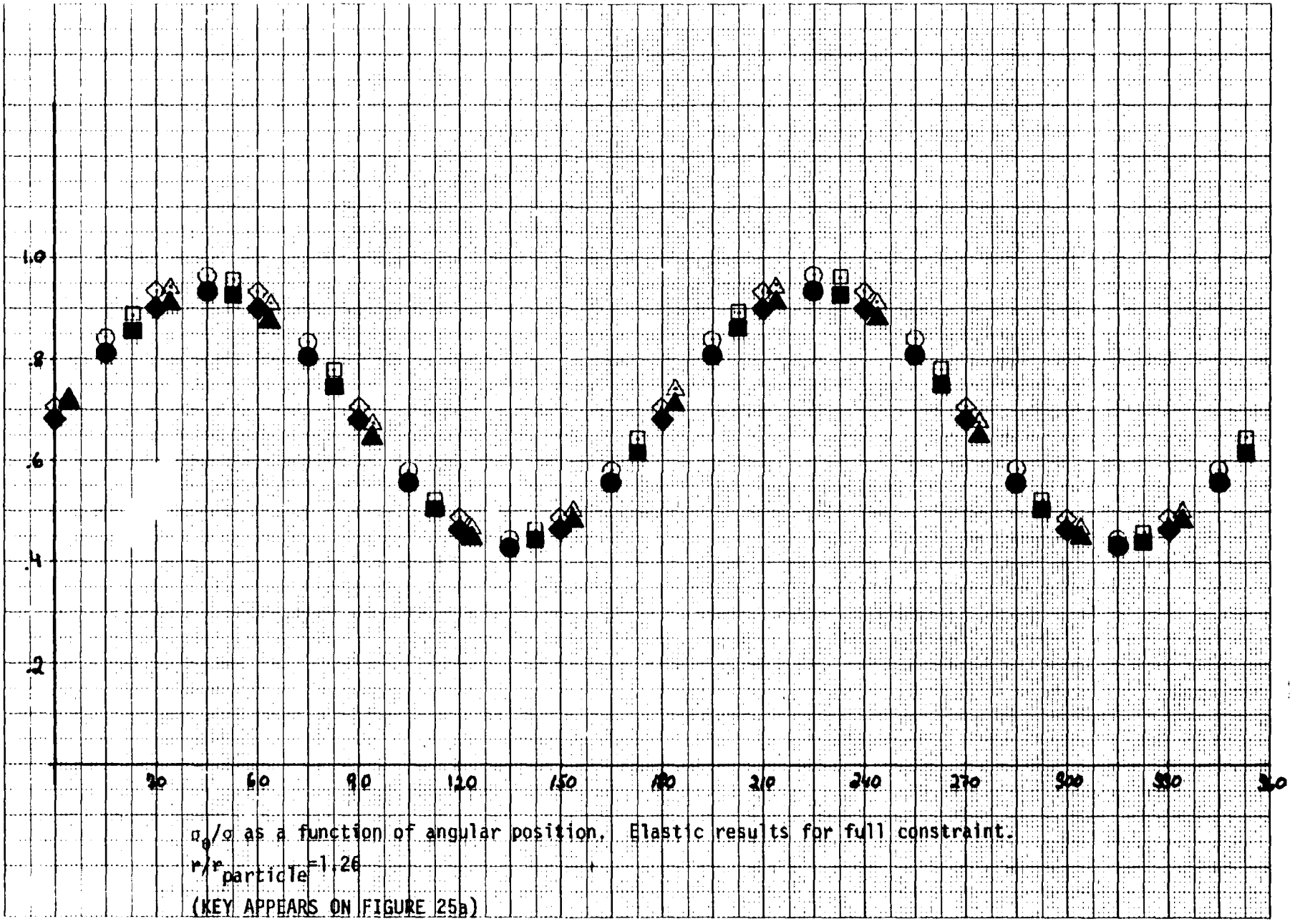

σ_θ/σ as a function of angular position. Elastic results for full constraint.

$r/r_{particle} = 1.26$

(KEY APPEARS ON FIGURE 25a)

Figure 35.

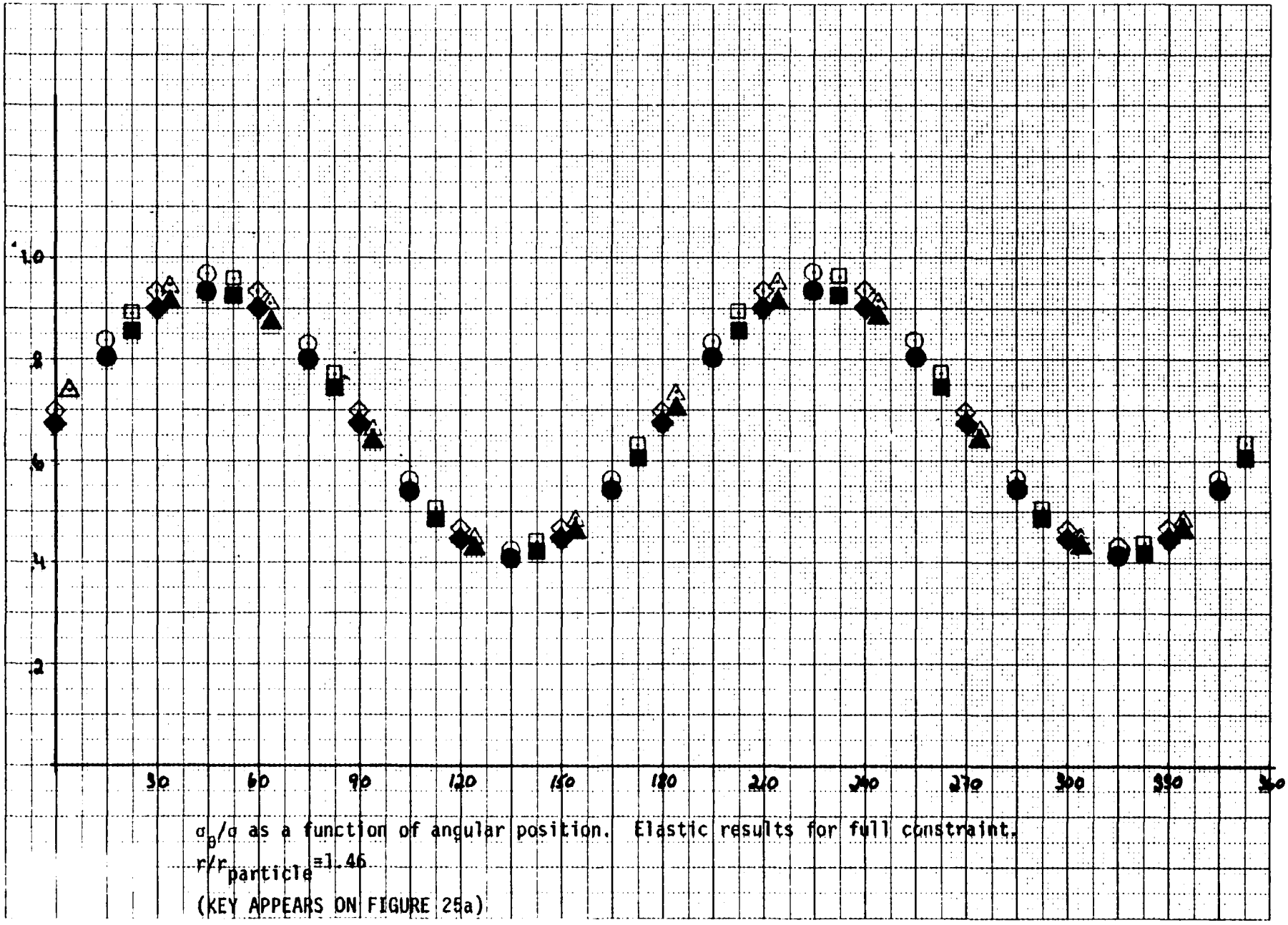

σ_θ/σ as a function of angular position. Elastic results for full constraint, $r/r_{particle}=1.46$

(KEY APPEARS ON FIGURE 25a)

Figure 36.

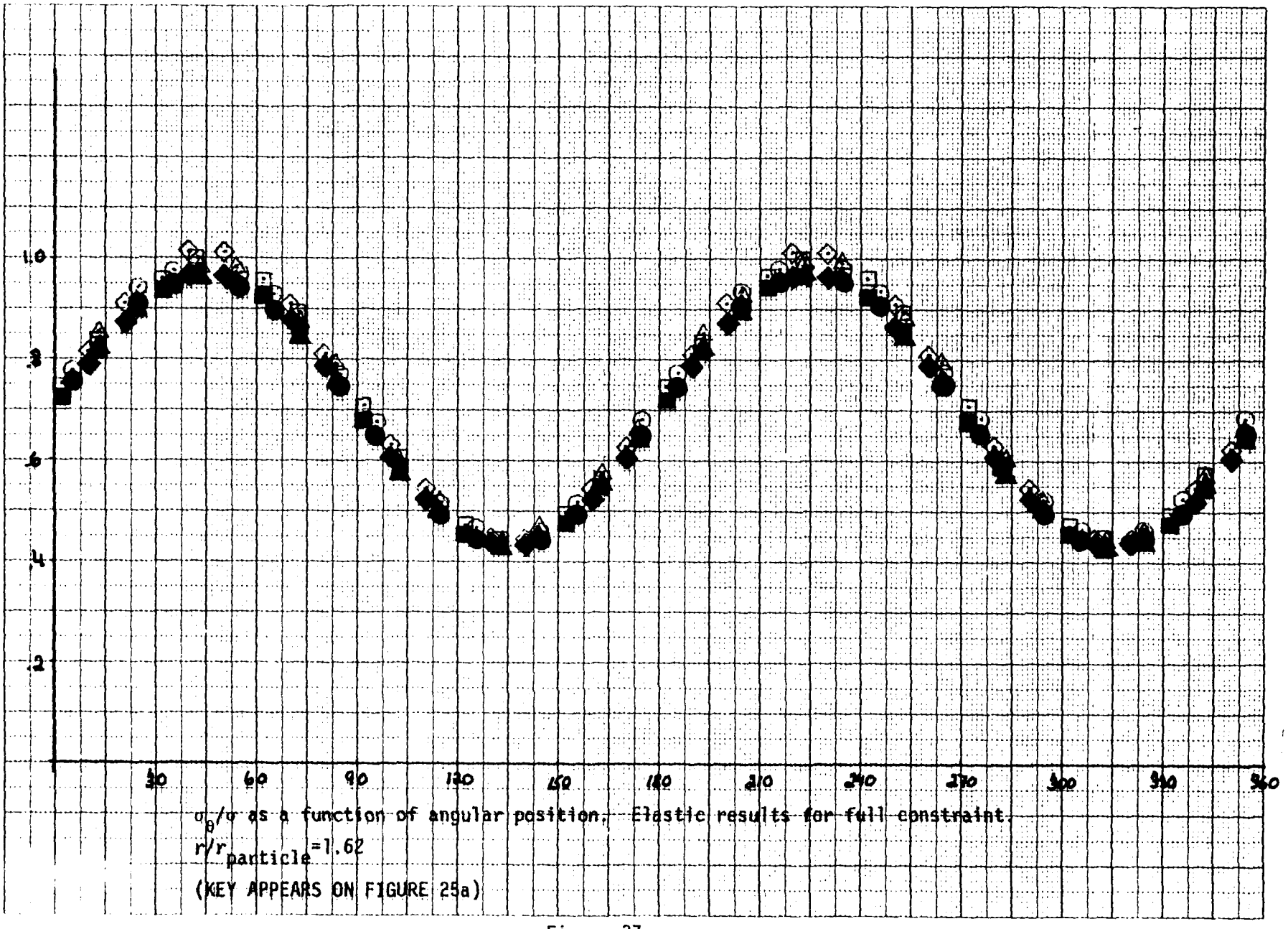

σ_θ/σ as a function of angular position. Elastic results for full constraint.
$r/r_{particle}=1.62$
(KEY APPEARS ON FIGURE 25a)

Figure 37.

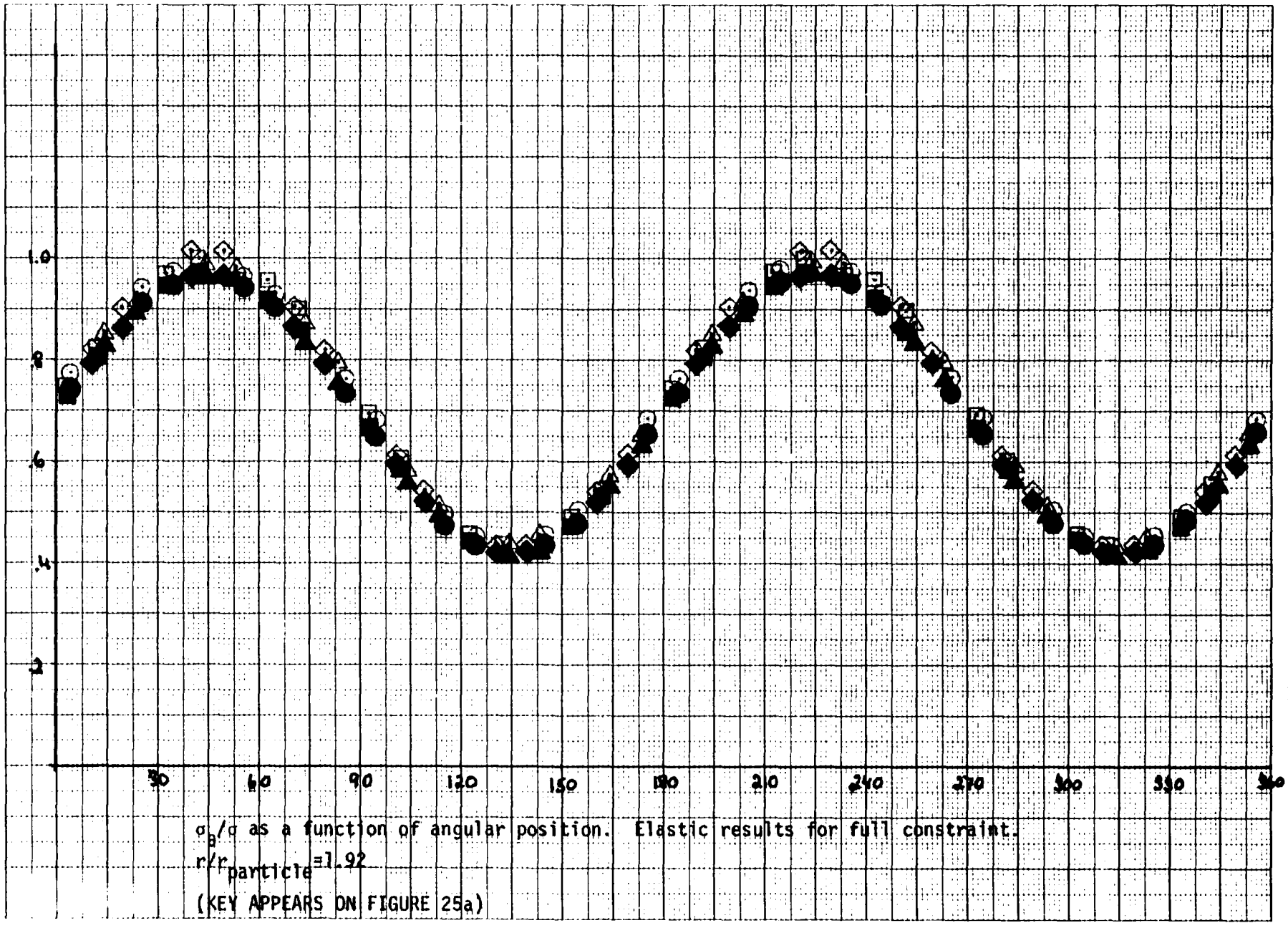

σ_θ/σ as a function of angular position. Elastic results for full constraint.
$r/r_{particle}=1.92$
(KEY APPEARS ON FIGURE 25a)

Figure 38.

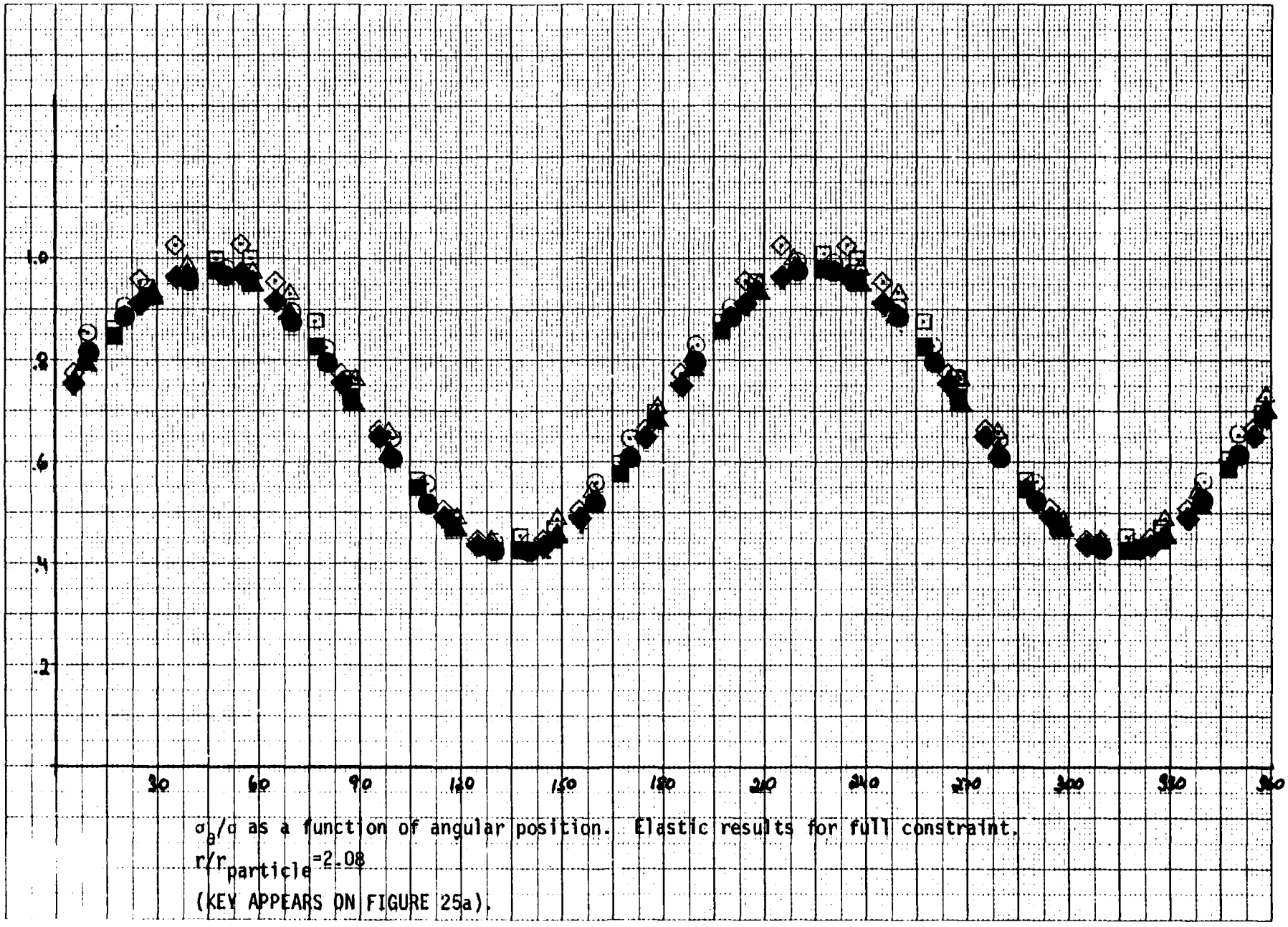

σ_θ/σ as a function of angular position. Elastic results for full constraint, $r/r_{particle}=2.08$ (KEY APPEARS ON FIGURE 25a).

Figure 39.

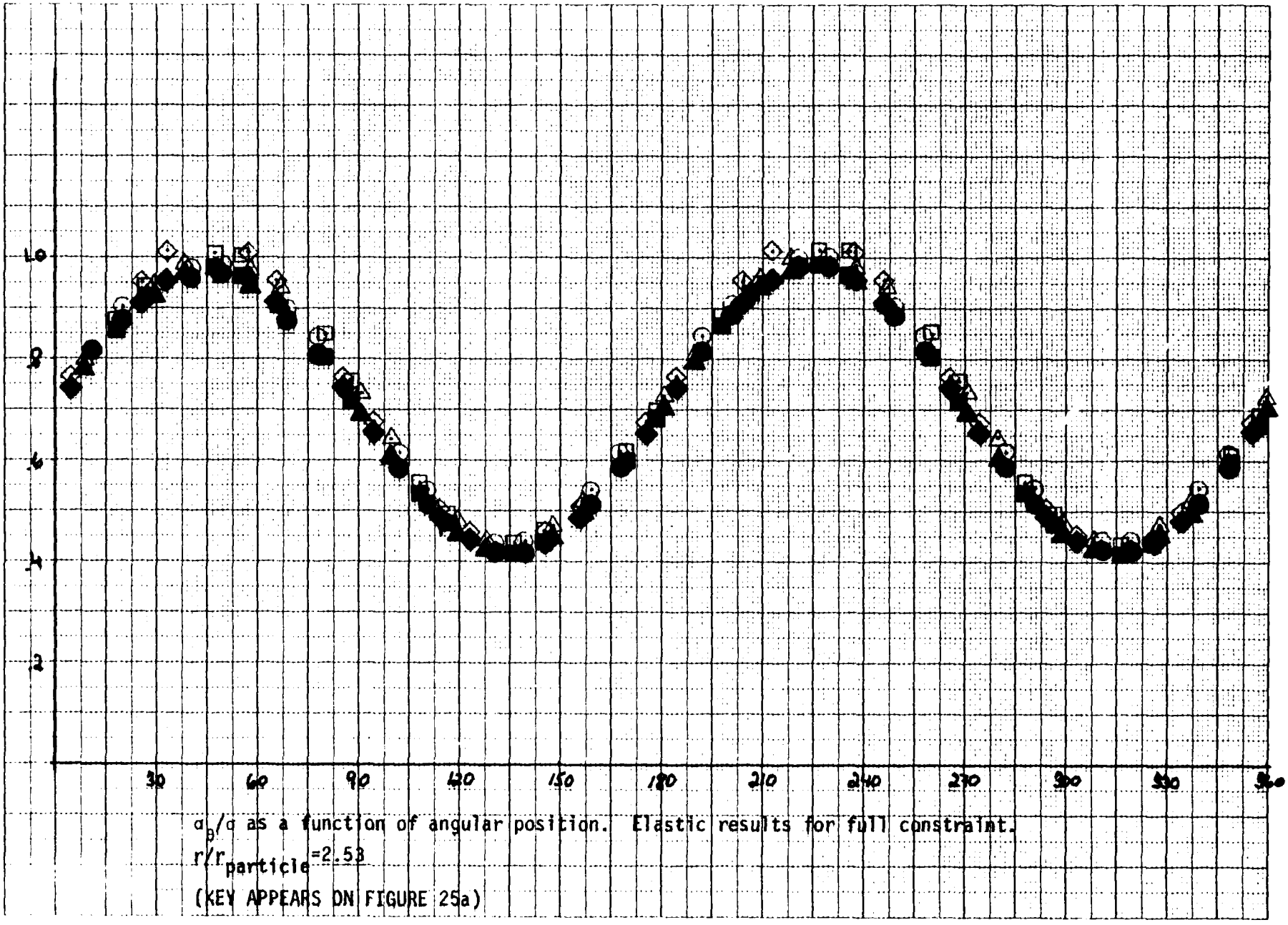

σ_θ/σ as a function of angular position. Elastic results for full constraint.
$r/r_{particle}=2.53$
(KEY APPEARS ON FIGURE 25a)

Figure 40.

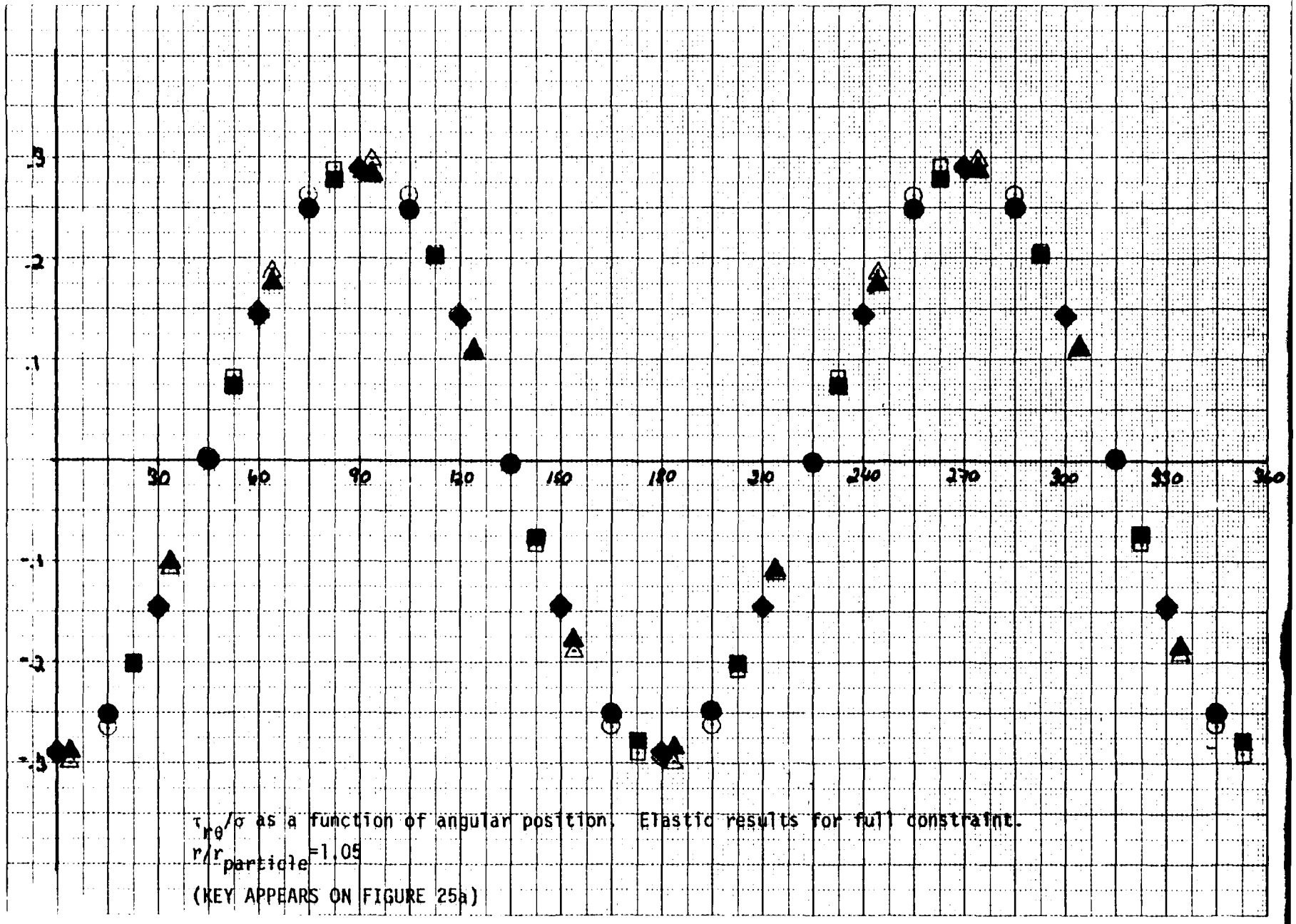

$\tau_{r\theta}/\sigma$ as a function of angular position. Elastic results for full constraint.
$r/r_{particle}=1.05$
(KEY APPEARS ON FIGURE 25a)

Figure 41.

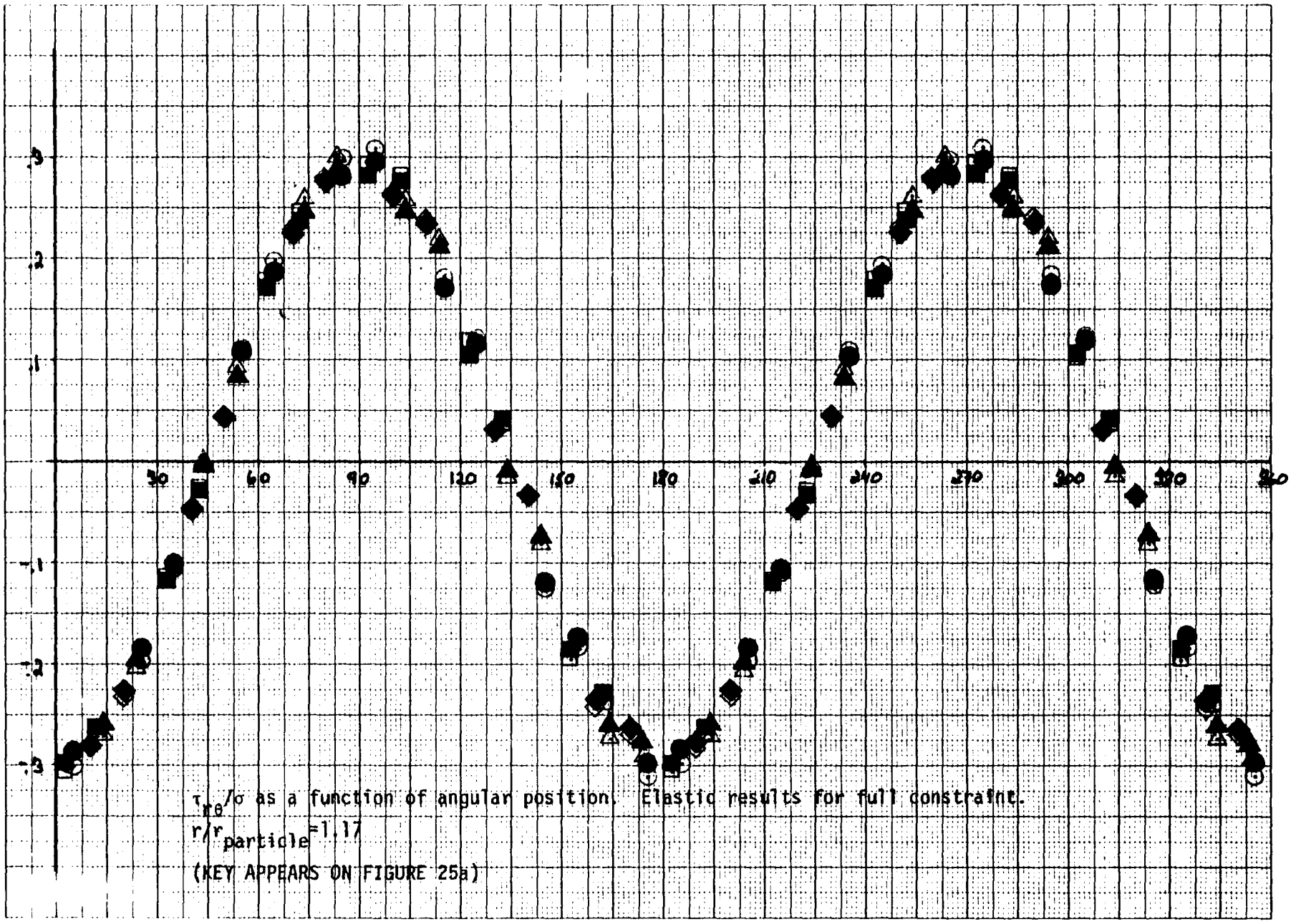

$\tau_{r\theta}/\sigma$ as a function of angular position. Elastic results for full constraint.
$r/r_{particle}=1.17$
(KEY APPEARS ON FIGURE 25a)

Figure 42.

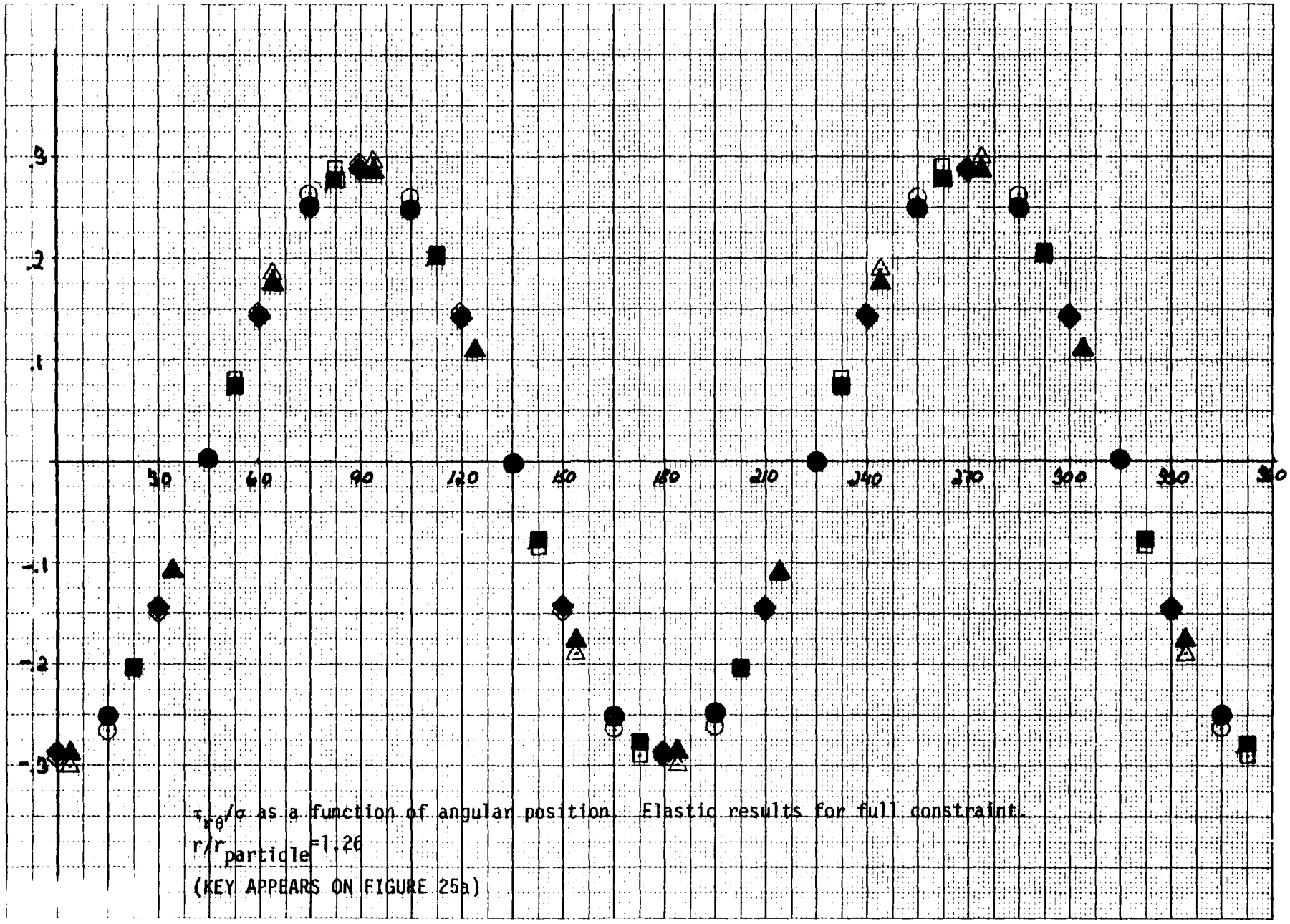

$\tau_{r\theta}/\sigma$ as a function of angular position. Elastic results for full constraint.
$r/r_{particle}=1.26$
(KEY APPEARS ON FIGURE 25a)

Figure 43.

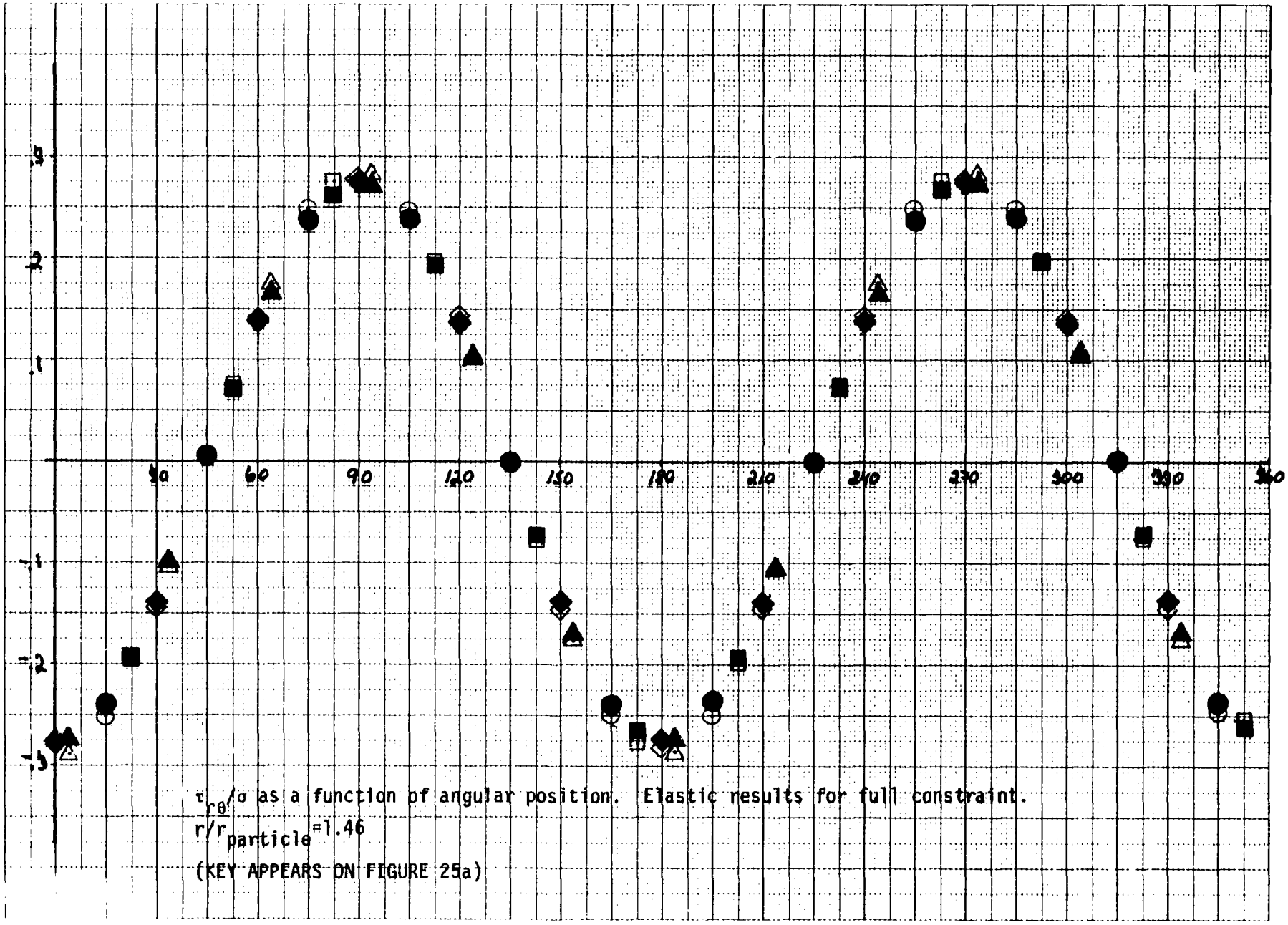

$\tau_{r\theta}/\sigma$ as a function of angular position. Elastic results for full constraint.
$r/r_{particle}=1.46$
(KEY APPEARS ON FIGURE 25a)

Figure 44.

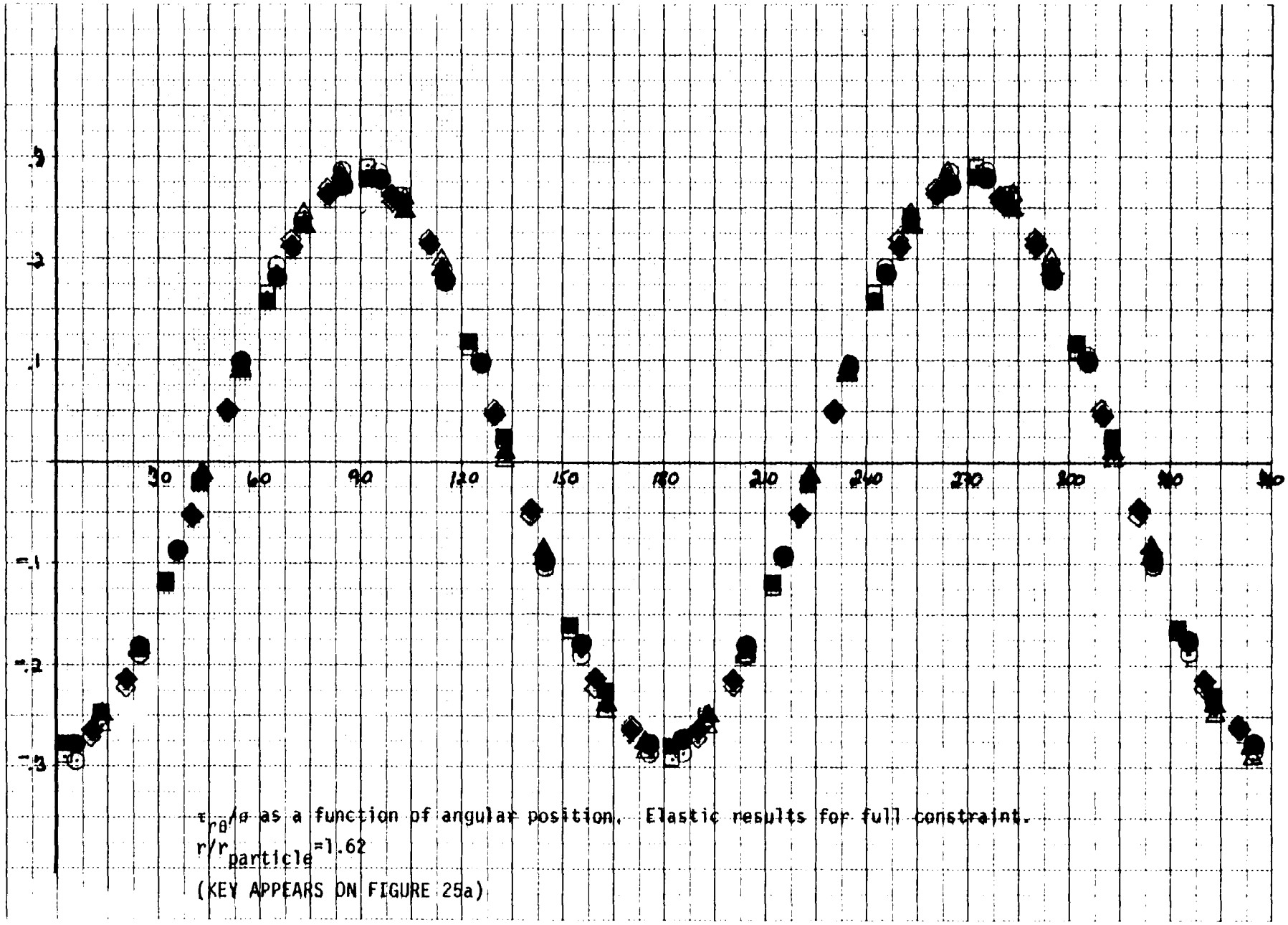

$\tau_{r\theta}/\sigma$ as a function of angular position. Elastic results for full constraint.
$r/r_{particle}=1.62$
(KEY APPEARS ON FIGURE 25a)

Figure 45.

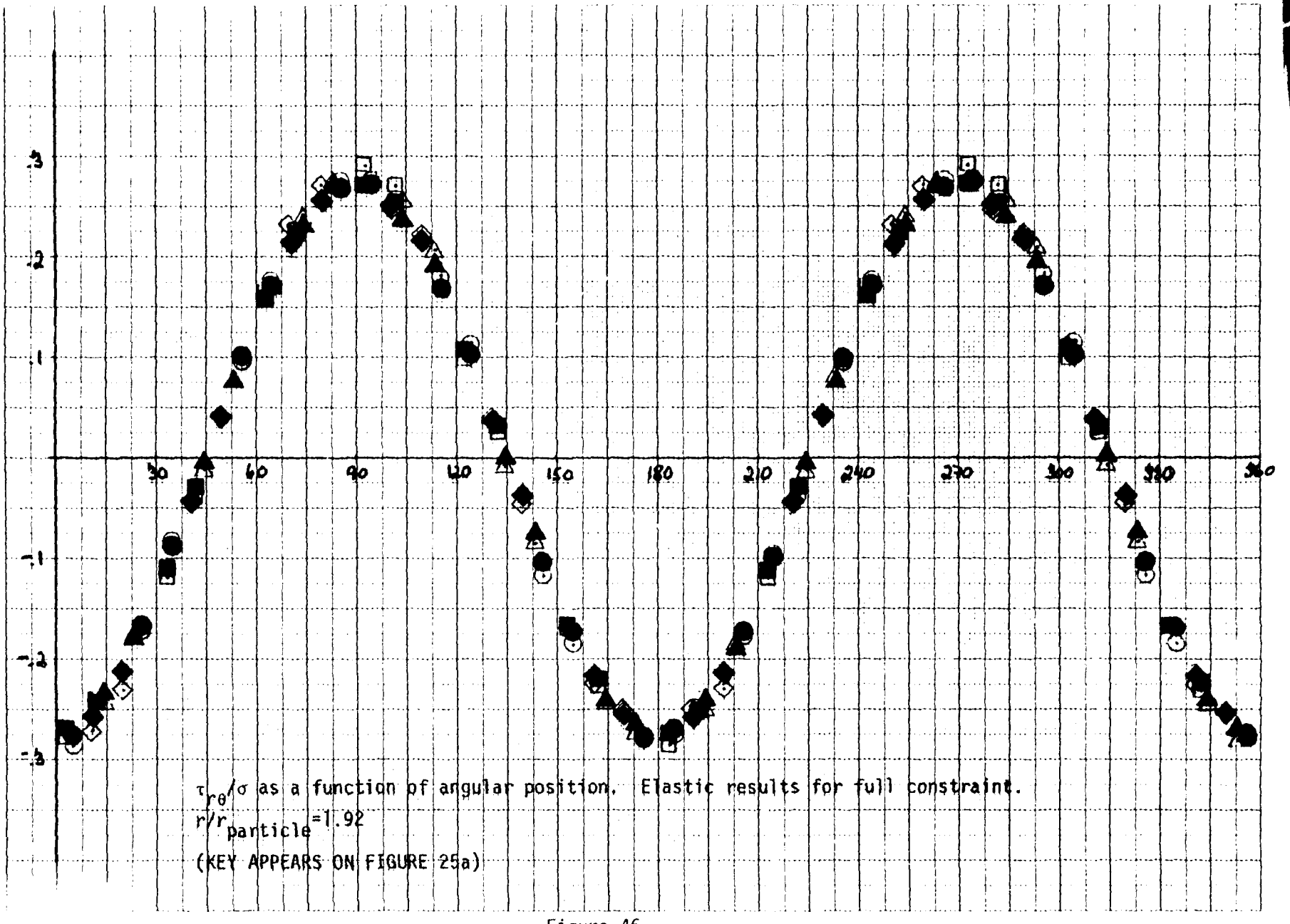

$\tau_{r\theta}/\sigma$ as a function of angular position. Elastic results for full constraint.
$r/r_{particle}=1.92$
(KEY APPEARS ON FIGURE 25a)

Figure 46.

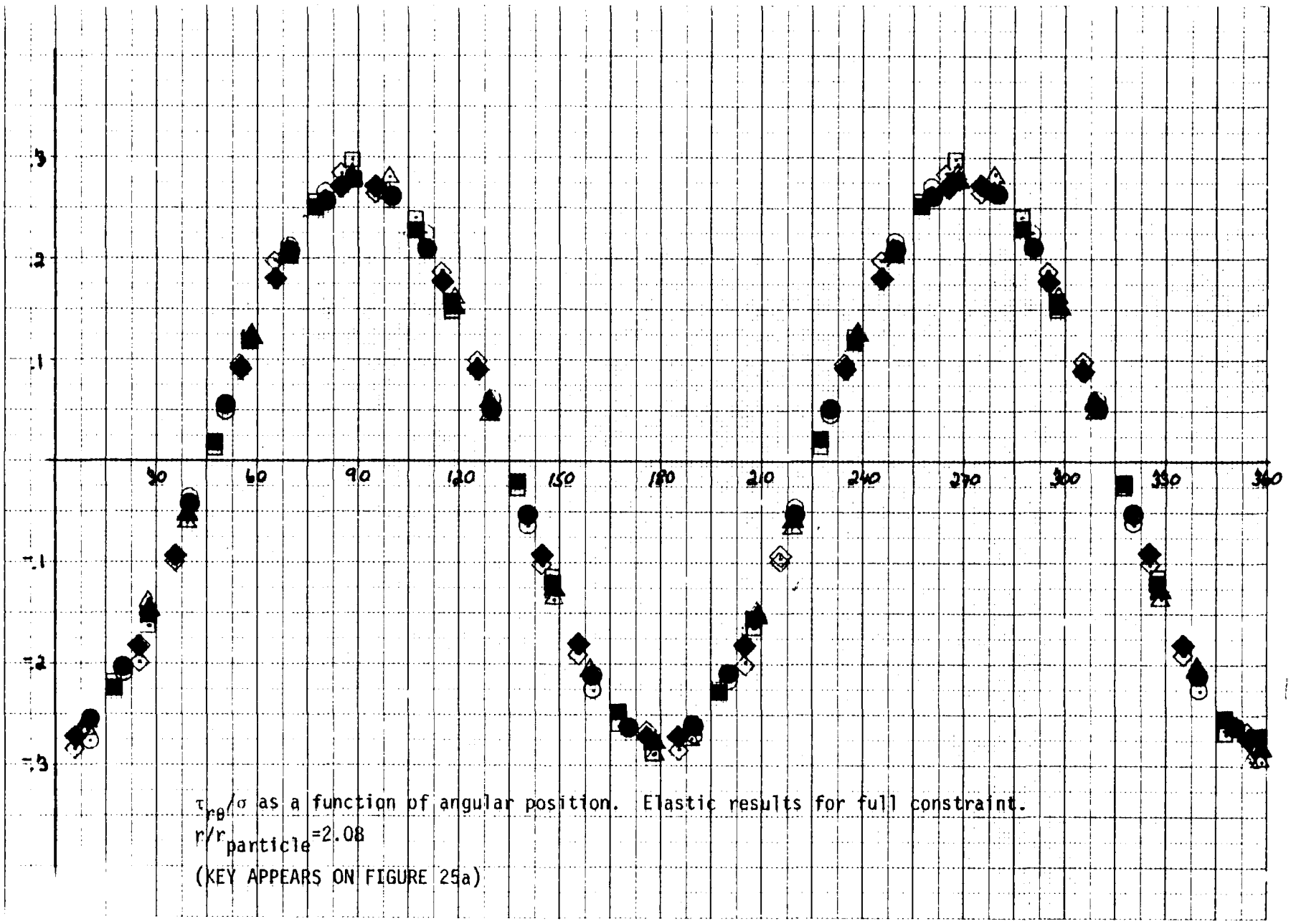

$\tau_{r\theta}/\sigma$ as a function of angular position. Elastic results for full constraint.
$r/r_{particle}=2.08$
(KEY APPEARS ON FIGURE 25a)

Figure 47.

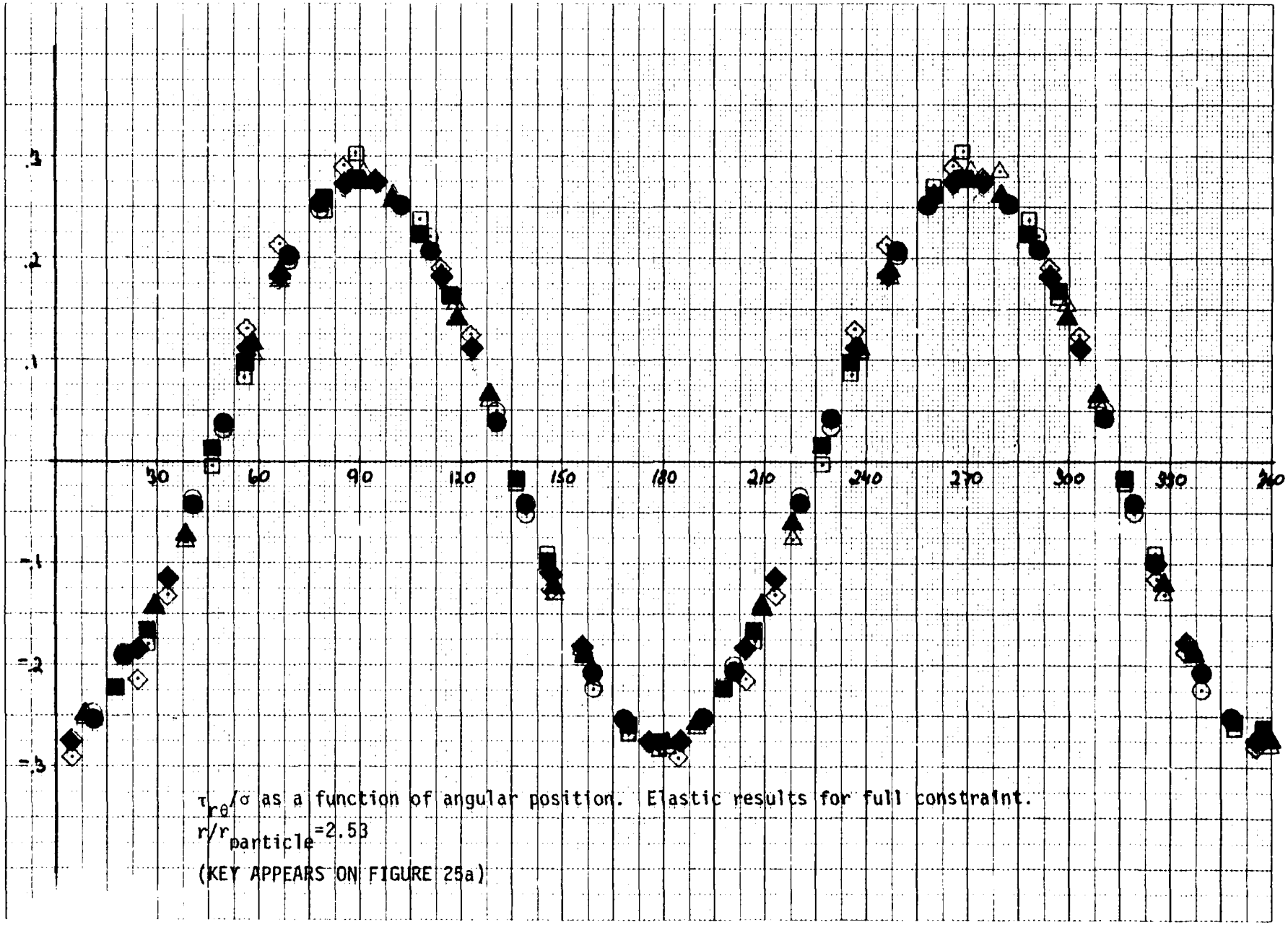

$\tau_{r\theta}/\sigma$ as a function of angular position. Elastic results for full constraint.
$r/r_{particle}=2.53$
(KEY APPEARS ON FIGURE 25a)

Figure 48.

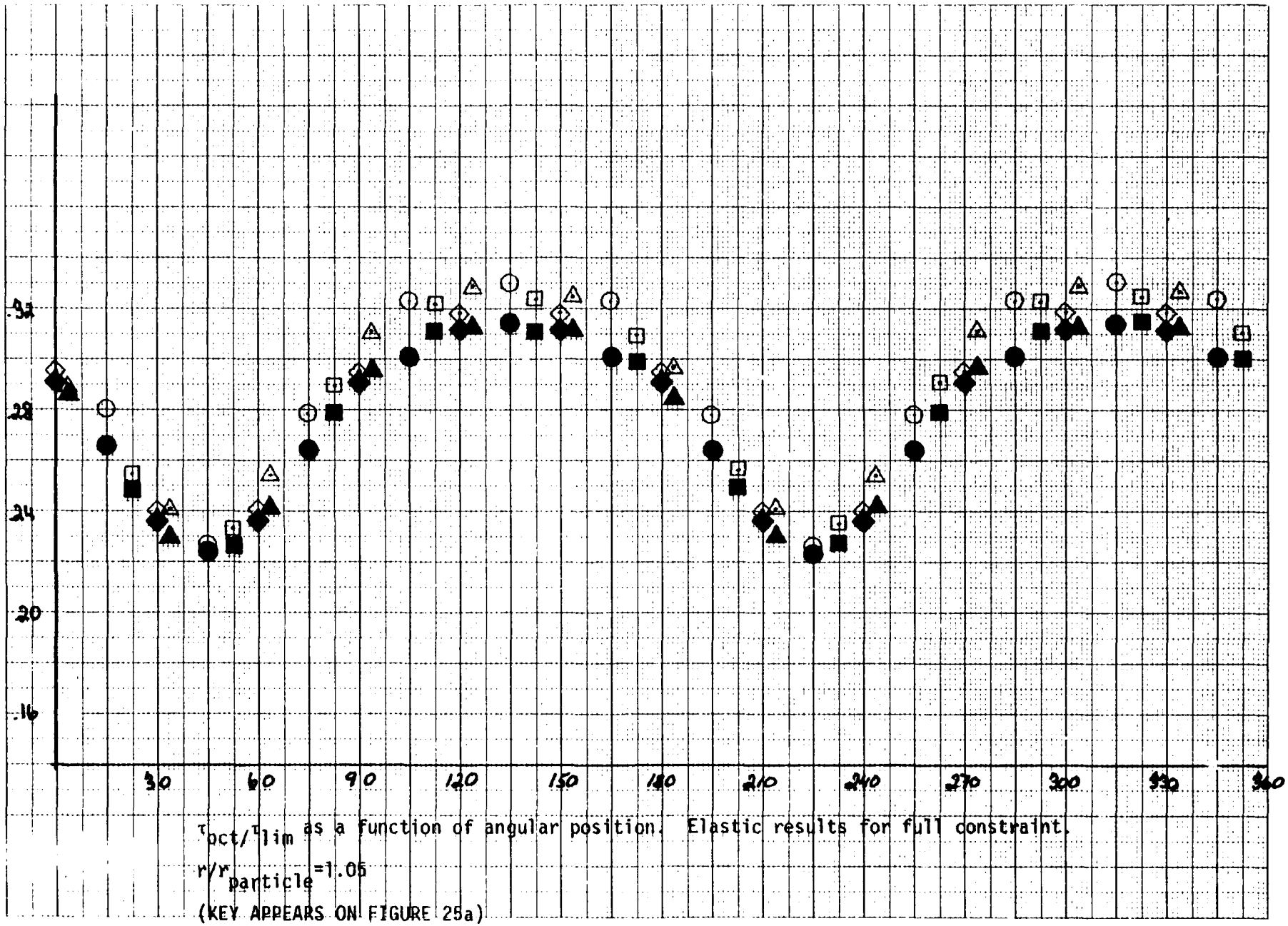

τ_{oct}/τ_{lim} as a function of angular position. Elastic results for full constraint.

$r/r_{particle}=1.05$

(KEY APPEARS ON FIGURE 25a)

Figure 49.

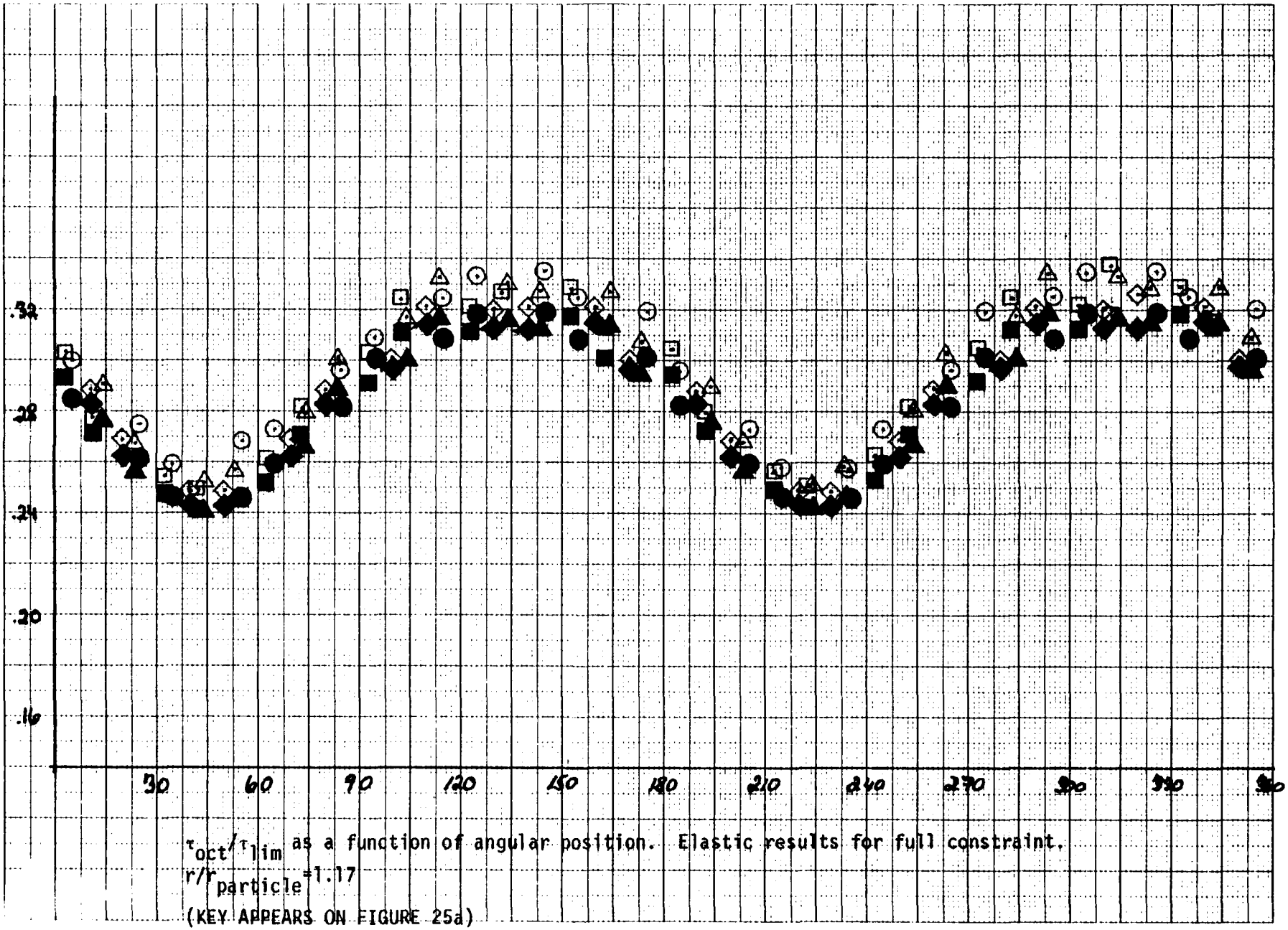

τ_{oct}/τ_{lim} as a function of angular position. Elastic results for full constraint.
$r/r_{particle}=1.17$
(KEY APPEARS ON FIGURE 25a)

Figure 50.

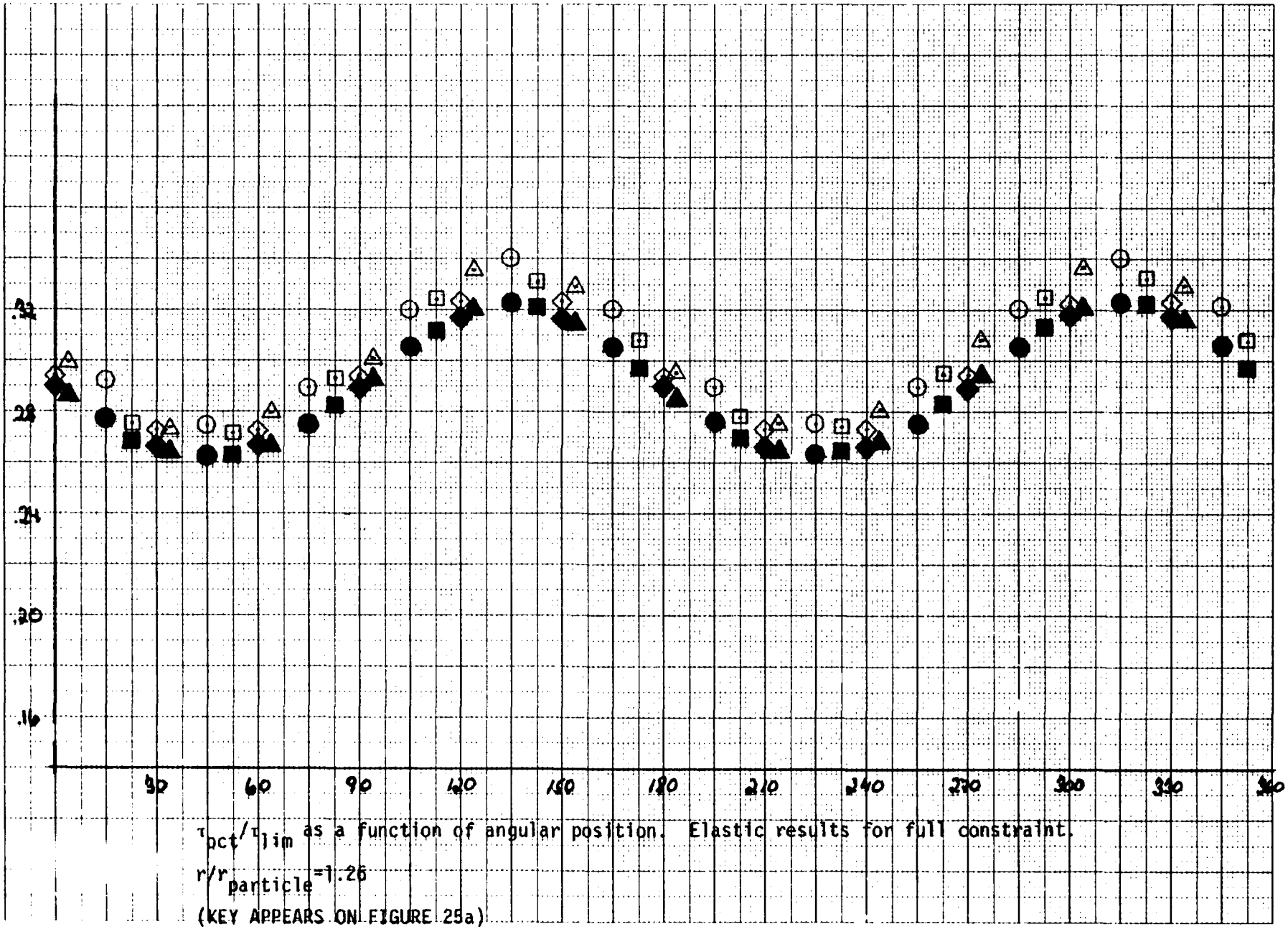

τ_{oct}/τ_{lim} as a function of angular position. Elastic results for full constraint.

$r/r_{particle}=1.26$

(KEY APPEARS ON FIGURE 25a)

Figure 51.

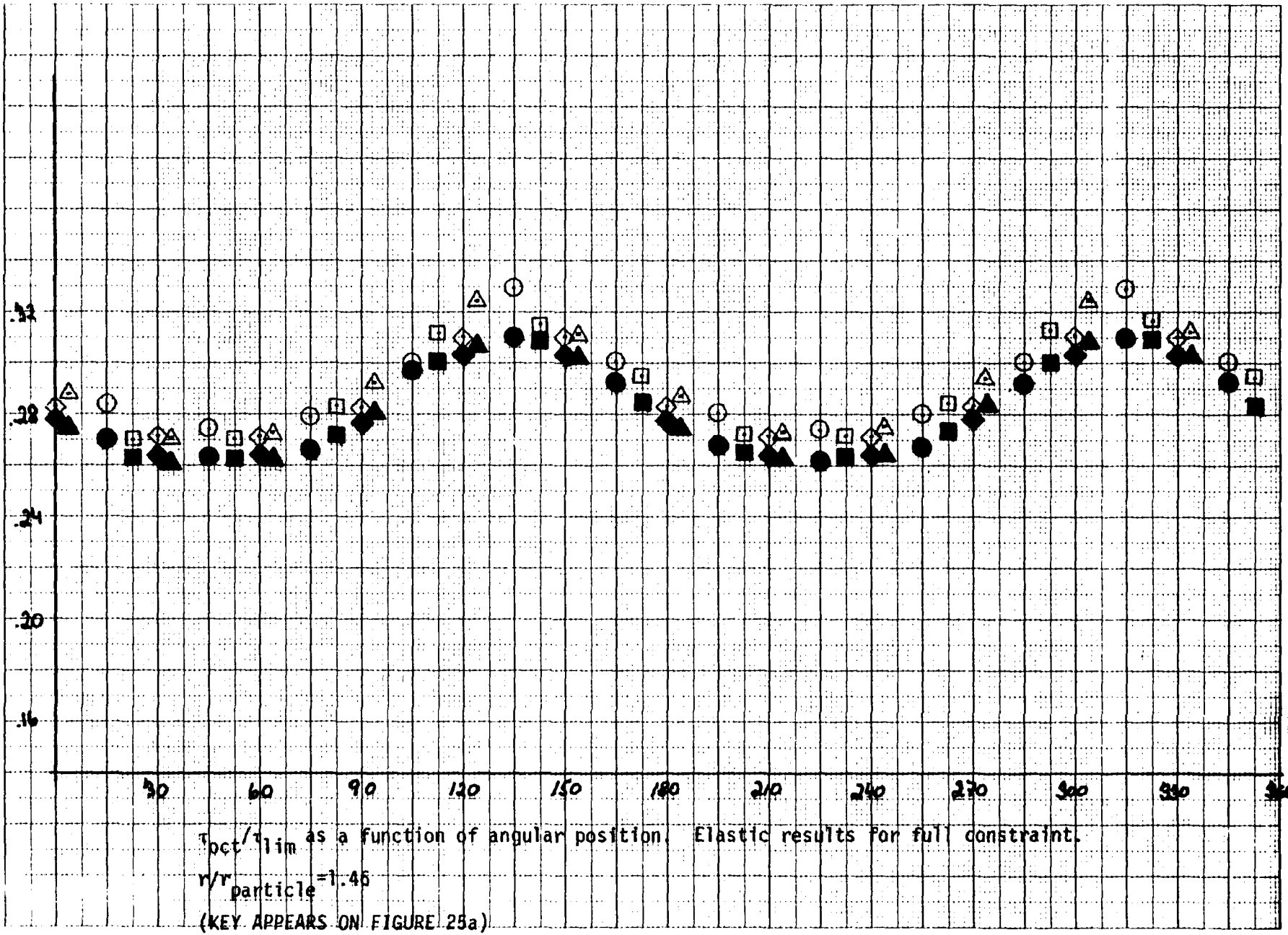

τ_{oct}/τ_{lim} as a function of angular position. Elastic results for full constraint.

$r/r_{particle}=1.46$

(KEY APPEARS ON FIGURE 25a)

Figure 52.

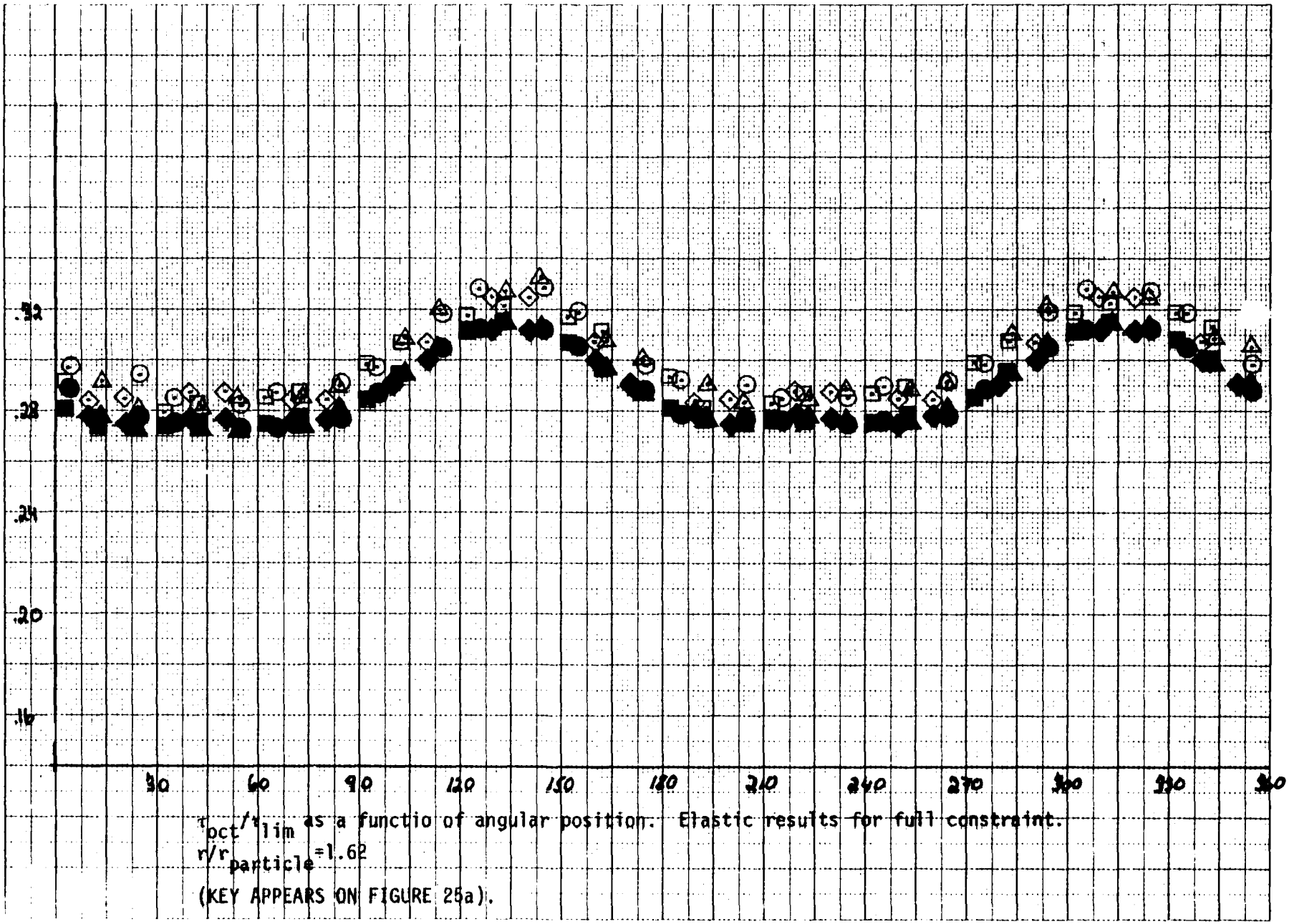

τ_{oct}/τ_{lim} as a functio of angular position. Elastic results for full constraint.
$r/r_{particle}$ =1.62

(KEY APPEARS ON FIGURE 25a).

Figure 53.

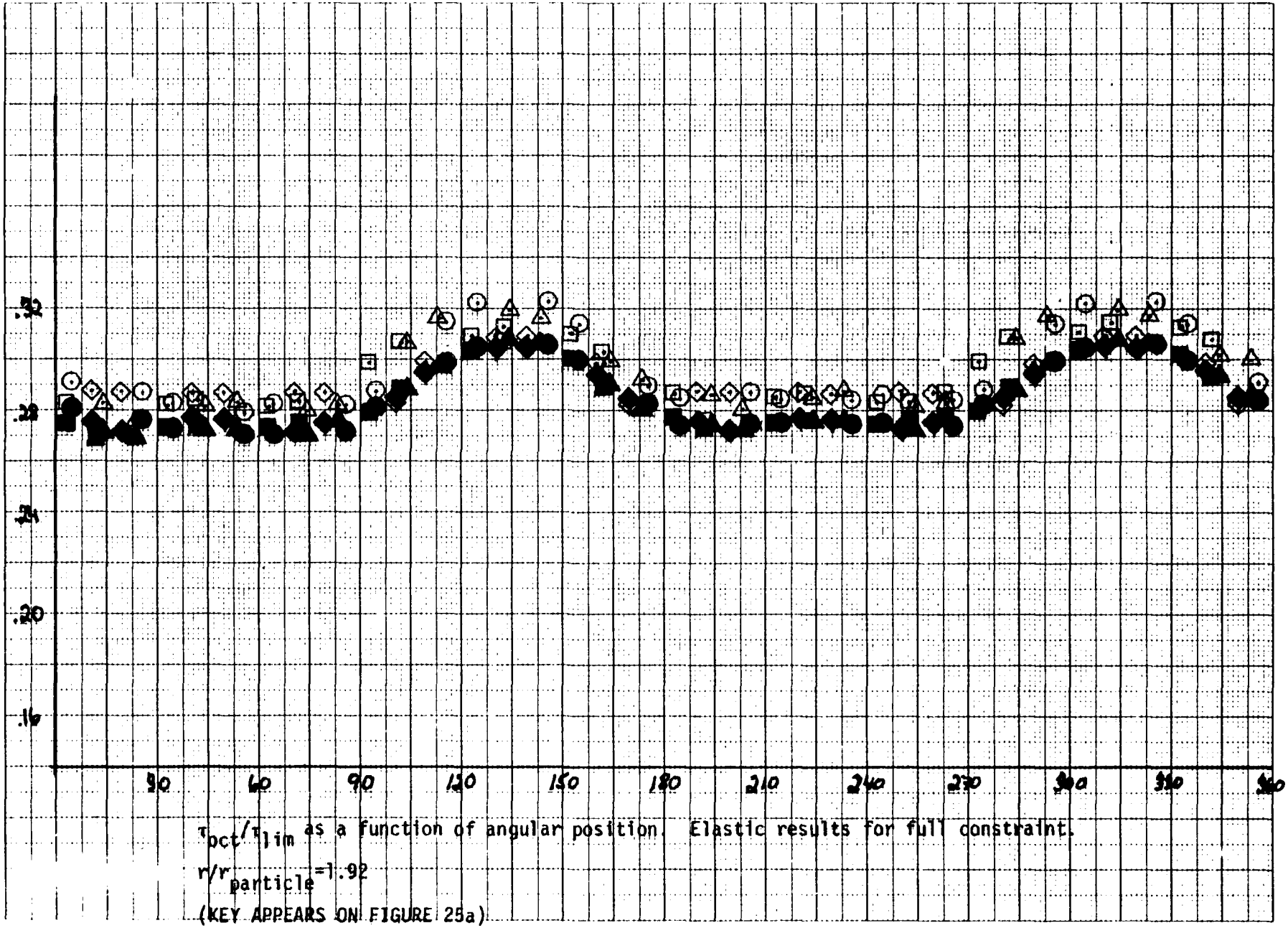

τ_{oct}/τ_{lim} as a function of angular position. Elastic results for full constraint.

$r/r_{particle}=1.92$

(KEY APPEARS ON FIGURE 25a)

Figure 54.

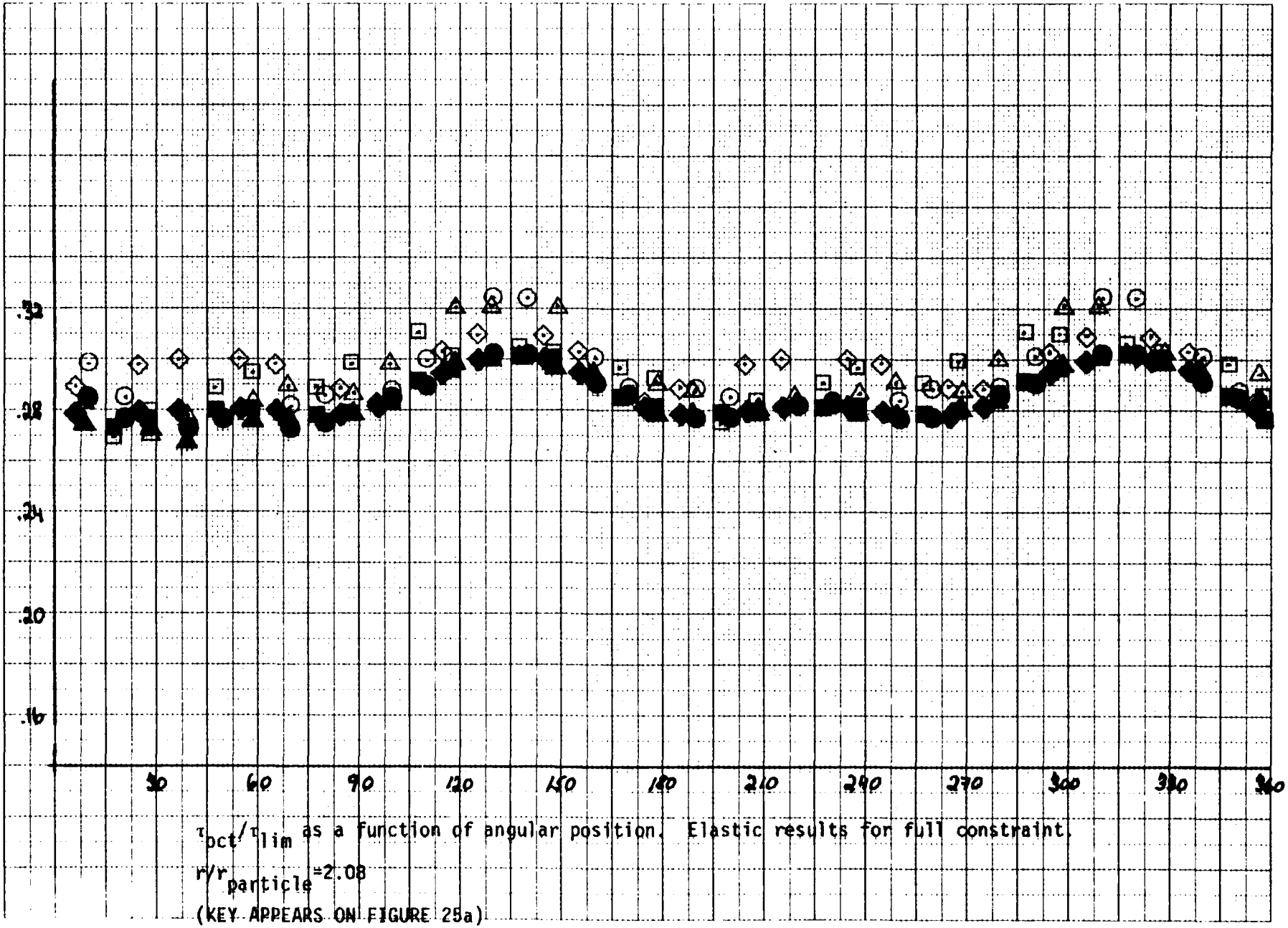

τ_{oct}/τ_{lim} as a function of angular position. Elastic results for full constraint.

$r/r_{particle}=2.08$

(KEY APPEARS ON FIGURE 25a)

Figure 55

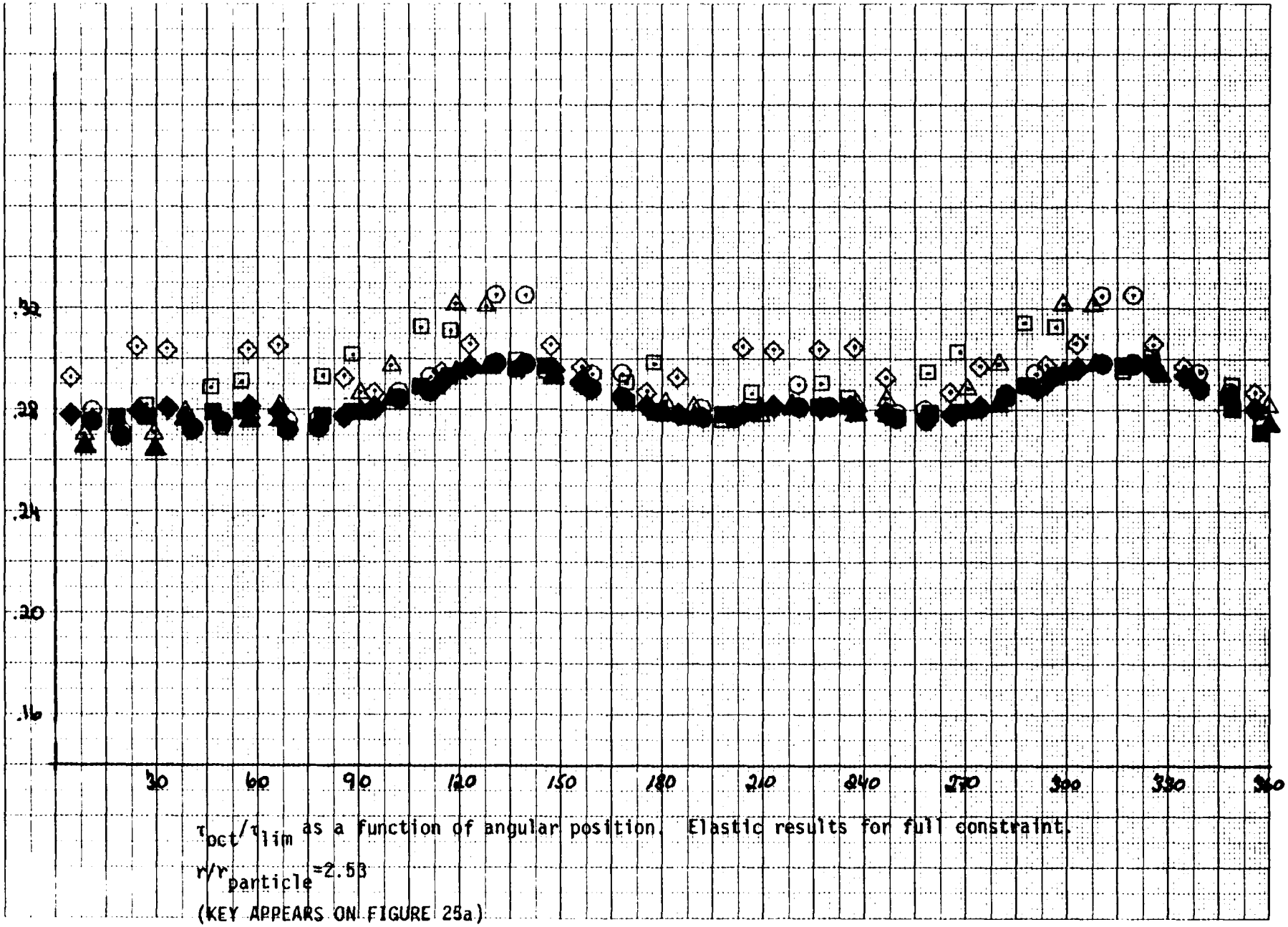

τ_{oct}/τ_{lim} as a function of angular position. Elastic results for full constraint.

$r/r_{particle}$ =2.53

(KEY APPEARS ON FIGURE 25a)

Figure 56

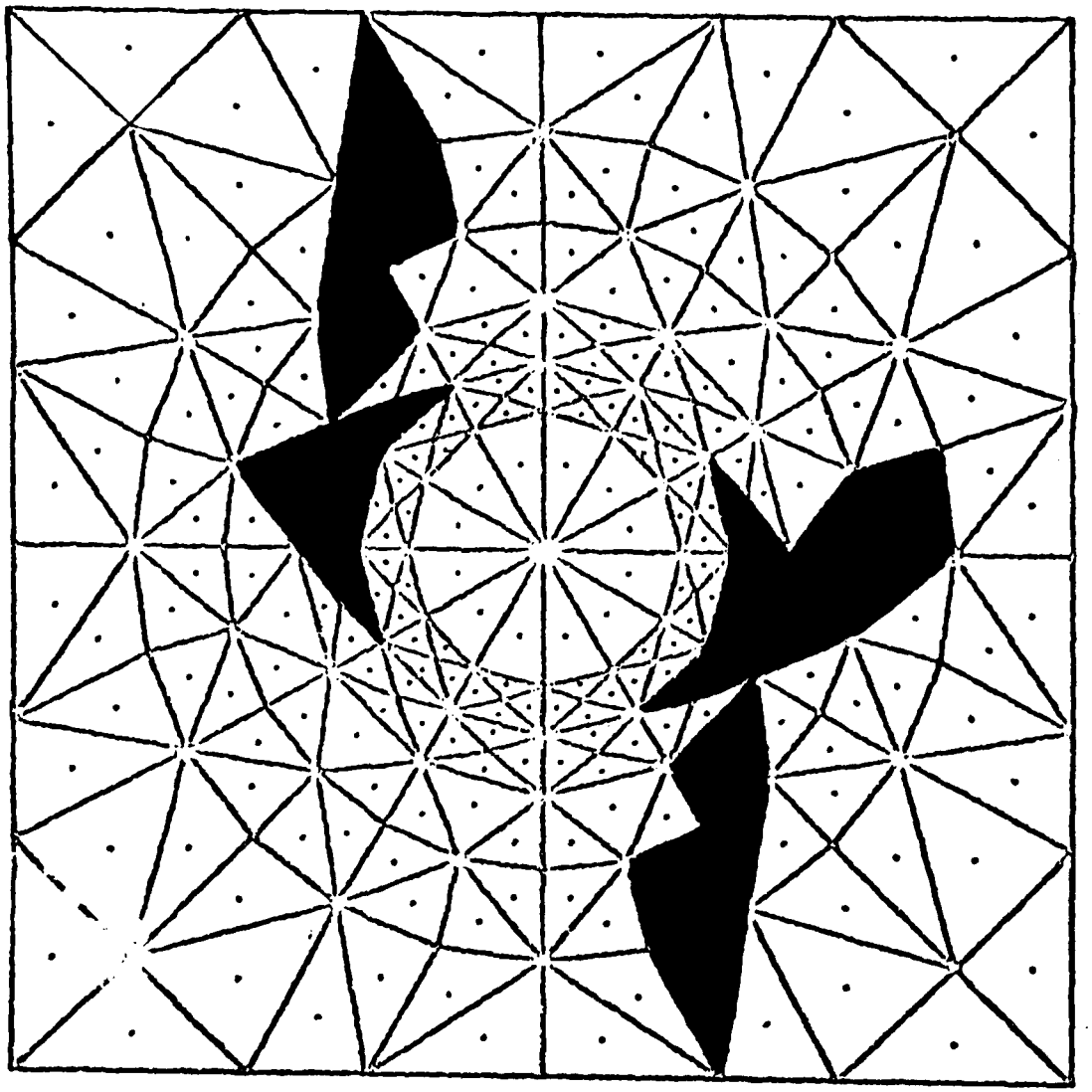

$$\frac{\gamma_{oct}}{\gamma_{lim}} > \left.\frac{\gamma_{oct}}{\gamma_{lim}}\right|_{\text{far field}} \times 1.05$$

Single particle

Figure 57.

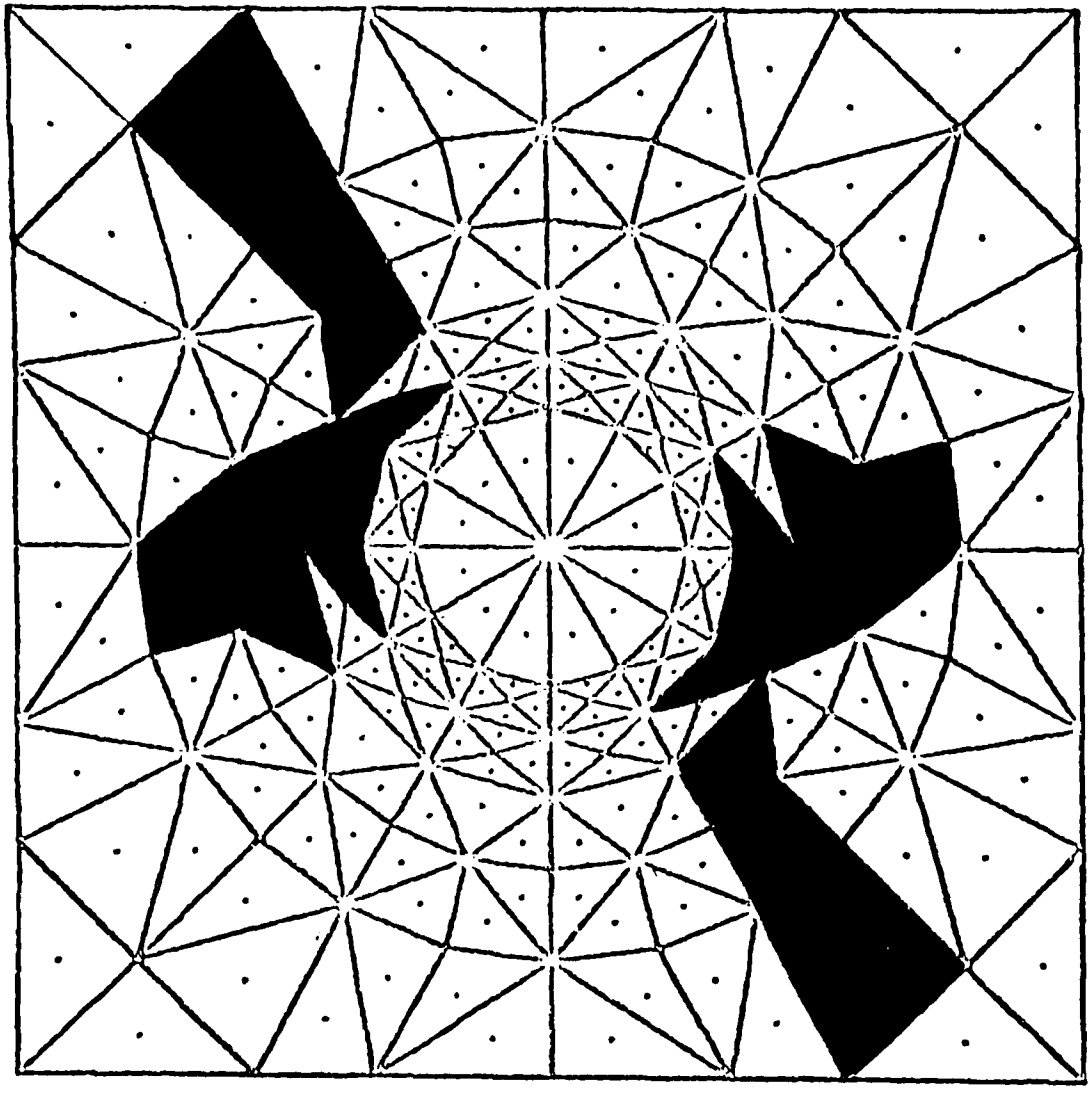

$\frac{\gamma_{oct}}{\gamma_{lim}} > \frac{\gamma_{oct}}{\gamma_{lim}}\Big|_{far\ field}$ x1.05 Multiple particles

Figure 58

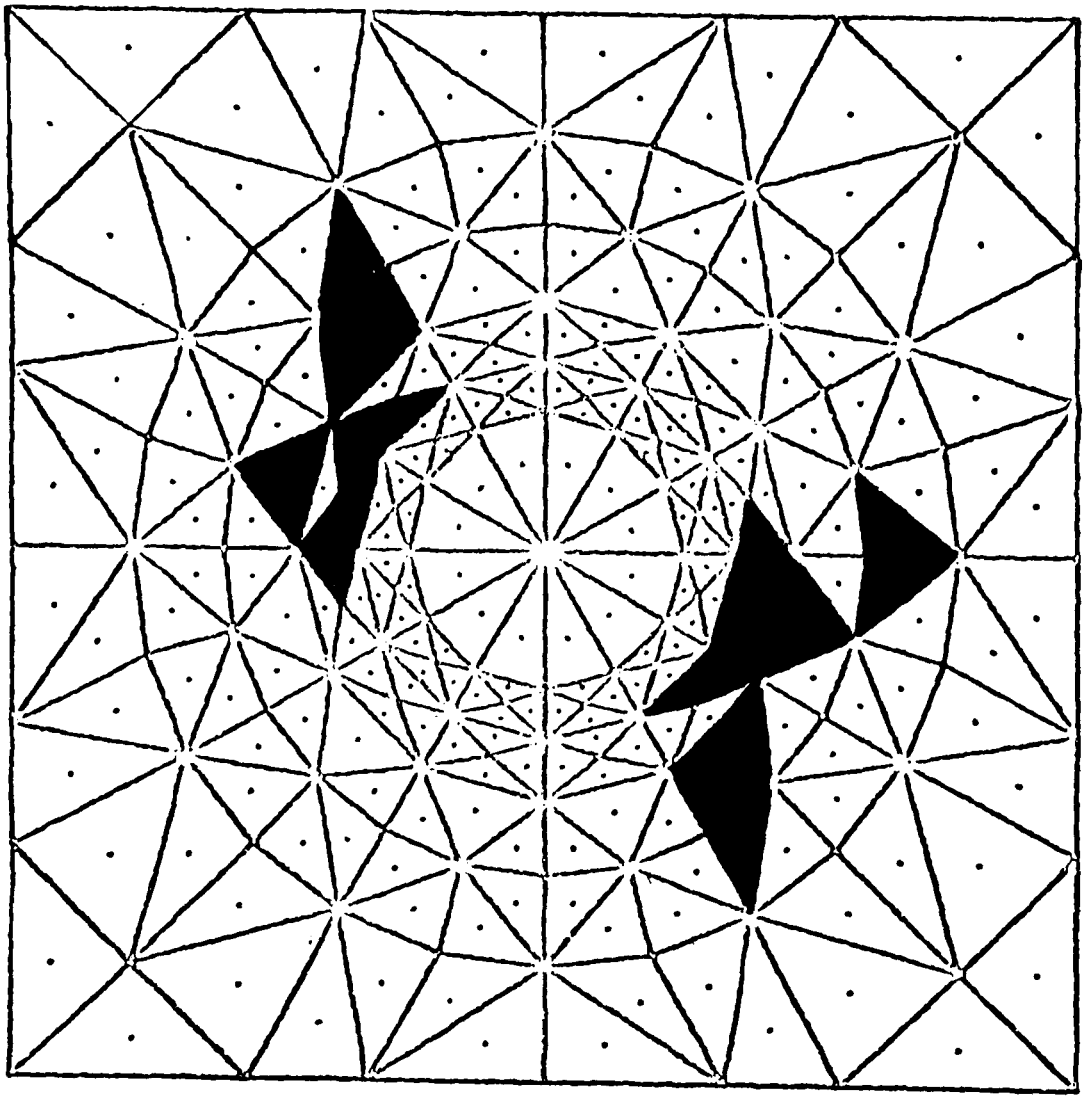

$$\frac{\gamma_{oct}}{\gamma_{lim}} > \left|\frac{\gamma_{oct}}{\gamma_{lim}}\right| \times 1.07$$

Single particle far field

Figure 59

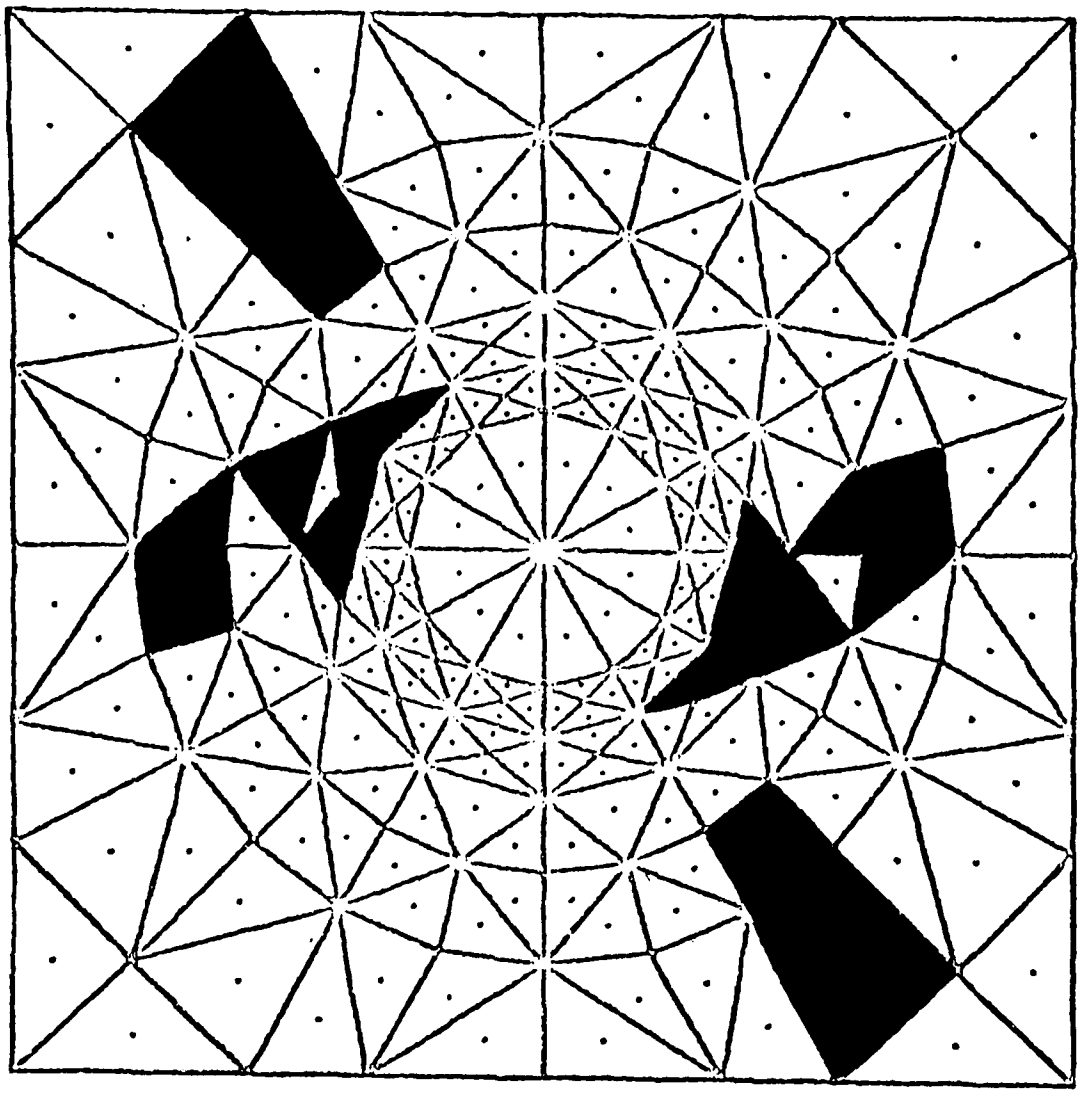

$\frac{\gamma_{oct}}{\gamma_{lim}} > \frac{\gamma_{oct}}{\gamma_{lim}}\Big|$ far field x1.07 Multiple particles

Figure 60

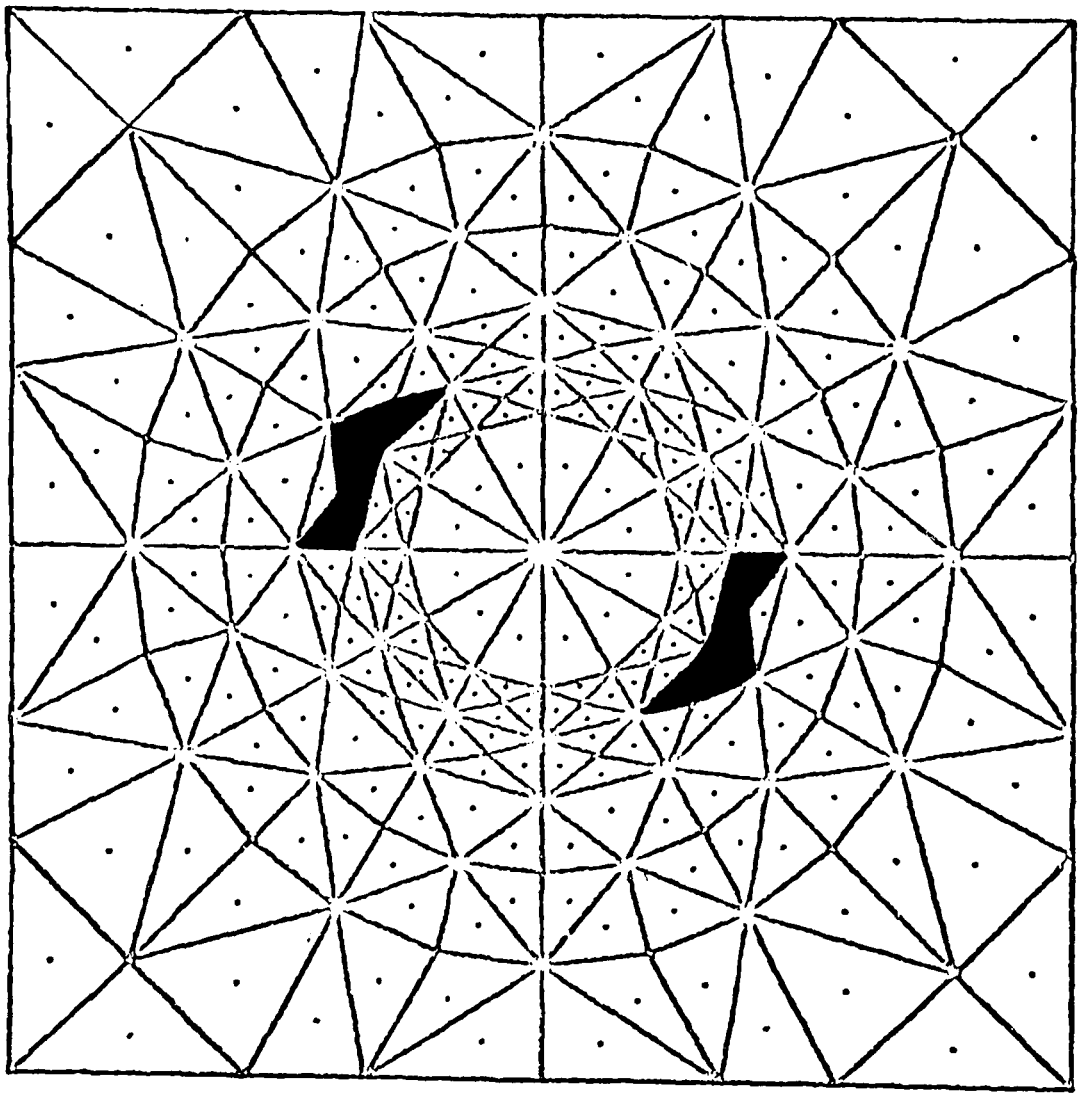

$\left.\frac{\gamma_{oct}}{\gamma_{lim}} > \frac{\gamma_{oct}}{\gamma_{lim}}\right|_{\text{far field}}$ x1.10 Single particles

Figure 61

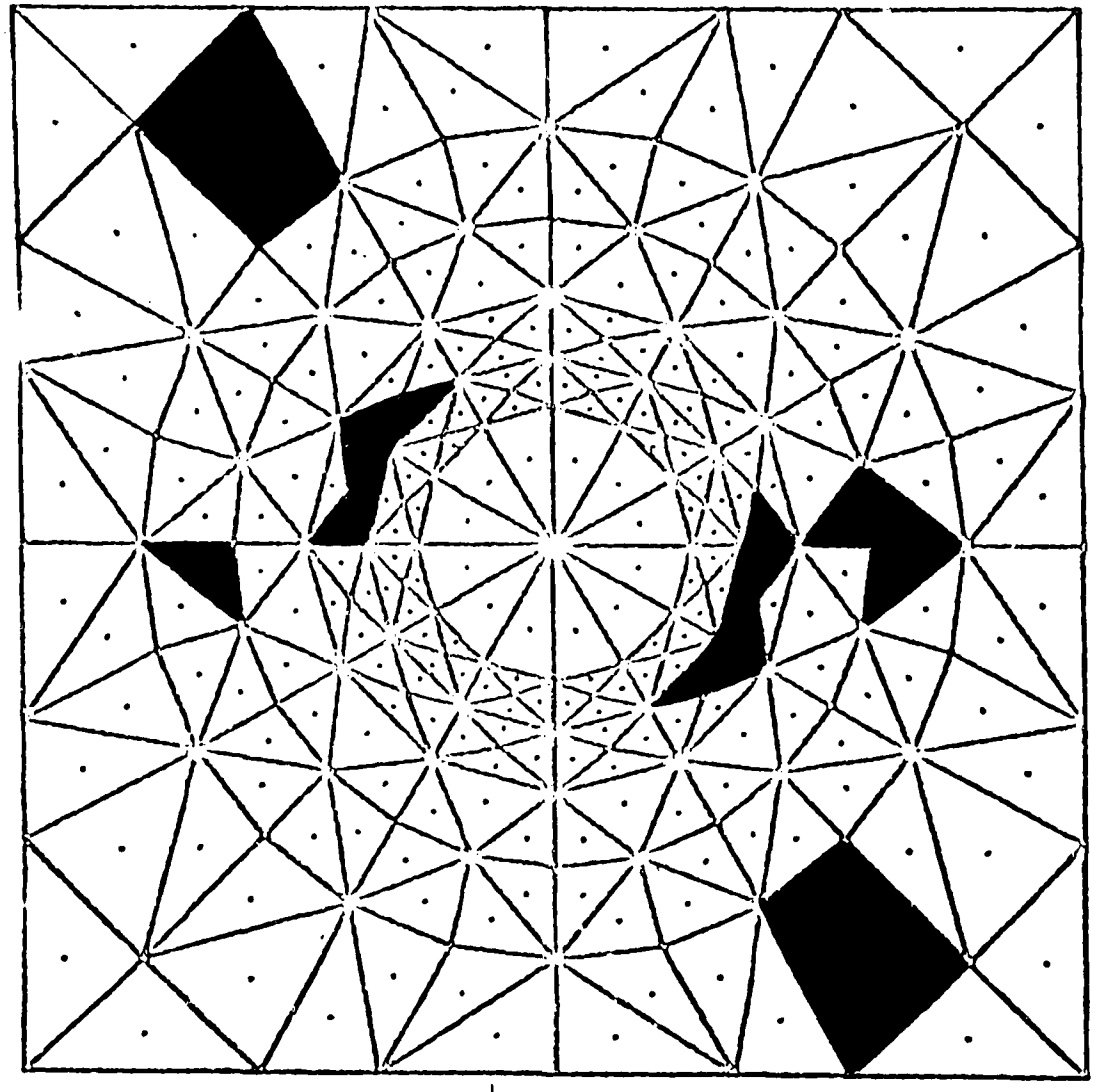

$\frac{\gamma_{oct}}{\gamma_{lim}} > \frac{\gamma_{oct}}{\gamma_{lim}}\Big|$ x1.10 Multiple particles far field

Figure 62


DATE
ILME